World-wide analysis and modelling of the ionospheric and plasmaspheric electron contents by means of radio occultations

Yixie Shao

Supervised by:
Professor Guillermo Gonzalez Casado
Professor Jose Miguel Juan Zornoza

1, September, 2018

Acknowledgement

First of all, I would like to give my deepest appreciation to Prof. Guillermo and Prof. Miguel, for all your patience and support in my study. I am really appreciated to your guidance and encouragement, which gives me the hope and helps me to find a way to carry on the research when I lost my direction. Thanks to your contribution in completing this dissertation.

I want to sincerely thank the gAGE group: Prof Jaume, Adria, Deimos, Jesus, Maite. I feel so lucky that I could study and work in gAGE to pursue my degree. With all your help, I gather more knowledge in GNSS and obtain more skills for research. Besides, I spent the lovely time in this group.

Furthermore, I am grateful to Estefania Blanch (Observatori de l'Ebre) and Angela Aragon-Angel (Joint Research Center). Thanks for your time and effort in reviewing this work and your precious suggestions.

Finally, I would like to give my great thanks to my husband, Albert. All your support and encouragement is really important for me. I am truly appreciated to your companion in the whole way.

Contents

List of Figures

List of Tables

Abbreviations

SE September Equinox

BIMS Bennett Ion-Mass Spectrometer

CHAMP Challenging Minisatellite Payload

CINDI Coupled Ion Neutral Dynamics Investigation

CNES National Centre for Space Studies

C/NOFS Communications/Navigation Outage Forecast System

COSMIC/FORMOSAT-3 Constellation Observing System for Meteorology, Ionosphere and Climate

EDP Electron Density Profile

EIA Equatorial Ionization Anomaly

ESF Equatorial Spread F

GAGE Group of Astronomy and Geomatics

GIM Global Ionospheric Map

GNSS Global Navigation Satellite System

GPS Global Positioning System

GPS/MET Global Positioning System/Meteorology

GRACE Gravity Recovery and Climate Experiment

HF High Frequency

IDM Ion Drift Meter

IGRF International Geomagnetic Reference Field

IGS International GNSS Service

LEO Low Earth Orbit

LT Local Time

NASA National Aeronautics and Space Administration

RO Radio Occultation

RPA Retarding Potential Analyzer

SAC-C Satellite de Aplicaciones Cientificas-C

SAMA South Atlantic Magnetic Anomaly

SM Separability Method

JS June Solstic

STEC Slant Total Electron Content

TEC Total Electron Content

UHF Ultra High Frequency

ME March Equinox

DS December Solstic

WSA Weddell Sea Anomaly

Nomenclature

CPDH model Chemical Equilibrium Plus Diffusion Equilibrium H^+ model

FLIP model Field Line Interhemispheric Plasma model

STIP model Simplified Topside Ionosphere plus Protonosphere model

Chapter 1

Ionosphere/Plasmasphere and Monitoring Technologies

1.1 Ionosphere and Plasmasphere

The atmosphere of the Earth is usually separated into different layers along the altitude based on different characteristics. For instance, if one considers the temperature, they are troposphere, stratosphere, mesosphere, thermosphere as the altitude increases. A further region above those layers is called the exosphere, which starts around $500km$ above the Earth's surface and extends up to $10000km$. While based on the other characteristics of the atmosphere, there is other definition of the layers which overlapped with the above ones.

The ionosphere is an abundant region in the atmosphere where ions exist. In most areas of the atmosphere, molecules are in combined state and remain electrically neutral. However, in the ionosphere, due to the intense solar radiation, part of the gas molecules are ionized. When enough atoms are ionized to significantly affect the electrical characteristics of the gas, it becomes plasma. Ionosphere stretches from around $50km$ above the surface till till $1000km$, overlapping into the mesosphere and parts of thermosphere and exosphere. The ionosphere is composed of three main parts, named for obscure historical reasons: the D, E and F regions. F region is the major and upper part of the ionosphere. It exists during both daytime and nighttime. During the day, it is ionized by solar radiation, during the night by cosmic rays. The E region exists in the middle, and it becomes weakened. And the D region is the bottom part, which disappear during the night.

Moreover, the Earth behaves like a huge magnet. The magnetosphere is the outer region surrounding the Earth, where charged particles spiral along the magnetic field lines. The plasmasphere is an inner part of the magneto-

sphere, located just outside the upper ionosphere with dense cold plasma. It is a doughnut-shaped region of low energy charged particles centered around Earth's equator and rotating with it. And its outer boundary varies, depending on geomagnetic conditions, from $4.5L$ to $8L$(L, Mcllwain L-parameter, is a distance (in the Earth's radii) from the Earth's center to a measuring point projected on the geomagnetic equator plane along the magnetic field). Figure 1.1 is an illustration of the layout and shape of plasmasphere and ionosphere, image source: *http://sci.esa.int/cluster/*. Comparing with the plasmasphere, ionosphere is a layer much more dense and thinner.

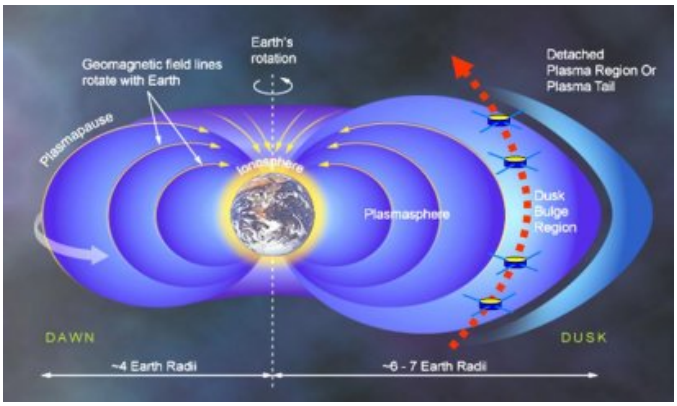

Figure 1.1: The showcase of plasmasphere and ionosphere

The ionosphere and plasmasphere are highly correlated. During quiet periods, the plasmasphere is charged by the ionosphere in daytime, while it acts as sources to fill the ionosphere to maintain the F2-layers at night. However, the geomagnetic activities will interrupt this normal process, speed up the interchange between these two regions. The boundary separating ionosphere and plasmasphere is defined as the transition region, where hydrogen ions(H^+) becomes the dominated ion constituent instead of oxygen ions(O^+) as the altitude increases. This region usually occurs at around 500 to 2000km altitudes, strongly depends on geophysical conditions such as solar and magnetic activities [10]. The behaviour of the ionosphere is often very dynamic. The electron densities over the ionosphere change from day to day, form day to night, with season and with solar cycle in a large range. And the plasmasphere is also not stable, it has similar but distinctive characteristics from ionosphere [9].

Free electrons in both ionosphere and plasmasphere affect the radio waves' propagation, i.e., these two regions play an important role in radio communication, navigation and related fields. The general ionospheric effects on radio navigation are shown in Figure 1.2, image source: *http://aer.nict.go.jp/en/*.

The Opacity of ionosphere varies according to the frequency of the radio waves. For the High Frequency (HF) radio waves and the ones with lower frequencies, ionosphere acts like a opaque wall. The signals from HF radars, or radio broadcasting, are blocked and reflected back to Earth by ionosphere. While, for the radio waves with frequencies above $30MHz$, ionosphere becomes more transparent. The Ultra High Frequency (UHF) waves, like the radio links from satellites, could penetrate plasmasphere and ionosphere. However, due to the refraction caused by the ionized region, the direction and speed of ray change while the radio passes through these two regions. According to the locations and the radio characteristics of these two regions, the radio links which propagate below ionosphere, i.e., the waves among ground-based, airborne devices, are only affected by ionosphere. While the radio links between space and air/ground are influenced by both ionosphere and plasmasphere.

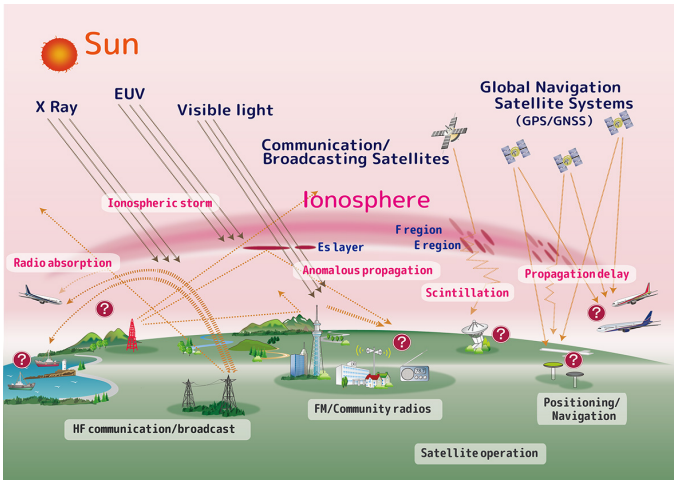

Figure 1.2: Ionospheric effect on radio navigation.

Thus, the analysis and study of ionosphere and/or plasmasphere is of chief interests for the applications related to the radio navigation. It is critical to have the correct information of ionosphere in precise positioning. On the other hand, it also introduces some way to carry out climatology analysis of thermosphere and exosphere.

1.2 Monitoring Technologies

Based on the impacts of the ionized layers of atmosphere on the radio waves, the various techniques of radio sounding on ionosphere and/or plasmasphere were developed. In general, they could be grouped into the ground-based and space-borne sounding.

The ground-based sounding could also be separated into two types. Type I is usually obtaining the characteristics of ionosphere by analysing the echoes of signals transmitted by its own transmitter, ground-based radio sounding can obtain the accurate estimation of the bottom layer of the ionosphere. The typical examples are ionosondes or incoherent scatter radars. Ionosondes, which are HF radars in principle, measure ionospheric reflection height by recording the time of a transmitted HF signals. The transmitter in ionosondes transmits short pulses with frequencies sweeping all or part of the HF range. Then the receiver records returned signals which are reflected from different layers of the ionosphere. Thus it can provide high accuracy estimation at heights of $100 - 400km$ [1], in local region. The incoherent scatter radars using the Doppler effects of radio signals, were introduced to the measurement of ionosphere shortly after 1958 when [5] pointed out that with the existing radar sensitivities, it should be feasible to measure ionospheric electron densities by detecting this weak Thomson scattering. Compared with ionosondes, it can obtain the complete electron density profile, electron and ion temperatures, and ionospheric motions. However, it is also relatively more expensive.

Type II is based on non-collocated receiver and transmitter. The Global Positioning System (GPS) project was launched by the U.S. Department of Defence in 1973 for use by the United States military and became fully operational in 1995. The civil usage of the GPS was applicable in 1980s. And the original set of 24 satellites of the Global Positioning System (GPS) were fully launched and became operational for navigation in 1990s. It is one constellation in Global Navigation Satellite System (GNSS) which aims to provide precise geo-location and time information globally, equivalent as Russia's GLONASS, China's BeiDou Navigation Satellite System(BDS) and the European Union's Galileo. On the other hand, the GPS signals is also an important source to study the ionosphere/plasmasphere. The receivers of GPS signals could be distributed in different places according to the distinctive purposes and methodologies. For instance, the computation of Global Ionospheric Map (GIM) is based on the GNSS ground network. In 1998, the International GNSS Service (IGS) Ionosphere Working Group (Iono-WG) was established by IGS Governing Board, and commenced to work. Since then, it began to provide reliable IGS Global Total Electron Content (IGTEC) maps with a 2-hours time resolution based on recorded GNSS measurements from ground receivers [7]. Besides, the GPS receivers could also be carried by aeroplane and ships. They are quite flexible and could provide some regional monitoring of ionosphere. However, it is hard to give a general picture of the ionosphere.

Space-borne radio sounding. It fills the gap of accurate estimation of upper-layer's ionosphere in ground-based sounding. Besides, it also brings a way to monitor the plasmasphere depends on the orbits of the satellites or other space-carriers. There are many different methods. The direct *in situ* measurements about the ions composition, density, velocity and related parameters could be obtained by instruments and devices carried by rockets or satellites. One of the simplest devices is the Langmuir probe, named as Irving Langmuir, which measures the ionospheric density *in situ*. Bennett Ion-Mass Spectrometer (BIMS) and Retarding Potential Analyzer (RPA) carried in satellites Atmosphere Explorer-C and Explorer-E have the same function, but provide the measurement of more parameters. It is simple but with extremely constraint in region. The idea of topside sounder satellite was introduced shortly after the first artificial Earth observation satellite was launched in 1957. It has the same working principle like type I ground-based sounding. The first topside sounder Alouette I was Canadian-built and US-launched on 29 September 1962. After that, a series of follow-on improved topside sounders, satellites Alouette 2, ISIS 1 and 2, were launched in 1965, 1969 and 1971, respectively. They were dedicating to ionospheric, magnetospheric radio sounding in a large scale [3], [2].

There are a lot of space sounding techniques using the GPS transmitted signals as the source. JASON-1 and 2, are joint projects between the National Aeronautics and Space Administration (NASA) and National Centre for Space Studies (CNES) space agencies. Since 1992, the plasmaspheric information could be derived based on the measurements from on-board GPS receivers. GPS Radio Occultation (RO), is a relatively new technique in space-borne sounding, using the GPS signals received during occultations. In 1995, the first GPS RO experiment for monitoring the atmosphere of the Earth, Global Positioning System/Meteorology (GPS/MET) mission, was carried out to prove the possibilities of RO techniques in Earth's atmosphere monitoring. Since then, many Low Earth Orbit (LEO) satellites were launched dedicated for collecting the RO measurements, for instance, Challenging Minisatellite Payload (CHAMP), Gravity Recovery and Climate Experiment (GRACE). Since 2006, the deployment of Constellation Observing System for Meteorology, Ionosphere and Climate (COSMIC/FORMOSAT-3), which consists 6 satellites, produces abundant data for ionosphere studying.

1.3 Research Objectives

This doctoral thesis will study the characteristics of the topside ionosphere/bottomside plasmasphere based on RO techniques. Abel transform inversion is widely used to get vertical electron density profiles in the iono-

sphere (Ne) from RO measurements, shortly after it was introduced in [8] and [11]. However, the several assumptions in classic Abel inversion bring large errors, approximately 20% reported comparing with ionosonde measurements. The Separability Method (SM), introduced in [6], is a TEC-aided Abel inversion method which overcomes the biggest error source in classic Abel inversion, symmetrical hypothesis, and improves the precision of profiles significantly. However, compared to the classic Abel inversion, SM methodology requires extra TEC information, which could be obtained from GIM, for instance, IGS GIMs. SM is the main inversion method used in this study. More details about the RO inversion techniques will be described in Chapter 2. The objectives of this research could be summarized into two points:

- Point I, it focuses on the methodology in profile retrievals from RO measurements, and aims to get more precise profiles from measured data. One objective in this thesis is checking and validating the improvement brought by SM corresponding to classic method. On the other hand, SM needs the assistant of Global Ionospheric Map (GIM). Hence, the impact of GIMs precision on retrieval results will also be studied. This point will be treated in Chapter 3.
- Point II, it is climatological study of ionosphere/plasmasphere based on the RO retrievals to give a general picture of characteristics and features of these two regions in different solar periods, solar minimum and maximum. The models of topside profiles will be used to separate the ionospheric and plasmaspheric contribution of the GPS Total Electron Content (TEC). The characteristics of topside ionosphere/bottomside plasmasphere in 2007 and 2014 will be studied. This point will be carried out in Chapter 4 and 5.

1.4 Thesis structure

This thesis consists of 6 chapters. Chapter 1, *Ionosphere/Plasmasphere and Monitoring Technologies*. It contains a description of ionosphere, plasmasphere, and radio sounding techniques of these two regions. It also gives research objectives of this doctoral thesis. The main part of this thesis could be be divided into two parts according to the research objectives.

Part I is related with the methodology of RO retrievals:

- Chapter 2, *Radio Occultation and Methodology of RO retrievals*. It introduces the principles of Radio Occultation techniques, and the methodologies of inverting electron profiles from RO measurements.

- Chapter 3, *Improvement of the ionospheric RO retrievals by means of accurate Global Ionospheric Map (GIM)*. It checks the performance of different methodologies in RO inversions and the impact of the GIMs precisions. Besides, it studies the mis-modellings in retrieval methods and their affects, along with the ways to overcome these errors.

Part II is about climatological study of ionosphere and plasmasphere:

- Chapter 4, *Modelling of the topside ionosphere/bottomside plasmasphere from RO retrievals*. It describes Simplified Topside Ionosphere plus Protonosphere model (STIP model), which was introduced in [4], to separate ionosphere and plasmasphere from topside ionosphere and derive the transition height between these two regions. The validations of this model based on some sample data will be carried out. The general features of the parameters to describe ionosphere/plasmasphere, scale height hs and transition height hu are studied under different conditions. And the relationship between ionospheric scale height and transition height is also checked.

- Chapter 5, *Study of Ionospheric and Plasmaspheric contributions to GPS TEC in Two Different Periods of Solar Cycle*. It mainly focuses on the characteristics of $IONf$ in solar minimum and maximum. The different ionospheric anomalies could be found through $IONf$. Besides, the similarity and difference between ionosphere and plasmasphere are studied. Furthermore, the capacitor model is introduced to model the $IONf$.

The thesis will end with Chapter 6, *Conclusions and guidelines for future research*, which contains the gained key points along with some guidelines for the future research inspired from this study.

Chapter 2

Radio Occultation and Methodology of RO retrievals

2.1 Radio Occultation

The working principles of RO technique are shown in Figure 2.1, image source: *http://www.cosmic.ucar.edu/ro.html*. This technique should at least contain one Low Earth Orbit (LEO) satellite with GPS signal receivers on board and one GPS satellite. The ray of GPS signals are bent due to the ionized region in the ray-path. As a result, the GPS signals could be "seen" by the receivers on LEO which are below the horizontal line. RO technique mainly recovers the ionospheric/plasmaspheric information from these received signals.

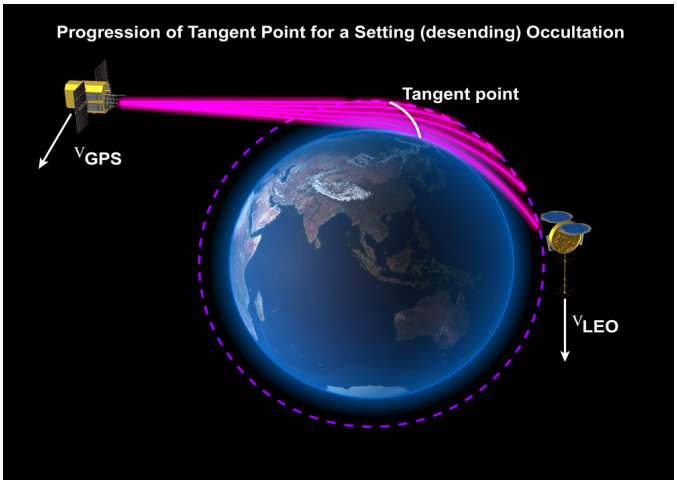

Figure 2.1: The working principles of RO.

The Radio Occultation (RO) technique was initially used in the study of planetary atmospheres and ionospheres [19], [20]. Since the GPS was fully operational, early 1990s, it has emerged as a powerful and relatively inexpensive approach for sounding the global atmosphere with high precision, accuracy, and vertical resolution in all weather and over both land and ocean [12]. Global Positioning System/Meteorology (GPS/MET) mission, from April in 1995 till March in 1997, was the first GPS occultation experiment with GPS receivers carried on MicroLab-I satellite. The RO techniques in recovering refractivity, density, pressure, temperature and water vapor profiles [8] and performing ionospheric tomography [18] were explored based on over 11000 occultations recorded during this experiments. After that, many other missions were carried out, such as the German geoscience satellite Challenging Minisatellite Payload (CHAMP) and international cooperative mission Satellite de Aplicaciones Cientificas-C (SAC-C), that both were launched in 2000. As a result, more occultation data were available. However, the sparsity and scarcity of occultation data still limit the global study of ionosphere by means of GPS RO techniques. Thanks to the successful deployment of Constellation Observing System for Meteorology, Ionosphere and Climate (COSMIC/FORMOSAT-3), the limitations of the RO data are overcame. COSMIC is a set of six satellites with the orbits around $800km$ above Earth, which is well above the F2 layer peak, and able to provide sets of data distributed globally and almost uniformly. In this doctoral project, the long-term, world-wide study of ionosphere will be carried out by means of GPS RO from the measurements of COSMIC LEO satellite.

2.2 RO retrievals

In RO technique, the EDP can be retrieved by means of the geometry-free combination (LI) of GPS measurements collected by a dedicated receiver on board of a LEO satellite during an RO and using the following equation:

$$L_I = L_1 - L_2 = \alpha STEC + b \tag{2.1}$$

where L_1 and L_2 are the GNSS carrier phase measurements at two different frequencies $f1$ ($1575.42MHz$), $f2$ ($1227.60MHz$). Slant Total Electron Content (STEC) is the slant Total Electron Content (TEC), the integrated electron density along the ray path between the GPS and LEO satellites, defined as:

$$STEC = \int_{LEO}^{GPS} N_e(\lambda, \phi, h) dl \tag{2.2}$$

Further, $\alpha = 0.105m/TECU$, where $1TECU = 10^{16}el/m^2$, is a conversion factor between STEC units and the LI units. And, finally, b is a constant per arc of measurements that includes the carrier phase ambiguity and hardware

delays. Assuming an onion-skin model, shown in Figure 2.2, the integration of STEC (equation 2.2) can be discretized.

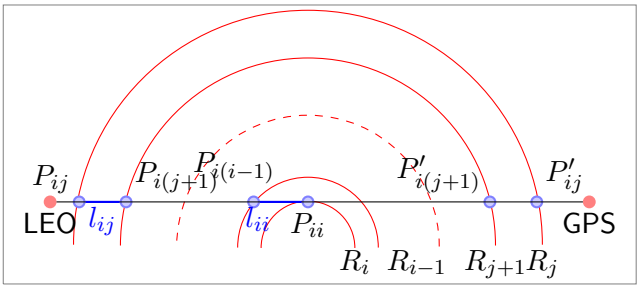

Figure 2.2: Layout of the onion-skin geometry

In the past century, [8] and [11] introduced the study of electron density in the ionosphere (Ne) by means of the Abel transform inversion for retrieving vertical profiles from GPS radio occultation (RO) observations. The Abel transform inversion technique, hereafter, referred to as classic Abel inversion or classic approach, is mainly based on three assumptions:

- Spherical symmetry, i.e., the electron density must be spherically symmetric and, only depending on height.
- Straight-line signal propagation between GPS and LEO satellite links.
- An initial value of electron density at some top altitude sounded by the occultation.

In classic Abel inversion, there is only one Ne value for each layer in onion-skin model in a given time, since it only depends on height. Hence, we can obtain equation 2.3.

$$STEC(p_i) = \sum_{j=1}^{j=i} 2l_{ij} \times Ne(p_j) \tag{2.3}$$

where the impact parameters p_i, p_j are the geocentric distance of the tangent points of layer R_i, R_j respectively.

In [11], it was shown that the spherical symmetry assumption is one of the most important error sources in the electron density retrievals from RO. To overcome this error, several methods have been developed that take into account the horizontal gradients of Ne. For instance, [17] introduced a 3D tomographic reconstruction that is constrained by the vertical Total Electron Content (TEC). In 1998, the International GNSS Service (IGS) started to

compute Global Ionospheric Map (GIM) based on observations gathered by a worldwide distributed network of ground receivers. Since that date, IGS GIMs have become one of the standard sources for obtaining TEC. Based on those maps, different TEC-aided Abel inversion methods have been proposed to improve the results obtained from classic Abel inversion method, [11], [13], [23]. More recently, regional or global maps of quantities, such as the F2 peak electron density ($NmF2$) or previously determined Electron Density Profile (EDP), have been used to develop similar methodologies to improve the accuracy of RO retrievals, [21], [22], [14].

The Separability Method (SM), is based on the hypothesis that Ne can be written as the product of two functions, one being the TEC depending on the horizontal coordinates and the other relating only with the vertical height. Using the SM, [15] and [16] compared the results of RO retrieved Ne with ionosonde measurements and reported average improvements of 30 and 45%, respectively, over the results obtained from the classic approach.

2.3 Basic concepts of SM

The basic concepts and the equations used by the SM are summarized in this section. The main advantage of SM is that it overcomes the spherical symmetry, i.e., electron density not only varies with different heights, h, but also distinct horizontal locations, could be represented by longitude, λ, and latitude, ϕ. In this sense, there are different Ne values in P_{ij} and P'_{ij}, even they are at the same height. Ne can be modelled as the product of two functions: one depending only on the altitude, $F(h)$, referred to hereafter as shape function, and another depending on the longitude and latitude, for instance, a horizontal TEC map from IGS, to represent the electron density as 2.4.

$$N_e(\lambda, \phi, h) = TEC(\lambda, \phi) \times F(h) \tag{2.4}$$

By introducing above equation, STEC can be written as:

$$\begin{aligned} STEC(p_i) = {} & 2 \times l_{ii} \times TEC(\lambda_{ii}, \phi_{ii}) \times F(p_i) + \\ & \sum_{j=1}^{j=i-1} l_{ij} \times [TEC(\lambda_{ij}, \phi_{ij}) + TEC(\lambda'_{ij}, \phi'_{ij})] \times F(p_j) \end{aligned} \tag{2.5}$$

As it is shown in [4], the EDP retrievals do not depend on the values which affect all the measurements of an RO equally, such as the EC above the LEO or the constant b. Since they can be removed by subtracting from all measurements a common reference value of LI, which can be selected, for example, from the measurement taken when the GPS satellite is at the

LEO satellite horizon during the RO. Thus, starting from the uppermost ray (i=1), where the observation tangent point coincides with the LEO position, the value of $F(p_1)$, shape function for the tangent point P_{11}, can be derived following [4]. From this point, equation 2.1 can be solved in a recursive way using equation 2.5 to obtain the value of $F(p_i)$ for each tangent point P_{ii} in each step.

Once the shape function $F(h)$ is obtained, EDP at the specific region, (λ, ϕ, h), for a given time can be determined from the equation 2.4 with the TEC value of a specific horizontal point (λ, ϕ) obtained from GIMs of that time.

According to the above equation, if one considers a uniform TEC, so no horizontal gradient exists, a spherical symmetry relationship used by the classic approach is obtained. Equation 2.5 is simplified as equation 2.3. Therefore, when the external TEC GIM is highly smoothed, like in poorly sounded regions, the retrieved EDP will be very similar to the retrievals obtained using the classic approach.

Moreover, the right side of equation 2.5 can be written as:

$$\begin{aligned} & l_{ij}[TEC(\lambda_{ij}, \phi_{ij}) + TEC(\lambda'_{ij}, \phi'_{ij})]F(p_j) \\ & = l_{ij}\frac{TEC(\lambda_{ij}, \phi_{ij}) + TEC(\lambda'_{ij}, \phi'_{ij})}{TEC(\lambda_{ij}, \phi_{ij})}N(p_j) \end{aligned} \tag{2.6}$$

where the fraction on the right side of 2.6 is the asymmetry factor used in [21] or [22]. Consequently, the techniques using the asymmetry factors are equivalent to the SM. However, in the first case, since $Ne(p_j)$ is directly calculated instead of $F(p_j)$, an oblique EDP is obtained because the tangent points used to retrieve the profile are not aligned vertically. On the contrary, the SM initially calculates $F(p_j)$, while the vertical EDP is calculated using equation 2.4 with the TEC at a given location covered by the RO.

Large differences can be found in the peak electron density between an oblique EDP and the profiles from the SM or the classic approach, as one can see from Figure 2.3. In this figure, green line represents the EDP obtained using classic approach, while the rest of lines are the ones for SM using different values of TEC in equation 2.4 to calculate the electron density profile. They are the oblique profile using the TEC at each tangent point, blue line; vertical profile using the TEC at the highest (P_{11}), red, and lowest (P_{nn}) tangent points of the RO, cyan, respectively.

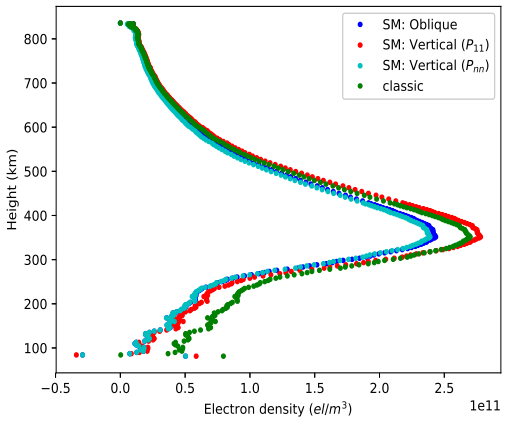

Figure 2.3: Different EDPs using different methods to invert the RO.

2.4 Other formats of SM

As introduced in previous section, Ne could be represented by the product of a shape function depending on altitude and one horizontal quantity varies with longitude and latitude. In the original format, TEC map, such as IGS GIMs, is treated as this horizontal quantity. However, it could be associated with any other magnitude linked to the EDP instead of TEC. For instance, one could use a map for $NmF2$. In [21], the monthly mean $NmF2$ distribution in latitude, longitude, and local time is obtained to aid the Abel inversion. In this way, the electron density as:

$$N_e(\lambda, \phi, h) = NmF2(\lambda, \phi) \times f(h) \tag{2.7}$$

where $f(h)$ is also a shape function describing the vertical variation of the EDP. Then, integrating this equation over the altitude, one can obtain the vertical TEC at any horizontal coordinates (λ, ϕ) as:

$$TEC(\lambda, \phi) = NmF2(\lambda, \phi) \int_0^\infty f(h)dh \tag{2.8}$$

where the integral on the right side is the so-called slab thickness parameter, which only depends on the vertical shape of the profile. Therefore, taking into account that the SM implicitly assumes a constant slab thickness, it is irrelevant to use the original TEC map, as in [6], or a horizontal map of $NmF2$ values as, for instance, in [21].

Chapter 3

Improvement of the ionospheric RO retrievals by means of accurate global ionospheric maps

3.1 Introduction

As mentioned in the chapter 2, TEC-aided Abel inversion overcomes the major error caused by spherical symmetry assumption. In this chapter, the performance of SM compared to the classic Abel inversion will be checked. One issue raised by [23] is that the performance of the TEC-aided methods could be determined by the quality of the TEC values used in the derivation of the EDPs. However, this assessment can hardly be quantified because the different works have used not only different TEC-aided methodologies but also different data sets gathered on different days and in distinct regions with varying ionospheric conditions. Besides, the accuracy of the different GIMs greatly varies from one study to another. The IGS GIMs or other similar GIMs generated by some of the centers involved in the IGS computation, generally consider the ionosphere distributed in a single layer at the height of $450km$. In [26], an ionospheric model was used with a geometric description of the ionosphere that overcame this simple description of a single layer. This model introduced an additional layer to account for the ionospheric delays in radio signals occurring at larger heights. The ionospheric delays obtained from those two-layer GIMs, known as the Group of Astronomy and Geomatics (GAGE) GIMs, were compared in [31], with respect to the ionospheric delays from the IGS GIMs, showing that the error of the ionospheric predictions is significantly reduced when the GAGE GIMs are used instead of the IGS GIMs. Hence, IGS and GAGE GIMs will be used to check the effects of the different GIMs in SM.

Besides, we will have more discussion about other errors and possible mismodelling in the RO retrievals using TEC-aided Abel inversion, to further improve the accuracy of the RO retrievals .

Using data from the Jicamarca ionosonde near the magnetic equator, [24] found a 10% improvement when using a narrow window to collocate the RO retrieved EDPs that were used in the comparison. However, [23], when comparing with ionosonde measurements, found a quite moderate improvement, of about 7%, in its TEC-aided Abel inversion results with regard to the classic approach and practically no improvement when comparing between large scale ionospheric features of the Ne retrievals. One reason for the discrepancies in the results is the so-called lack of collocation (LoC) error. This error increases as the geographical location of the F2 peak of the EDP observed during the RO is further from the ionosonde location. This trend was already noted in [15] when using a maximum distance of $2000km$ to compare RO and ionosonde results, showing that the error growth with distance is clearly larger for the classic approach than for the SM and that the advantage of the SM with respect to the classic approach relies on this capability to mitigate the LoC error when comparing with ionosonde measurements.

On the other hand, according to [4], the EDP retrievals from ROs depend only on the electron content (EC) below the LEO so that the EC above the LEO only affects the Ne retrievals at the altitudes near the LEO height. In fact, this characteristic was used by [25] to infer the plasmaspheric EC by comparing the EC associated with the EDP retrieval with the TEC. However, this finding implies that the TEC-aided inversion could be affected by some mismodelling because TEC is used instead of EC below the LEO satellite height to describe the horizontal gradient in the electron distribution for the EDP retrieval.

3.2 Data, tests and metric used for study

This section describes the different quantities and statistical parameters used to assess the performances of different techniques considered in the present study for electron density retrievals from ROs. These techniques are: spherical symmetry Abel inversion or classic approach, SM aided by the TEC extracted from the IGS GIMs and SM aided by the TEC from the GAGE GIMs. At the end of this section, the data sets considered for the different comparisons are also described.

3.2.1 Description of the tests and metric

In order to assess the performance of the RO inversion methods, two tests are carried out in this study.

First test is related to the errors accumulated by the use of recursive strategy, which is the method commonly applied in solving the equation 2.1 to retrieve the EDPs.

Due to recursive procedure, the errors in the electron density retrieval propagate downwards in altitude, as it has been reported in several works. Therefore, the worst estimated values will correspond to the retrievals at the lowest heights. However, for altitudes below $100km$ a significant ionization is not expected. Hence, the electron content between 80 and $100km$

$$EC_{100} = \int_{80}^{100} Ne \cdot dh \tag{3.1}$$

can be compared with zero to test the accuracy of the profile, with a better accuracy corresponding to smaller values of this parameter.

It is worth emphasizing that the testing based on EC_{100} does not rely on the comparison with reference ground measurements at a given location as, for example, from ionosondes, and hence, is not affected by the LoC effects. For this reason, the EC_{100} test can be done on a global scale, including all locations over continents or oceans, where RO observations are available.

Notice also that this test is different from other tests that compare the electron density retrievals at low altitudes [23], [21], which are based in the difference between the results of a new proposed method and the classic approach, while the test proposed in the present study compares the EC_{100} retrievals with zero.

Besides, the low-latitude ionosphere is characterized by the Equatorial Ionization Anomaly (EIA), which will be described in details in chapter 5, and the existence of unexpected electron density reductions, termed as "plasma caves", located underneath the EIA crests has been reported in many studies. [52] presents that classic Abel inversion overestimates electron density to the north and south of the crests of the EIA, and introduces artificial plasma caves underneath the EIA crests. [29] suggests that the artefacts appears mainly below $250km$ altitudes and becomes pronounced when the EIAs are well developed. However, it also points out that due to the significant errors in the bottomside ionosphere around magnetic equator introduced by spherical symmetry assumption, the plasma caves cannot be detected or ruled out through RO profiles using classic Abel inversion. Actually, [28] reports the existence of plasma caves based on electron densities simulations from the International Reference Ionosphere (IRI-2007) and clear evidences given by plasma density and drift measurements of the Dynamic Explorer 2 (DE 2) satellite during 1981–1983. However, it is daytime

features, and only located at 5^o – 10^o to the magnetic equator. Equatorial plasma caves will be also checked in this test.

The second test compares the RO retrievals with other measurement on the F2-layer critical frequency, $foF2$, units in Hz. In this case, the ionosondes measurements are gathered as the reference. $foF2$ can be derived from the peak electron density, $NmF2$, units in el/m^3, through the relationship

$$NmF2 = (foF2/8.98)^2 \tag{3.2}$$

In this test, one can assess the error of the RO results by calculating the distribution of the relative difference with respect to ionosonde measurements:

$$\Delta r_{foF2} = \frac{foF2_{RO} - foF2_{ionosonde}}{foF2_{ionosonde}} \tag{3.3}$$

To compare the results of tests described before, we will use the 68% and 95% percentiles from the distributions of the target quantities as metrics. Those percentiles approximately correspond to one and two standard deviations of a Gaussian distribution, respectively. In previous studies, the root mean square (RMS) of absolute or relative errors has been used to calibrate the improvement achieved by different methods. Although the RMS is an adequate metric when the error distribution is close to a Gaussian, its value can be significantly affected if the distribution has long tails with a few outliers giving extremely large error values compared with the bulk of the error distribution. Instead, the percentiles provide an unambiguous statistical measure of the true shape of the error distribution. Moreover, in the presentation of the results, it will be shown that the distributions of the target quantities analyzed are clearly non-Gaussian.

From the value of the percentiles of the target quantity derived from the different methods considered, the % of improvement, W, of a given method "B" for EDP retrieval with regard to another method "A" can be quantified as follows:

$$W = 100\frac{P_{68}(A) - P_{68}(B)}{P_{68}(A)} \tag{3.4}$$

$P_{68}(A)$ and $P_{68}(B)$ being the corresponding 68% percentile of the target quantity derived after application of the methods A and B, respectively. Since lower values of of the 68% percentile correspond to a more centrally concentrated distribution, they reflect a better performance of the corresponding method in a statistical sense. Thus, the W parameter measures the typical percentage of error reduction, as reflected by the 68% percentile of the error distribution, that is achieved by the method having better performance in the comparison.

3.2.2 Data set

As the data set for the study, we have used ROs observed by the COSMIC constellation of LEO satellites. 2014, it is the solar maximum, when the ionospheric conditions are more demanding because of higher solar activity. Hence, the data of observed ROs during 180 days of 2014, evenly distributed, has been collected from the Cosmic Data Analysis and Archive Center and processed to retrieve nearly 1.56×10^5 EDPs for each of the different methods analyzed in this chapter. The altitude of the COSIMIC satellite orbits is around $800km$, the maximum altitude reached by the EDPs used in this study from 740 to $860km$. All the profiles were retrieved down to a minimum altitude of $80km$ when possible, selecting profiles according to an F2-layer peak altitude ranging from 150 to $450km$. In these conditions, as it was shown by [4], the retrieved EDP is essentially sensitive to the electron distribution below the satellite altitude, i.e., the effects of the electron content above the LEO satellite almost negligible in the EDP finally obtained.

Besides, more than 1.86×10^4 measurements of F2-layer peak from 48 ionosondes around the world for the whole year of 2014, have been collected from the Digital Ionogram DataBase of Global Ionospheric Radio Observatory [30], as the reference to check the accuracy of RO retrievals using different methods. All the ionosondes are located within the longitude range $[-130^o, 130^o]$. Among them, 12 ionosondes are distributed in Europe.

3.3 Comparison results

Since the performances of the TEC-aided retrieval methods strongly depend on the accuracy of the TEC values, the present study will focus not only on worldwide results but also on the results over the European region, where it is known that the TEC from GIMs is more accurate, due to the existence of a dense network of ground receivers.

As commented on in the introduction, in order to perform a reliable comparison of the quality of the retrievals calculated with different TEC-maps, it is important to define common criteria. According to [32], the GAGE GIMs were computed using permanent receivers located within the longitude range $[-130^o, 130^o]$. Thus, the Global scale is set using that longitude range, while Europe scale is set as longitude $[-10^o, 50^o]$ and latitude $[30^o, 60^o]$.

3.3.1 Accumulated Error in RO retrievals

EC_{100}

To avoid the contamination by outliers in the distribution, it is important to apply a filtering to exclude extreme values, hereafter named as outlier filter. For the quantity EC_{100}, $[-1,\ 1]$ $(TECU)$ is used to select the reasonable data set. In general, this process never excludes more than a few percent of the original data.

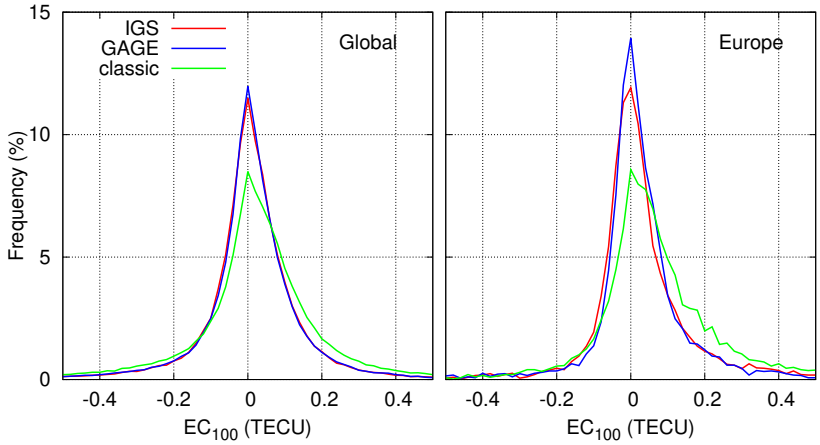

Figure 3.1: Histograms of the distribution of EC_{100} derived by three different methods. Green line: EC_{100} from RO retrievals using classic method; red line: SM aided by IGS GIM; blue line: SM aided by GAGE GIM.

Figure 3.1 depicts the histogram of the EC_{100} values obtained from the three methods considered: the classic approach, SM aided by IGS GIMs and SM aided by GAGE GIMs. The left panel shows global results, i.e., based on the ROs whose F2-layer peaks located inside the global range. While in the right panel, one can see the results of the comparison for ROs observed over Europe. From both plots, one can find that EC_{100} obtained using SM is more centralized around zero than the one using classic method. Moreover, in Europe, the results from SM aided by GAGE maps are obviously better than the one using IGS GIMs. Besides, from these histograms, one can find the interval used as outlier filter for EC_{100}, i.e., $[-1,\ 1]$ $(TECU)$, is a reasonable choice.

Region	Number ($\times 10^3$)	Classic		IGS GIM		GAGE GIM	
		68%	95%	68%	95%	68%	95%
Global	104.2	0.141	0.463	0.096	0.326	0.097	0.338
Europe	5.4	0.148	0.508	0.090	0.394	0.081	0.357

Table 3.1: Comparison of the percentiles of the EC_{100} distributions, in $TECU$, from the different techniques

Table 3.1 shows the 68% and 95% percentiles of the distributions of the EC_{100} parameter, represented in Figure 3.1, for the different methods and for the global and European regions. The total number of ROs considered in each region is given in the second column. There is a clear improvement with respect to the classic approach when the SM uses the IGS GIM and the further improvement increases when the GAGE GIMs are used. Specifically, SM with IGS GIMs improves the results of the classic approach, according to parameter W defined in equation 3.4, by nearly 39% in Europe and 32% globally, while the improvement using the SM with the GAGE GIMs is 45% in Europe and 31% globally. Therefore, comparing the results of the SM using different GIMs, the GAGE GIMs are 10% better in Europe than the IGS GIMs but globally, no improvement is observed. This last result is not surprising since the global results include poorly sampled regions over the oceans, where both types of GIMs have similarly low accuracy.

Equatorial Plasma Caves

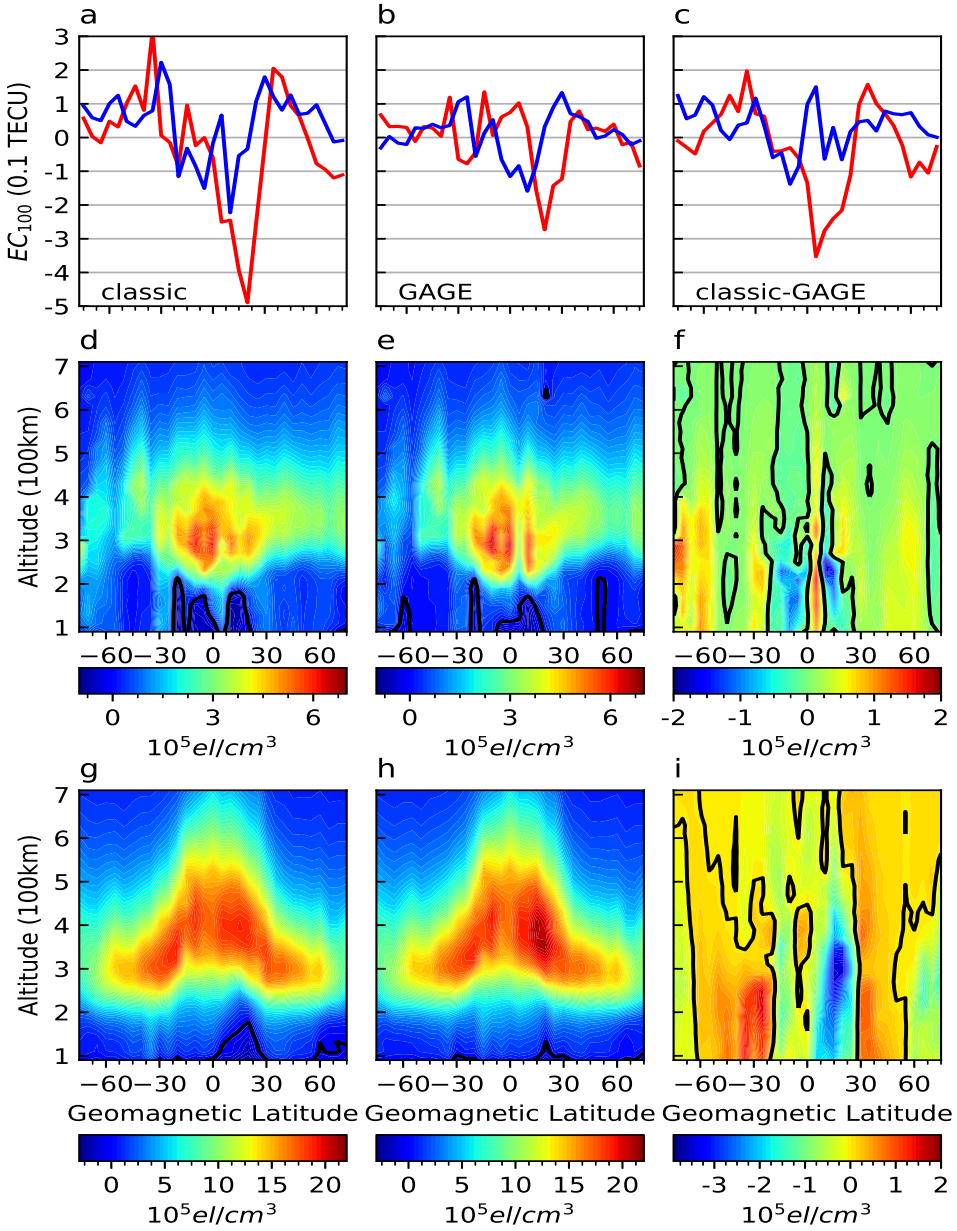

Figure 3.2: Mean EC_{100} for March 2014 LT between 0 h and 2 h (blue solid lines) and between 13 h and 15 h (red solid lines) from (a) the classic approach, (b) the SM with GAGE GIMs and (c) the difference between Figures 4a and 4b. Zonal mean electron density distribution for March 2014 LT between 0 h and 2 h for (d) the classic approach, (e) the SM with GAGE GIMs and (f) the difference between Figures 4d and 4e. (g-i) The same as Figures 8d-8f but for results between 13 h and 15 h. Black contour lines represent zero electron density.

EC_{100} measures quantitatively the error in the retrievals by looking the EC at the bottom part of the profiles which should be close to zero. The top panel of Figure 3.2, plots (a), (b) and (c) depict, respectively, the mean EC_{100} at different geomagnetic latitudes from the classic approach, the SM aided by GAGE GIMs and their difference, calculated for RO retrievals in March, 2014 and for two Local Time (LT) intervals just after noon (red curves) and after midnight (blue curves). Compared with the very small value expected for EC_{100}, plot (a) shows clear overestimations in mid-latitude regions, while significant underestimations are seen near magnetic equator. Indeed, as it is reported in [23] and [21], the classic approach cannot account for the large gradients in the low latitude regions and produces a clear underestimation in the equatorial region and an overestimation in the surrounding mid-latitude regions as observed in plot (a). As seen in plot (b), the deviations from the small value of a few hundredth of $TECU$ expected for EC_{100} are clearly mitigated in the retrievals from the SM aided by the GAGE GIMs. The reduction of these deviations are quantified in plot (c), where one can see a maximum reduction of nearly $0.2TECU$ at midnight and close to $0.4TECU$ at noon, reducing more than half of deviation brought by classic Abel inversion.

The average electron density distributions for midnight and noon periods during March 2014 are presented in the middle and bottom rows of Figure 3.2. It is a common representation for illustrating the diminision of artificial plasma caves, as shown in [23], [21]. In agreement with the EC_{100} results shown in the top row, the artificial plasma caves around the equator observed in the EDP retrievals from the classic approach – plots (d) and (g) for midnight and noon, respectively, are substantially mitigated when using the SM – plots (e) and (h) for midnight and noon, respectively. The electron density values derived for the classic approach are consistent with the values obtained in previous studies [21] for the same LT intervals during September 2013, a period with similar ionospheric activity as March 2014. However, in plot (f) – the difference between plots (d) and (e), one can observe that the difference between the classic approach and the SM retrievals is close to $2 \cdot 10^5$ el/cm^3 for altitudes below 200 km in the low latitude region during midnight. This is one order of magnitude larger than the corresponding values derived in [21]. On the other hand, during noon, the corresponding reduction of the artificial plasma caves observed in plot (i) – the difference between plots (g) and (h), is a factor 4 to 8 larger than reported in that previous study for altitudes around and below $300km$. Hence, we conclude that the SM using more precise two-layer TEC maps and non-oblique EDPs clearly improves the classic approach, providing a more accurate description of the large electron density gradients that characterize the equatorial region during the equinox of 2014.

3.3.2 Comparison between RO retrievals and ionosonde measurements

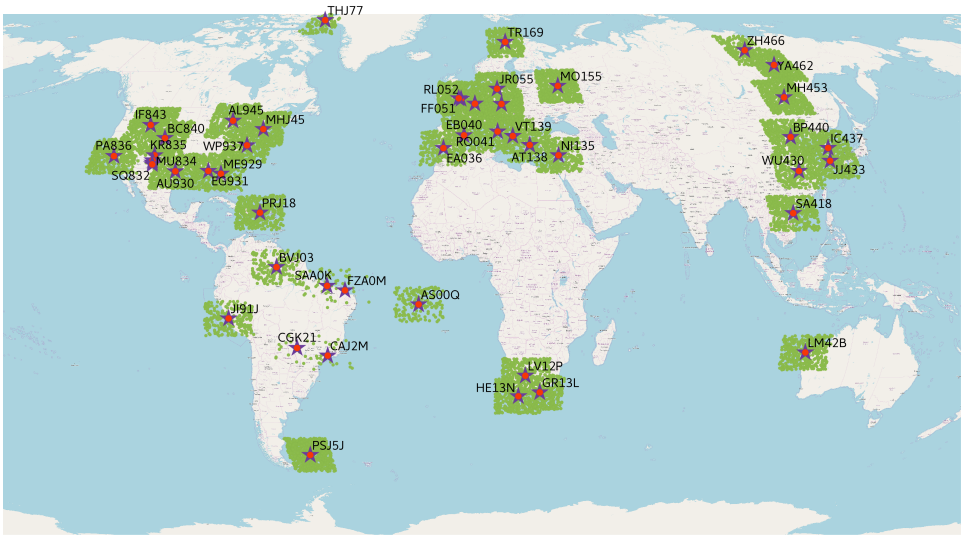

Figure 3.3: Map with the locations of the ionosondes (stars) and the collocated ROs (green dots) considered in the present study.

Figure 3.3 shows a map of the ionosonde locations with the ROs whose F2 layer peaks observed within some fixed spatial and temporal window. To mitigate the LoC error in the comparisons, we have considered only the subset of ROs yielding an F2-peak located inside the region with a longitude difference smaller than $\Delta\lambda = 8^o$ and a latitude difference below $\Delta\phi = 5^o$ with respect to the ionosonde location. Moreover, comparisons were done only when the time difference between RO and ionosonde observations was less than 0.5 hours. In this comparison, the ionosonde measurements are treated as the reference. Thus, the Global/European data sets are defined according to the locations of ionosondes.

The $foF2$ values derived from EDPs will be compared with ionosonde measurements to check the quality of the RO inversion. The outlier filter for the comparison is set as $[-1, 1]$, i.e., those cases giving relative differences with regard to ionosonde measurements larger than 100% have been excluded from the distributions.

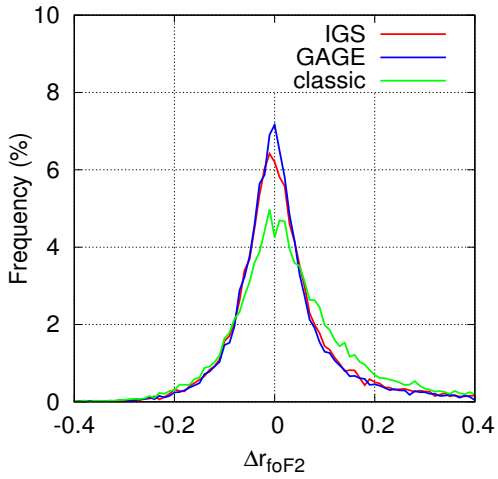

Figure 3.4: Histogram of the distribution of the relative error, with regard to ionosonde measurements, in the retrieved foF2 values from the different methods to obtain the EDP

Figure 3.4 shows the histogram of relative differences Δr_{foF2}, see equation 3.3, between RO inversion results from the different methods considered, with respect to the ionosonde measurements at the global scale. From this figure, we can see that there is a significant improvement from classic approach to SM inversion using IGS GIMs, while this improvement is even greater when using GAGE GIMs.

Two quantitative maps of errors corresponding to individual ionosonde are presented in Figure 3.5, where the 68% percentile of the distribution of Δr_{foF2} is represented using a colour code. The top one is the map of result using the IGS GIM and the bottom one is the one from GAGE GIM. Both figures show the some level of consistence. As it can be seen, better results are obtained in mid-latitude well-sounded areas (such as Europe). While in the high latitude region and the region close to longitude 130^o, the results are worsen, which reflects the poorer quality of the GIMs in these regions. On the other hand, comparing the results in the top with those on the bottom map one can conclude that, the results with the GAGE GIMs are generally better than those using the IGS GIM.

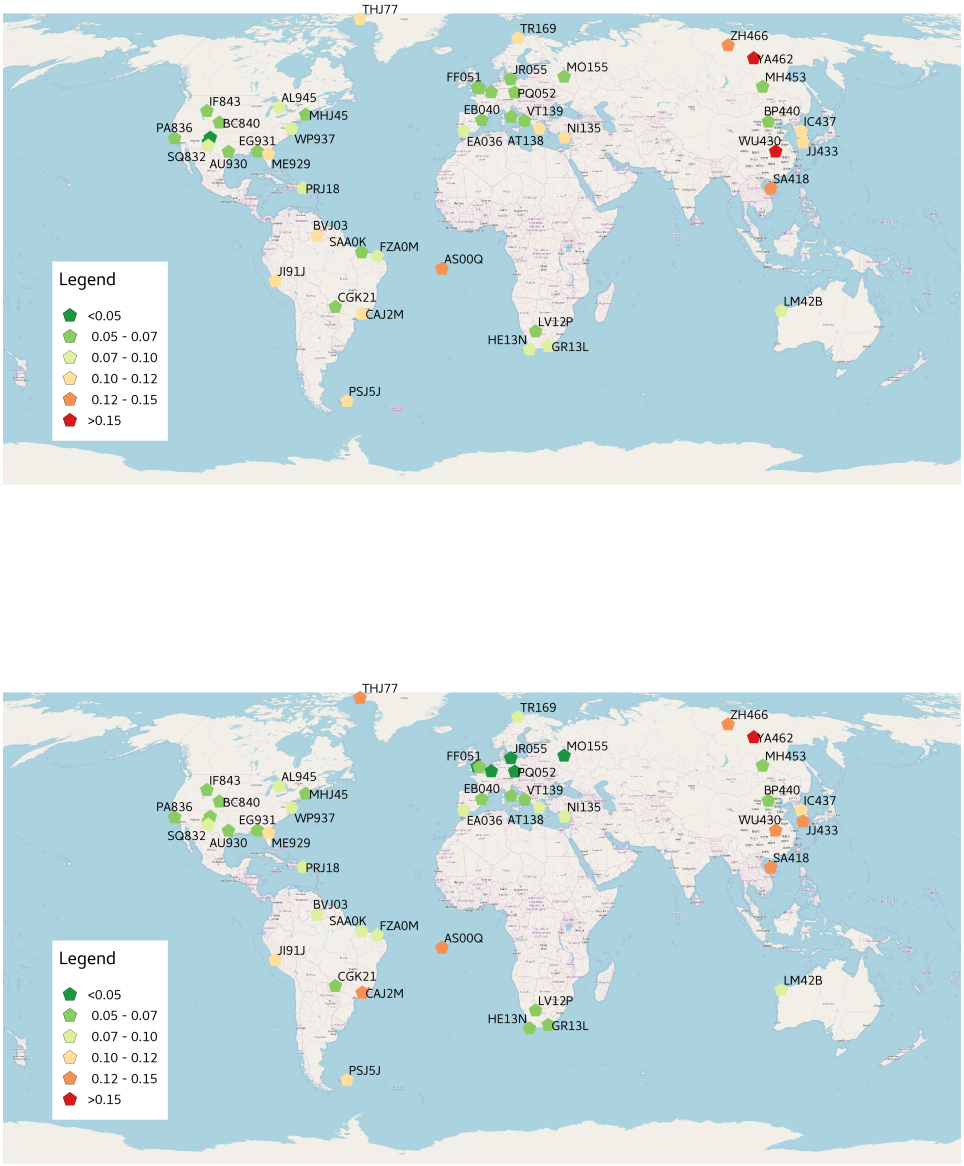

Figure 3.5: Map of the relative errors.
Top: IGS GIM; bottom: GAGE GIM

Tables 3.2 and 3.3 show the percentiles of the distributions of Δr_{foF2} and Δr_{NmF2}, respectively. The second column shows the total number of

collocated ionosonde–RO pairs. Note that one RO can be compared with two different ionosondes when they are located closely enough, particularly in the European region.

Region	Number ($\times 10^3$)	Classic		IGS GIM		GAGE GIM	
		68%	95%	68%	95%	68%	95%
Global	17.7	0.106	0.356	0.077	0.288	0.072	0.274
Europe	6.0	0.092	0.288	0.063	0.202	0.056	0.180

Table 3.2: Statistical comparison of the relative errors in foF2 for the different techniques

Region	Number ($\times 10^3$)	Classic		IGS GIM		GAGE GIM	
		68%	95%	68%	95%	68%	95%
Global	17.0	0.199	0.582	0.143	0.439	0.133	0.424
Europe	5.9	0.179	0.521	0.121	0.350	0.108	0.306

Table 3.3: The same quantities as table 3.2 for $NmF2$

Focusing in the results for the 68% percentile on $foF2$, the improvement achieved by the SM based on IGS GIMs in comparison with the classic approach for the global network of ionosondes is 27%, and 32% for the European network, while in the case of the GAGE GIMs, the corresponding improvement increases to 32% globally and 39% in Europe. Thus, in the global comparison, the use of a GAGE GIM improves the results, with respect to the use of an IGS GIM, by more than 6%, while the corresponding improvement in Europe is around 11%.

Besides, due to the quadratic relationship between critical frequency and peak electron density, when the error is small one should expect that the relative difference in the peak electron density is approximately equal to two times Δr_{foF2}. Indeed, this could be confirmed by comparing these two tables.

The values of the 95% percentile, reflecting the overall shape of the distribution, are also obtained. In all the cases, the 95% percentiles are approximately around three times larger than the 68% percentiles, which reflects the relevance of the tails in the error distributions that clearly deviate from a Gaussian distribution. For this reason, the use of the RMS to assess the performance of the methods seems not adequate.

3.4 Effects of the electron content above the LEO satellite

In this section, we will have a more detailed study about the mismodelling in TEC-aided methods.

3.4.1 Methodology

From the retrieved EDP, one can calculate the EC below the LEO, EC_{LEO}, by performing the following integral:

$$EC_{LEO}(\lambda, \phi) = \int_0^{h_{LEO}} N_e(\lambda, \phi, h)dh = \beta \times TEC(\lambda, \phi) \tag{3.5}$$

where

$$\beta = \int_0^{h_{LEO}} F(h)dh \tag{3.6}$$

As it was shown by [4], the EDP retrievals from an RO are essentially a representation of the EC below the LEO satellite orbit, while the EC above the LEO only affects the values of the retrieved EDP near to the LEO satellite altitude. Nevertheless, the EC over the LEO satellite orbit is a substantial fraction of the TEC, typically larger than 20–30% [25]. Thus, in order to apply self-consistently the SM technique, the TEC values used in equation 2.5 should be replaced by the values of EC_{LEO}, which better describe the true horizontal gradients in the region below the LEO satellite orbit. This mismodelling would be larger for LEO satellites at a lower altitude like, for example, the CHAMP satellite having nearly two times a lower altitude than the COSMIC satellites [27]. In order to address the impact of this mismodelling on the final EDP, we have used the two-layer GAGE GIMs to find an approximate value of EC_{LEO} as the sum of the EC contributions from the bottom ionospheric layer of the GIM, EC_{bottom}, plus some unknown fraction γ of the EC from the top-layer, EC_{top},

$$EC_{LEO}(\lambda, \phi) \approx EC_{bottom}(\lambda, \phi) + \gamma EC_{top}(\lambda, \phi) \tag{3.7}$$

The value of β from equation 3.6, estimated after inverting the RO using the $TEC = EC_{bottom} + EC_{top}$ from the GAGE GIMs, can be used to derive the parameter γ by means of the following equation:

$$\gamma = \frac{\beta \times TEC - EC_{bottom}}{EC_{top}} \tag{3.8}$$

The EC_{LEO} values obtained from equation 3.7 can be used to replace the original TEC used in equation 2.5, yielding a new derivation of the EDP that can be compared with the original EDP to assess the magnitude of the

mismodelling. According to equation 2.5, if the ratio between the EC_{LEO} and the original TEC from the GIM is nearly constant for all the locations covered by the RO, then differences will be found in the results obtained for the shape function $F(h)$ but not in the corresponding EDP.

3.4.2 Analysis

β and the accuracy of the EDP

The β parameter defined in equation 3.6 provides a measure of the ratio between the electron content below the LEO satellite orbit and the TEC, and hence, the mismodeling affecting the SM should be smaller when β is closer to unity. Figure 3.6 depicts the histograms of the distribution of β values when the EDPs are derived using the SM aided by the IGS (in red) or GAGE GIMs (in blue). In both cases, the values of β are clearly smaller than one.

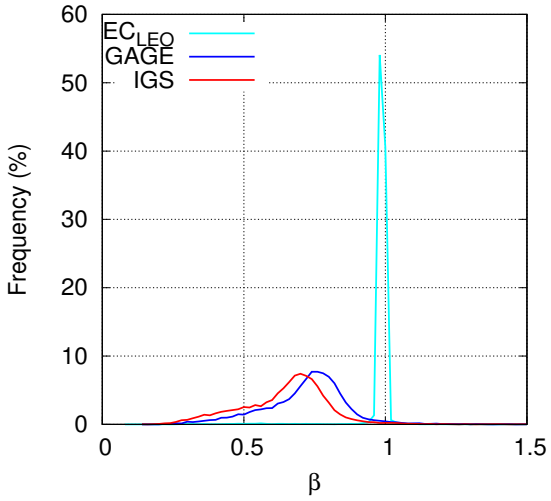

Figure 3.6: Distribution of β values obtained when using different GIMs to aid the SM: IGS GIM (red), GAGE GIM (blue), and EC_{LEO} calculated after the derivation of γ parameter for each RO (cyan)

From the value of β, one can calculate the γ parameter for each RO following equation 3.8 and the EC_{LEO} according to 3.7, from which a new retrieval of the EDP can be obtained after substituting the original TEC in equation 2.5 by EC_{LEO}. The cyan curve, shown in Figure 3.6, corresponds to the β histogram derived after those new EDPs are calculated with the SM. As one can see, the new β histogram is mostly peaked around one.

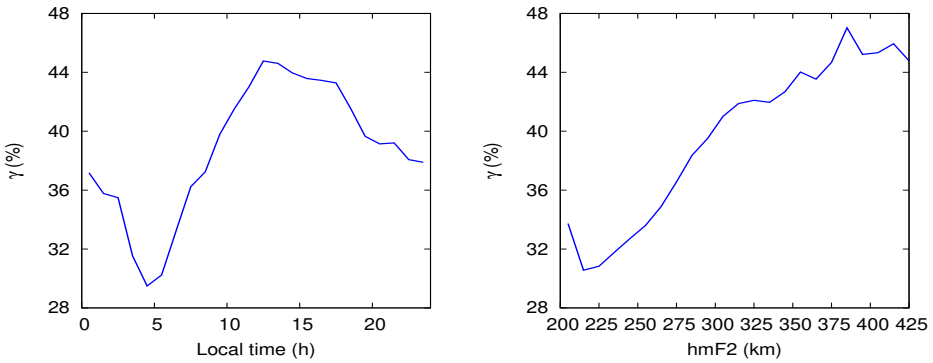

(a) local time vs γ (b) $hmF2$ vs γ

Figure 3.7: Dependency of γ with respect to the local time (left) and the $hmF2$ (right) for the global data set of ROs used in previous figure

Figure 3.7 shows the magnitude of the variations of the mean γ as a function of the local time (left) and the peak altitude $hmF2$ (right). From this figure, it can be seen that the contribution of EC_{top} in equation 3.7 to the EC_{LEO} approximately varies from 28% to 48%. The left panel shows a clear day/night dependency associated to the F2 layer deployment after sunrise. Indeed, this deployment starts at about $5h$ of local time, reaching a maximum around noon. During this deployment the contribution of the EC_{top} to the EC_{LEO} becomes more important because the F2-peak altitude increases, this trend is more evident in the right panel of Figure 3.7, where it can be observed that, in general, the higher the value of $hmF2$, the larger the contribution of EC top from the GAGE GIM to the EC_{LEO}.

However, there is little difference between the error distributions of $foF2$ values for the European region obtained with the SM using the EC_{LEO} or the original TEC from GAGE GIMs, as shown in Figure 3.8. This result strongly indicates that EC_{LEO} and TEC values used in equation 2.5 are nearly proportional at all tangent points sampled by a given RO in most cases. Thus, this finding implies that, in terms of the retrieved $foF2$, there is only a small mismodelling affecting the final EDP retrieval when using TEC from GAGE GIMs in the SM to describe the horizontal gradient in the electron content.

On the other hand, from the shape of the β distribution shown by the cyan curve in Figure 3.6, one can select the ROs yielding a β value around unity as the ones providing the most reliable EDP retrieval. Table 3.4 shows a quantitative assessment of the 68% percentile of the $foF2$ distributions of relative error that are derived if one selects only the ROs that, after

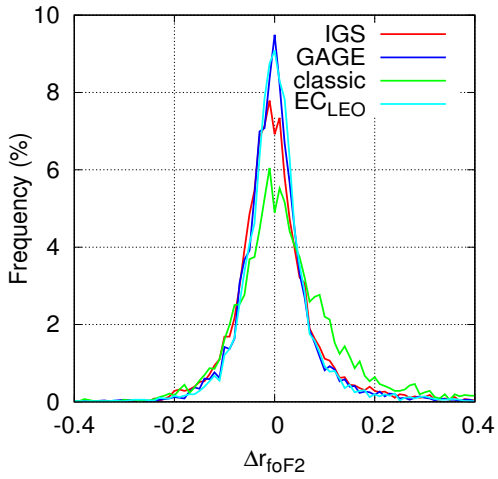

Figure 3.8: Histograms of the relative error of the $foF2$ for the European region: using spherical symmetry in green, SM with IGS GIM in red, SM with GAGE GIM in blue, and SM with EC_{LEO} obtained with varying γ according to equation 3.8 in cyan

applying the SM aided by the EC_{LEO} values, yield a value of β in a restricted range around unity. One can see that the improvement of the SM that uses EC_{LEO} is only a few per cent with respect to the SM using the GAGE GIM. However, all the techniques improve their performance with regard to the results presented in Table 3.2 for Europe, when the narrow β-filter is applied, while the relative improvements between the different methods are maintained. This finding implies that the filtering applied to ROs, according to a value of β around unity, provides a quality control of the mismodelling of the SM affecting the EDP retrievals, selecting a more accurate set of profiles than the original set used in Table 3.2.

Filter range	Number ($\times 10^3$)	68% percentile Classic	IGS	GAGE	EC_{LEO}
all β	6.0	0.092	0.063	0.056	0.054
$0.95 \leq \beta \leq 1.05$	5.6	0.087	0.060	0.053	0.050

Table 3.4: Statistical comparison of the results for foF2 in the European region when the ROs are filtered according to β values derived with the SM using EC_{LEO}

Two adjacent ionosondes and RO retrievals

Given the small values of the 68% percentile achieved by the SM when compared with ionosonde measurements in Europe, we have considered two closely located ionosondes in Europe, Fairford $(51.7^oN, 1.5^oW)$ and Chilton $(51.5^oN, 0.6^oW)$, to see if the observed differences between their $foF2$ measurements are similar to the errors achieved by the SM. The baseline of these two ionosondes is less than $70km$, which is clearly smaller than the window used in the comparison of ROs with ionosondes.

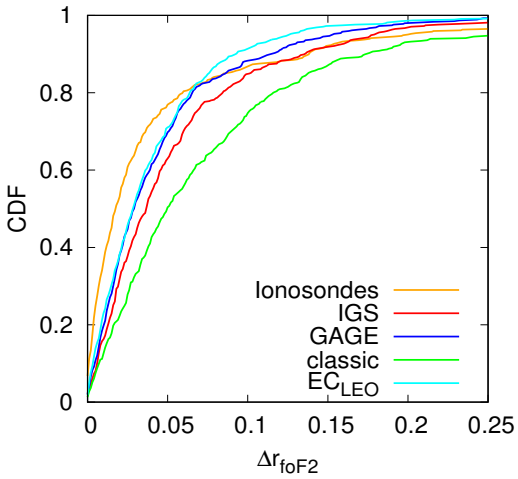

Figure 3.9: CDFs inferred from relative error distributions of $foF2$ values from two near ionosondes in Europe and from the different methods of EDP retrieval selecting profiles with β in [0.95, 1.05]

Figure 3.9 shows the cumulative distribution function (CDF) of the Δr_{foF2} between the Chilton ionosonde measurements and the Fairford ones, orange line. In the same figure we show the corresponding CDFs of the Δr_{foF2}, with regard to Fairford measurements, achieved by the different methods previously considered. These comparisons are done for a total number of 510 collocated measurements of the $foF2$ peak. From this figure, one can clearly observe that the SM based on the GAGE GIMs, cyan and blue curves, yield errors of magnitude remarkably similar to the ones observed between the ionosonde measurements, orange curve. Both GAGE GIM methods and ionosonde observations achieve relative errors smaller than 7% in nearly 80% of the cases.

As a final remark, it must be emphasized the importance of analyzing the full distribution, or the corresponding CDF, of relative errors in order

to properly compare the performance of different methods. The percentiles of the distributions provide a metric that reflects unambiguously its shape and, in particular, they evaluate more accurately the nominal error in a statistical sense. On the contrary, the use of an average parameter like the RMS is not able to reproduce all the specificities of the full error distribution, particularly when it is not a Gaussian one, like in the present case. This is clearly illustrated by the differences between the percentile values and the RMS that are presented in Table 3.5 for the different CDFs represented in Figure 3.9. One can see that in all cases, the 95% percentiles are two times larger than the RMS values, the latter being systematically larger than the 68% percentile, although the relative increase is not the same for all methods. In particular, according to the RMS, the SM using GAGE GIMs or alternative EC_{LEO} values will outperform the error from ionosonde measurements, while the 68% percentile shows that for the main bulk of the distributions, or nominal errors, this is not really the case. The RMS is clearly affected by a few per cent outlier values, from very large errors as indicated by the large 95% percentile value and, consequently, the RMS does not describe the bulk of the error distributions shown in the previous figures. Instead, the 68% percentile compares nominal errors from all the methods, not being significantly affected by the presence of a few outliers from the tails of the error distributions.

METHOD	68%	95%	RMS
Ionosondes	0.035	0.200	0.090
Classic	0.087	0.257	0.121
SM IGS	0.059	0.179	0.088
SM GAGE	0.049	0.154	0.077
SM EC_{LEO}	0.047	0.127	0.072

Table 3.5: Percentiles and RMS values derived from the CDFs presented in Figure 3.9

3.5 Conclusion

The main goal of this chapter is to show the impact of the accuracy of the GIMs used by the SM Abel inversion technique on the quality of the RO retrieved EDP. This quality has been assessed not only by comparing two different types of GIMs but also by considering regions where the performance of the GIMs is expected to be different. Previously published studies ([15], [16]; [13]; [23]) suggested that the improvement of the SM, with regard to the classic approach, is small and/or essentially due to the LoC error, which is substantially mitigated when the SM is used. However, our results do not agree with this interpretation.

The present study has demonstrated that the SM provides significantly greater precision than the classic approach based on the spherical symmetry assumption. First, through the EC_{100} test, which is not affected by the LoC error, it has been shown that, according to the 68% percentile of the error distributions, the results using SM aided by GAGE GIMs can improve by 31% world-wide and 45% over Europe the results obtained using the classic approach. Moreover, the SM has been shown to substantially mitigate the artificial plasma caves produced by the large ionospheric gradients in the equatorial region when the classic approach is used. Second, by comparing with ionosonde measurements, similar improvements as those with the EC_{100} test are obtained. Indeed, we have found relative errors using the SM that represent a 32% improvement world-wide and a 39% in Europe with respect to the results using the classic technique. Finally, introducing a quality criterion based on selecting the ROs yielding a value of β around unity, it has been shown that the SM aided by GAGE GIMs can achieve relative errors, at the 68% percentile, nearly 5% in the retrieved $foF2$, similar to the errors obtained when comparing the results from two nearby ionosondes. This implies that using the SM with GAGE GIMs in well sounded areas, one can retrieve the peak electron density from ROs with an accuracy similar to that of ionosonde measurements, with errors smaller than 7% in nearly 80% of the cases in the European region during 2014.

Chapter 4

Modelling of topside ionosphere and bottomside plasmasphere from RO retrievals

4.1 Introduction

The O^+/H^+ transition height hu is an important parameter characterizing ion composition, which it is defined as the altitude where densities of O^+ and H^+ are equal. It indicates the separation between ionosphere and plasmasphere. Due to the highly dynamic characteristics of ionosphere and plasmasphere, the transition height is not static.

hu could be accurately determined from *in-situ* observations of satellites. [38] used observations from both the Bennett Ion-Mass Spectrometer (BIMS) and the Retarding Potential Analyzer (RPA) on board the Atmosphere Explorer E satellite to derive transition height. In [39], it was introduced the NASA sponsored project, Coupled Ion Neutral Dynamics Investigation (CINDI), which could provide number density of the thermal ions in the ionosphere using the RPA and an Ion Drift Meter (IDM), carried by the Communications/Navigation Outage Forecast System (C/NOFS) satellite launched in April, 2008. The measurements are only constrained around equator due to the low inclination (13^o) of the satellite orbits. Hence, it is not possible to get a global picture of the transition height. Besides, it is inaccessible to the large diurnal, seasonal, yearly variation of the transition height due to the limited measurements. The Incoherent Scatter Radar (ISR) measurements are also widely used in many studies. [45] studied transition height measured from the incoherent scatter radar at Arecibo during the periods from 1992 to 1994. [43] used the observations from ISR

in Kharkiv, Ukraine for hu study during the equinoxes of 2006–2010. The same as the *in-situ* observations on satellites, the ISR data are also constraint to local regions.

Hence, during the last decades, many studies have investigated to derive hu indirectly from topside electron density profiles, which could be obtained based on a variety of data sets. There are extensive topside ionospheric observations available from the swept-frequency sounders carried on the polar-orbiting satellites Alouette 1 and 2, ISIS 1 and 2 (launched in 1962, 1965, 1969 and 1971, respectively). In general, there are two approaches to determine the transition height from topside profiles. The first way is based on the use of some theoretical model. [51] used analytical functions to fit the topside profiles obtained from those sounders by iteratively changing the parameters like temperature, temperature gradient and transition height to achieve the best fit. Meanwhile, hu was obtained during the iteration. The other way of deriving hu is based on shape of the topside profile to build some empirical models. Basically, the O^+ density profile is determined from the topside ion profile by model fitting, then the transition height is derived at the altitude where the O^+ density is equal to half of the ion density [47], [44].

As we discuss in previous part of the thesis, the EDPs of ionosphere could be obtained from the RO measurements, till the altitude of LEO satellite orbit. Using SM, the RO retrievals have high accuracy. Thanks to the deployment of Constellation Observing System for Meteorology, Ionosphere and Climate (COSMIC/FORMOSAT-3), there are abundant RO measurements. Based on the COSMIC RO data, [4] introduced Simplified Topside Ionosphere plus Protonosphere model (STIP model) to fit the topside profile retrieved from RO measurements and separate the ionospheric and plasmaspheric contributions from GPS TEC. In this methodology, hu could be derived from the RO empirical data. Different from the single component model, where only O^+ is modelled, used in other studies, like in [44], STIP model is a two-components model, i.e., both topside ionosphere and bottomside plasmasphere are modelled.

In the following sections, STIP model is described in detail and applied to some sample data in 2008. The derived results are checked in different ways to validate the model. Finally, the STIP model is used to fit the RO retrievals in 2007 and 2014 to get transition height, hu, and scale height, hs. And the climatological study about hs and hu is carried out based on the model derived results.

4.2 Methodology of separating Ionospheric and Plasmaspheric contribution of TEC

4.2.1 STIP model

STIP model can be used to fit the upper part of shape function $F_{RO}(h)$, that $F_{RO}(h)$ is obtained from RO observations with equation 2.5. The upper part of $F_{RO}(h)$ corresponds to topside ionosphere/bottomside plasmasphere region.

$$F_{stip}(h) = F_{O^+}(h) + F_{H^+}(h) = A \cdot exp(-h/hs) + B \tag{4.1}$$

STIP model is defined as equation 4.1, which considers a plasma consisting only of O^+ and H^+ in the upper part region. Charge neutrality is assumed, hence the electron density is equal to the sum of the O^+ and H^+ densities, $Ne = n(O^+) + n(H^+)$. Besides, the STIP model is based on the assumption that the density of the dominant ion constituent is approximately equal to the electron density in the corresponding region, i.e., $Ne(ionosphere) = n(O^+)$ and $Ne(plasmasphere) = n(H^+)$. According to the basic concept in SM introduced in chapter 2, shape function $F(h)$ is obtained through dividing Ne by a horizontal quantity. Hence, the same principle could be applied to shape function, i.e.,$F_{ionosphere}(h) = F_{O^+}(h)$ and $F_{plasmasphere}(h) = F_{H^+}(h)$. A, hs are the factor that determines ionospheric proportion (O^+ ion) and ionospheric vertical scale height in the model, respectively. Meanwhile, B relates to the H^+ ion density in topside ionosphere/bottomside plasmasphere regions. It is worthy mentioned here that the scale height for the H^+ is expected to be larger than 10^3 km, thus it is a reasonable assumption to take B as a constant in topside ionosphere/bottomside plasmasphere regions. The definition of upper part of $F_{RO}(h)$, which is used for fitting, is from some altitude h_{bc} above F2 peak altitude, $hmF2$, till several kilometres h_{tc} below the LEO satellite altitude, h_{LEO}.

After using STIP model to achieve a the best fit to the topside electron density, the parameters A, B, hs are obtained. Hence, the ionospheric and plasmaspheric portions along the altitude are known. Following the definition of transition height hu, where the O^+ and H^+ has the same portion of the electron density, i.e., $n(O^+) = n(H^+)$, based on equation 2.4, we can also derive:

$$A \cdot exp(-hu/hs) = B \tag{4.2}$$

Hence, we can get hu by solving the above equation,

$$hu = hs \cdot ln(A/B) \tag{4.3}$$

4.2.2 $IONf$

The concept of $IONf$ was introduced in [25]. It represents the fractional contribution of the ionosphere to vertical TEC, and it is expressed as:

$$IONf = \frac{EC_{ion}}{TEC} \tag{4.4}$$

While, TEC is the sum of ionospheric and plasmaspheric electron content, EC_{ion} and EC_{pl}, i.e., $TEC = EC_{ion} + EC_{pl}$. Hence, from the definition, the value of $IONf$ should be within [0, 1].

On the other hand, based on the assumption that, there is only ionospheric contribution to profiles from the minimum altitude sampled by the RO till the lower cutting point for the interval of altitudes in the topside ionosphere/bottomside plasmasphere, $hmF2 + h_{bc}$, $IONf$ can be calculated by following equation 4.5 with the fitting parameters, the same as equation (5) in [25].

$$\begin{aligned} IONf = & \int_{h_0}^{hmF2+h_{bc}} F_{RO}(h) \cdot dh + \int_{hmF2+h_{bc}}^{+\infty} A \cdot exp(-\frac{h}{h_s}) \cdot dh = \\ & \int_{h_0}^{hmF2+h_{bc}} F_{RO}(h) \cdot dh + h_s \cdot A \cdot exp(\frac{-(hmF2 + h_{bc})}{h_s}) \end{aligned} \tag{4.5}$$

Here, h_0 is the minimum altitude sampled by the RO (typically around 100 km). Once the $IONf$ is obtained, we can get the EC_{ion} and EC_{pl} with known TEC.

It is worthy to point out here that $IONf$ is a different concept from β defined in equation 3.6, which was introduced in chapter 3.

- β represents the integration of shape function $F(h)$ below the LEO satellite orbit, i.e. it is ratio between electron content below the LEO and GPS TEC.
- $IONf$ reflects the ionospheric portion of GPS TEC, i.e. excluding the plasmasphere.

In other words, β includes part of the plasmasphere below the LEO height, while $IONf$ takes into account part of the ionosphere above the LEO height. Hence, the quantities of these two parameters are different. When the transition height, hu, is below the LEO height, the parameter β can include a significant part of the plasmasphere. i.e., β will be greater than the $IONf$.

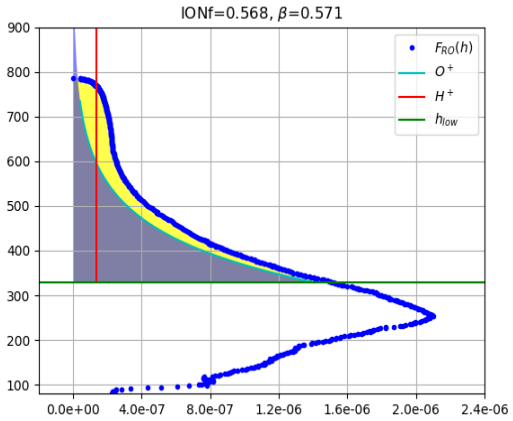

Figure 4.1: An example showing the difference between $IONf$ and β. Blue dots are the shape function retrieved from RO measurements. The green horizontal line is the low limit of upper part of RO profile for fitting. The cyan curve is the ionospheric profile and the red vertical line is the plasmaspheric one. The grey shadow represents the plasmaspheric portion in the topside ionosphere. And the yellow filled region is the difference between the RO retrieval and ionospheric contribution.

Figure 4.1 is an example showing the difference between $IONf$ and β. The RO was measured at midnight in January, 2007. The blue dots represent the shape function $F_{RO}(h)$ retrieved from the RO measurement using SM with the assistance of IGS GIM. The horizontal green line is the low limit of upper part of RO profile used for fitting. I.e., below this altitude, there is only ionospheric portion in the profile. While the region above the green line is defined as the topside ionosphere, which consists of both ionospheric/-plasmaspheric portions, and it is fitted with the STIP model to separate the ionospheric contribution, cyan line, and plasmaspheric one, red vertical line. The intersection of cyan and red lines is the transition height, hu. In this example, hu is lower than the LEO height, and there is a significant portion of plasmasphere below LEO height, shown as the yellow patch between the RO profile (blue dots) and ionospheric portion (cyan line). Hence, in this case, β, 0.571, is slightly bigger than $IONf$, 0.568.

4.2.3 Chemical Equilibrium Plus Diffusion Equilibrium H^+ Model (CPDH model)

In [71] it was addressed that the H^+ number density in low altitudes is mainly controlled by the chemical equilibrium, while in high altitudes the main controlling factor is diffusive equilibrium. In Field Line Interhemispheric Plasma model (FLIP model), a physical model presented in [69], the

true H^+ profile is a combination of the chemical equilibrium profile at low altitudes and the diffusive profile at high altitudes, with a smooth transition between the two from 500 to 1200 km, this range varies as a function of solar flux. Besides, [44] pointed out the maximum of the H^+ altitude profile is slightly above the transition height and there the H^+ density is practically constant with altitude.

The STIP model assumes that the plasmaspheric portion is a constant along the altitude from some height above the F2-layer peak, $hmF2 + h_{bc}$, i.e., the developing process of the plasmasphere along the altitude is ignored. From the discussion above, we can find there is a simplification in STIP model, which is the ignorance of the developing process of the plasmaspheric portion in topside ionosphere/bottomside plasmasphere region. In order to check the impact of this simplification on the final results, we introduce CPDH model based on STIP model:

$$F(h) = Aexp(-h/hs) + F_{H^+}(h) \tag{4.6}$$

where $F_{H^+}(h)$ is expressed as following equation:

$$F_{H^+}(h) = \begin{cases} 0, & h \leq 200 \\ (1-r) \cdot b1 \cdot exp((h-200)/hp) + r \cdot b2, & 200 < h < hz \\ b2, & h \geq hz \end{cases}$$

with

$$r = (h - 200)/(hz - 200)$$

The only difference between this model and STIP model happens in the plasmaspheric portion. Here, the plasmaspheric portion is not a constant, but its value varies along the altitude. The $F_{H^+}(h)$ is defined as different functions in three altitude regions. Below 200 km, there is no H^+ contribution. hz is the transition altitude that the controlling factor of H^+ number density is switched from chemical equilibrium to diffusion equilibrium, within the range [500 km, 1200 km]. In the range between [200 km, hz], in order to achieve a smooth transition between chemical equilibrium and diffusion equilibrium, a combination of the chemical and diffusive components is used, with the weight ratio r, which is linearly varying along the altitude. Here, $b1 \cdot exp((h-200)/hp)$ is the chemical part, $b1$ is the scale factor related with H^+ number density in chemical equilibrium and hp is the scale height with an effective mass of 7 a.m.u., which was described in [40]. While $b2$ represents the diffusive part. Above hz, only diffusive component is considered, i.e., $b2$.

The chemical equilibrium means the production rate and loss rate of exchange reaction, $O^+ + H \leftrightarrow H^+ + O$, are the same, i.e., there is no net production of H^+. H^+ number density at low altitude, where it is controlled by chemical equilibrium, could be expressed as the following equation, the same one as equation (5) in [71]:

$$n(H^+) = \frac{2.5 \cdot n(O^+) \cdot n(H)}{2.2 \cdot n(O)} \sqrt{\frac{Tn}{Ti}} \tag{4.7}$$

where, $n(H^+)$ and $n(O^+)$ are the H^+ and O^+ number density, respectively. And $n(H)$ and $n(O)$ are the neutral hydrogen and oxygen number densities. Tn is the neutral temperature and Ti is the ion temperature. In this region, comparing the variation scale of the H and O number densities, the variation of quantity Tn/Ti could be neglected, i.e., it could be treated as a constant. Assuming the atmospheric constituents H and O to be distributed exponentially in the region where O^+ is the predominant ion, equation 4.7 leads to the relationship [40]:

$$n(H^+) \propto exp(hr/hp) \tag{4.8}$$

In this relationship, hp is the scale height with an effective mass of 7 a.m.u., and hr is the reduced altitude, which is replaced with the $(h - 200)$ in CPDH model. From this relationship, we can see that the H^+ number density increases exponentially along the altitude in chemical equilibrium.

While, in diffusion equilibrium, the H^+ number density follows the relationship [36]:

$$n(H^+) \propto exp(-h/hs_{pl}) \tag{4.9}$$

The hs_{pl} is the plasmaspheric vertical scale height. Comparing to the ionospheric scale height hs in equation 4.6, it is much larger, more than 10^3 km. The interval of altitudes considered in the model is far smaller than the vertical scale height of plasmaspheric component. Hence, the similar assumption as in STIP model is applied to this component, a constant $b2$ is used.

According to the definition of hu, equation 4.10, we can find hu in numerical way once the model parameters are obtained from the best fit of RO profiles.

$$Aexp(-hu/hs) = F_{H^+}(hu) = \frac{1}{2}F(hu) \tag{4.10}$$

4.3 Validation of the Models

4.3.1 Data set, Metric for validation

The COSMIC RO observations of 18 days in November and December in 2008 were collected as the sample data for the validation of models. The shape function of ROs $F_{RO}(h)$ are obtained using SM aided by IGS GIMs, which was described in chapter 2 in detail. Besides, the CINDI measurements of the same days were gathered to get the transition height, hu_{CINDI}, as the reference.

For simplicity, fixed values of $\{h_{tc},\ h_{bc}\}$ for the whole ROs data set are used. The set of values $\{h_{tc},\ h_{bc}\}$ is chosen based on the one providing the greatest success in terms of very good fits. The criteria for selecting very good fits, referred hereafter as good-fit conditions, are the following:

(a) The interval of altitudes in the topside ionosphere used for fitting is more than two times of the scale height hs, i.e., $((h_{LEO} - h_{tc}) - (hmF2 + h_{bc})) > 2hs$. This condition guarantees that there are enough data for tracking the ionospheric changes.

(b) The global relative error, dr, is small, i.e., $dr < 0.1$.

$$dr = \frac{\sum |y_{orig}/y_{fit} - 1|}{n_{fit}} \tag{4.11}$$

Here, y_{orig} and y_{fit} represent the original value and best fitting value, and n_{fit} is the number of the data set used for fitting. Thus, dr is an index showing the quality of the fitting.

(c) The fractional contribution of the ionosphere to TEC, $IONf$, which is computed with equation 4.5, is in the range of [0, 1]. It ensures the physical meaning of $IONf$.

According to the above criteria, we set the reference value pair of $\{h_{tc},\ h_{bc}\}$ as {50, 50} km for the sample data sets. However, we should mention here that the difference in the numbers of very good fits using different cutting range sets is quite small.

Based on the data set and cutting range which are defined above, we will validate the models in the following ways.

- Check the distribution of global relative error dr of fitting results with respect to RO profiles.

- Check the impact of plasmaspheric developing process on the model parameters, such as hs, hu and $IONf$, by comparing the results obtained with CPDH model, equation 4.6, with the ones from STIP model.
- Check the variation of derived hu and hs using different cutting criteria to select upper part of RO profiles for fitting. The values obtained with the cutting range 50 km, 50 km are set as the reference.
- Compare the values of hu which are obtained from RO profiles using models with the direct measurements from CINDI. In this comparison, hu_{CINDI} is set as the reference.

Among the above four checks, the first one will be done based on all fitting results, while the following three are based on the very good fits which are selected with the above good-fits conditions (a) – (c).

4.3.2 Cumulative distribution function of dr

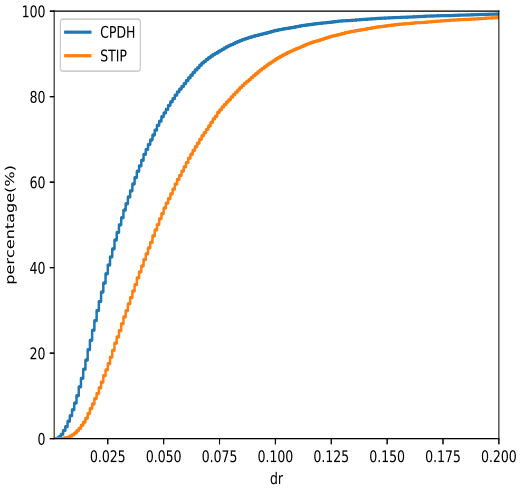

Figure 4.2: The cumulative distributions function (CDF) of dr from the fitting using two models.
Orange line – STIP model, blue line – CPDH model.

Figure 4.2 shows the cumulative distributions function (CDF) of global relative error dr. The number of sample RO retrievals is $2.64 \cdot 10^4$, almost all ROs meet the good-fits conditions (a), which guarantees enough data for fitting. Blue line is the result of CPDH model, and orange line represents

STIP model model. STIP model has good performance, i.e., around 90% fits have $dr < 0.1$, i.e., 90% fits meet good-fits conditions (b). And The performance of CPDH model is even better, more than 95% fitting results meet this condition.

4.3.3 Impact of Plasmaspheric Developing Process

In this section, the impact of plasmaspheric developing process is checked by comparing the fitting results from STIP model and CPDH model based on the same data set.

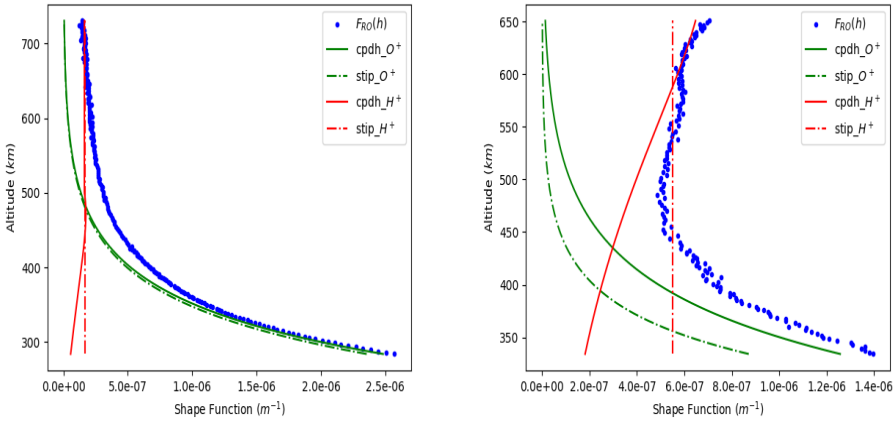

Figure 4.3: Examples of the fitting result using STIP model – dash lines and CPDH model – solid line. The blue dots are the upper part of RO shape function used for fitting. Green lines are the estimated O^+ contribution, and red lines represent H^+ contribution.

Figure 4.3 shows two fitting examples with two models, STIP model and CPDH model. The blue dots are the upper part of RO shape function used for fitting. Green lines are the estimated O^+ contribution, and red lines represent H^+ contribution. The dash lines are the result of STIP model, and the solid lines represent CPDH model. The left plot shows the case that the plasmasphere is already well developed at the altitude of $hmF2+h_{bc}$, the bottom limit of the data set. In this case, the results from these two models are similar. While the right plot shows the case which the plasmasphere is still under developing till the LEO height. Hence, we could find the difference of the estimations of O^+ and H^+ contributions using these two models.

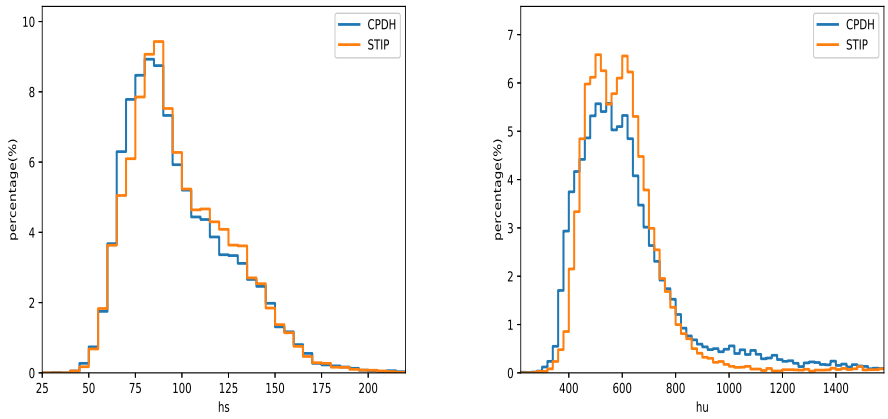

(a) hs (b) hu

Figure 4.4: Histograms of model parameters hs and hu. Orange line – STIP model, blue line – CPDH model.

The comparison of parameters hs, hu and the quantity $IONf$, based on all the sample data, are obtained by fitting ROs with the two models: CPDH model and STIP model. Figure 4.4 shows the comparison of hs and hu respectively. The blue line represents the result from CPDH model, while the orange line is the one from STIP model.

Figure 4.4a shows the distribution of the scale height hs. Generally, hs obtained from these two methods are overlapped with each other. Comparing to hs, the histograms of transition heights hu show more difference, Figure 4.4b. The hu derived from CPDH model are slightly more spread than the ones using STIP model. And the difference in the small/big values of hu are more obvious. In fact, the calculation of hu needs the more accurate estimation of the ionospheric and plasmaspheric portions along the altitude. The errors in estimating ionospheric/plasmaspheric portion will be multiplied when we compute hu. Thus, the simplification of plasmaspheric developing process has more impact on hu. Even though, the distributions of hu from these two models are still similar. They have the same peak values, around 600 km for ROs in November and December, 2008. Thus, the errors introduced by the simplification in STIP model are acceptable.

Besides, the quantity $IONf$, ionospheric contribution to GPS TEC, calculated using these two models, is studied, shown in Figure 4.5. There is no difference in distributions of $IONf$ using the model whether considering the plasmaspheric developing process or not. Since in most cases, the ionospheric portions are the dominant contribution to the topside ionosphere till

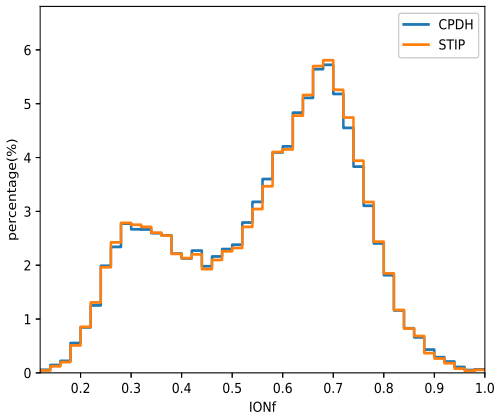

Figure 4.5: Histograms of $IONf$. The result from STIP model is represented as orange line, and the one from CPDH model is blue line.

LEO height. Thus, the developing process of plasmasphere is negligible in computing $IONf$.

4.3.4 Impact of the cutting ranges on STIP model

The impact of different $\{h_{tc}, h_{bc}\}$ value sets on the fitting results is also studied. The values of hs and hu are obtained by changing the $\{h_{tc}, h_{bc}\}$ set, i.e., the data set which used for fitting is different. The relative difference ΔP between the derived value and reference, which the $\{h_{tc}, h_{bc}\}$ is set as $\{50, 50\}$ km, is an index to show the impact. The definition of ΔP is:

$$\Delta P = 100 * |\frac{P - P_{ref}}{P_{ref}}| \tag{4.12}$$

Figure 4.6 shows the CDF of Δhs, left plot, and Δhu, right one. By comparing these two figures, one could find that the cutting ranges have more impact on hs, i.e., the different value set of $\{h_{tc}, h_{bc}\}$ will cause a larger Δhs than Δhu generally. Especially the h_{bc}, the distance from $hmF2$, has a great impact on the derived value of hs. Since the scale height hs reflects the ionospheric decaying speed. The smaller hs, the faster decay of ionospheric portion along the altitude, and the variation of ionospheric portion is more dramatic when it is close to F2 layer peak. However, for the transition height hu, this impact is reduced. In general, more than 90% fitting parameter hs are within the 20% variation range for the case $\{50, 100\}$ km, while for the rest of analysed cases, the variation range is only 10%. For hu, the variation margin is within 10% for more than 90% fitting results in all the cases.

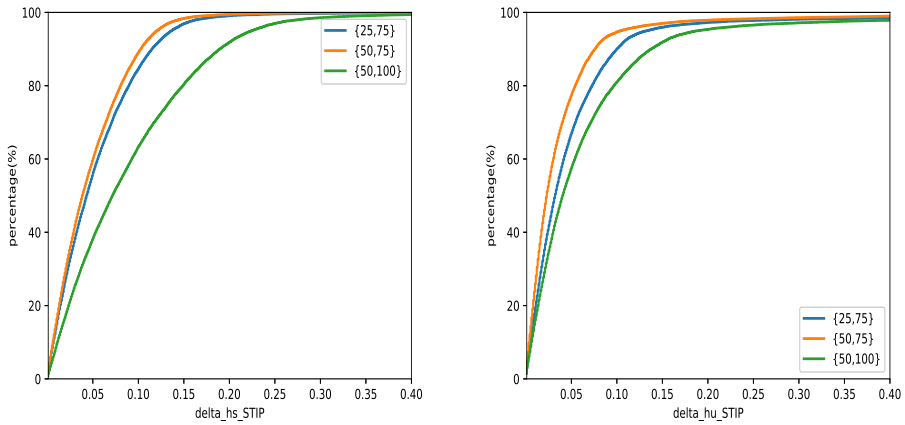

(a) Δhs (b) Δhu

Figure 4.6: Impact on the fitting parameters by using the different value sets of $\{h_{tc}, h_{bc}\}$.

4.3.5 Compare derived hu to CINDI measurements

In this section, we use the direct measurements from CINDI project as the reference. The fractional composition of O^+, H^+ and He^+ in the total electron density are provided in CINDI measurements. Hence, the transition height could be derived directly through the definition: $n(O^+) = n(H^+) + n(He^+)$. However, all the measurements are constrained in equator area due the satellite orbit, within $\pm 13^o$ geographic latitude, dip in $[-50^o, 50^o]$. In this thesis, the magnetic dip is calculated using International Geomagnetic Reference Field (IGRF) model, 12th generation [42]. The similar comparison was carried out in [49], where the single-component model, α-Chapman function, is used to derive transition height hu from RO profiles.

Figure 4.7a shows the distribution of CINDI measurements. The x-axis is LT, and the y-axis represents magnetic dip. The colour of points represent the value of hu_{CINDI}. The CINDI's sample rate is 1 Hz, i.e., there is one measurement per second. Thanks to this high sample rate, we may have many different hu values within several seconds. However, only one hu_{RO} is obtained within several minutes. Hence, we group the CINDI measurements in epochs, and use the mean value in the epoch to represent the hu_{CINDI} in the epoch, while the mean location of all measurements in an epoch is used as the location for hu_{CINDI}. Here, the one epoch is defined as a group of continuous hu measurements in time. The definition of continuous measurements is set as two adjacent measurements are within 10 seconds gap.

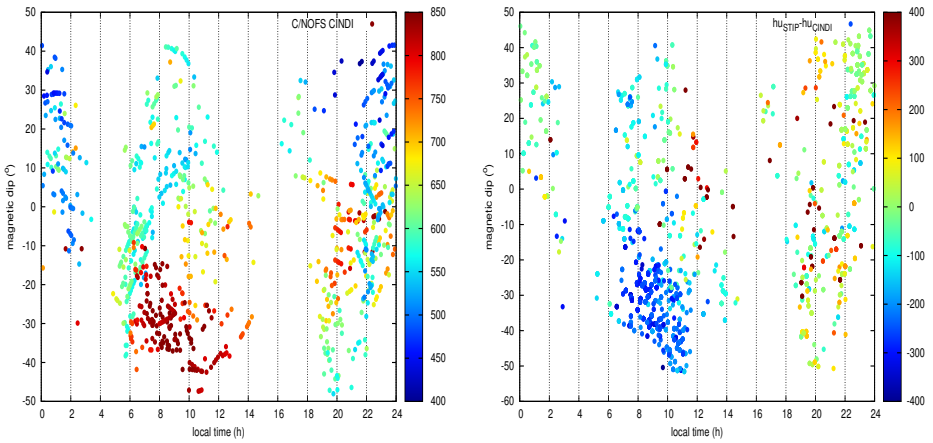

(a) hu_{CINDI} (b) Δhu

Figure 4.7b shows the distribution of Δhu, the difference between hu_{STIP}, which is derived from RO profile by STIP model, and hu_{CINDI}. For ROs, we use the F2-layer peak's time and location of one RO to represent the RO. The ones within dip range $\pm 5^o$ and time range ± 0.5 h with respect to CINDI measurements, shown in Figure 4.7a, are selected. From this plot, one can find that except the ones in the dip range $[-60^o, -20^o]$ and LT range [6 h, 12 h], where CINDI measurements are mostly greater than 800 km, the absolute difference between these two values is generally less than 200 km.

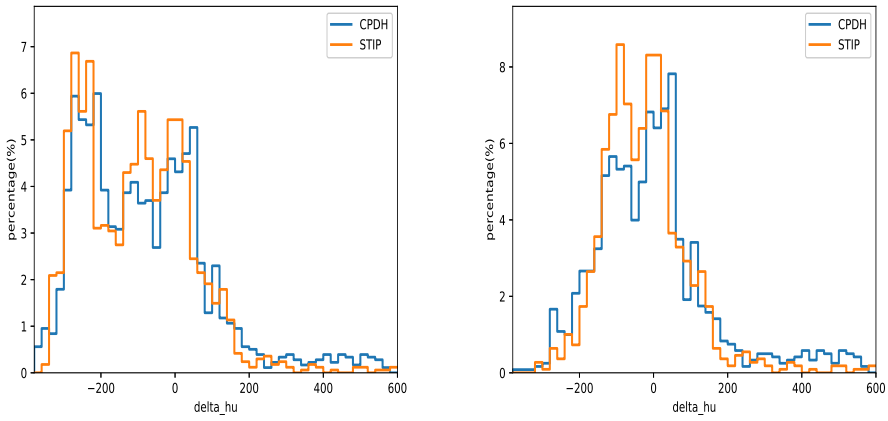

(a) whole data set (b) $hu_{CINDI} < 800$ km

Figure 4.8: Histogram of $\Delta hu = hu_{RO} - hu_{CINDI}$.
The difference between derived hu using STIP model (orange line), CPDH model (blue line) and CINDI measurements.

In order to check more detail about the difference between hu derived from CINDI measurements and the one obtained from RO profiles, the histograms of Δhu from the two fitting models are computed and shown in Figure 4.8a. The orange line represents Δhu between the value derived from RO profile using STIP model and CINDI measurements, i.e., $hu_{STIP} - hu_{CINDI}$. It shows the same quantity as in Figure 4.7b, but in different way. One can find there are two peaks in the Δhu distribution, one is located around zero, while another one is at -250 km. Blue line is the Δhu between derived hu based on ROs using CPDH model and CINDI measurements. Comparing to the hu_{STIP}, hu_{CPDH} is slightly closer to the hu_{CINDI}. In general, nearly 70% of model derived hu yields the difference within 200 km with respect to hu_{CINDI}.

Figure 4.8b shows the comparison result for the case of hu_{CINDI} smaller than 800 km. The CINDI measurements are treated as the reference for the data selection. Most of values, $hu_{RO} - hu_{CINDI}$, are located within 200 km difference margin, for both models, STIP model and CPDH model. In [49], the RO derived hu, using α-Chapman function, is about 100 km smaller than the hu_{CINDI} in general.

It is worthy to point out that, different from the *in situ* measurement, the hu derived from RO is not a value in one specific point at fix time, it is an average value during the whole RO process in a related area. However, in order to identify the hu derived from RO in spatial and time dimension, in this work, the location and time of $F2$ layer peak for one RO is used.

Figure 4.9 shows a case of the RO in high latitude, close to magnetic polar region. The magenta stars represent GPS and LEO satellite, respectively. The blue curve illustrates the plasmasphere. The red line is the ray path of radio signal from GPS to LEO, and the magenta cross is the locus of $F2$ layer peak, which is the horizontal location of RO derived hu. In theory, there is no plasmasphere in magnetic polar region due to the doughnut shape of the plasmasphere. However, in RO technique, as shown in plot, there is some path of the radio ray crossing the plasmasphere for $F2$ layer peak located around magnetic polar region. Hence, we still could derive hu from these RO measurements. On the other hand, the ray path is along the edge of the plasmasphere in this case. Thus, the plasmaspheric contribution to the GPS TEC is low. As a result, we could get high hu value in polar region, which will be shown in the following part of this chapter.

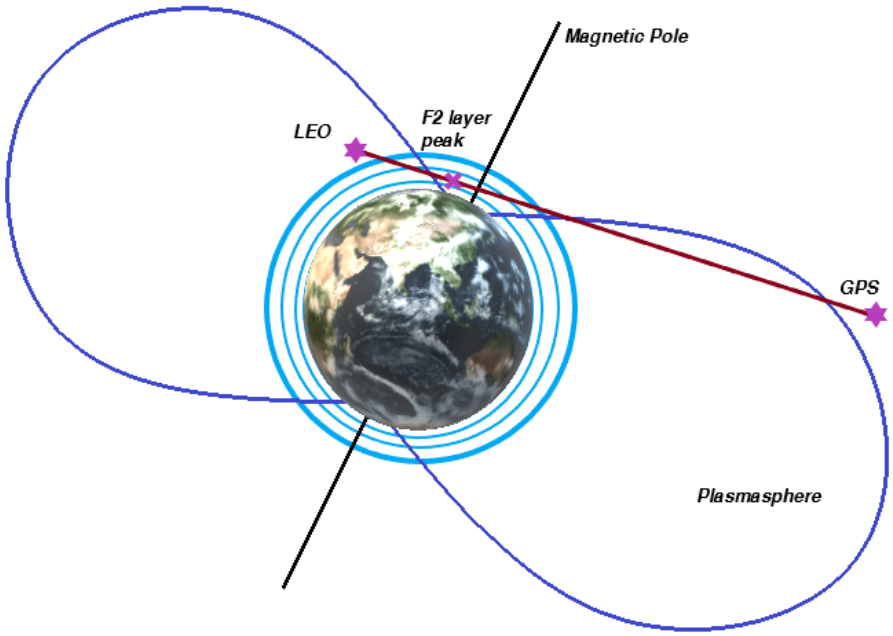

Figure 4.9: Geometry of the radio ray from GPS to LEO passing through the plasmasphere in high latitude

4.4 Discussion: conditions of applying STIP

The basic idea of STIP model is separating the ionospheric and plasmaspheric contribution in topside ionosphere. It reflects the state of topside ionosphere at the altitudes of the empirical data set used for fitting, the upper part of RO profiles.

When B is around 0, it implies that there is only ionospheric contribution below the maximum altitude of data set which is a few tens of kilometers below LEO satellite orbits. It also implies that the transition height hu is much higher than the LEO satellite orbits, hence there is no plasmaspheric contribution in the data set. In this case, it simply reduced to single component model, such as Chapman model [49]. Under this condition, the derived hs is reasonable if there is plenty data to check the variation of the ionospheric contribution. Moreover, the quantity $ION f$, which depends on the estimation of ionospheric contribution, is also reliable. However, in order to get transition height hu, the reasonable estimations of both components are needed. Even the methodology used in single component model to derive

transition height that hu is at the altitude where O^+ density is half of the ion density, it is inapplicable in this situation. Since there is only ionospheric contribution in empirical data, i.e., O^+ is always more than half in the data set. Hence, we cannot make the reasonable estimation of hu if the empirical data is lack of the plasmaspheric contribution.

When $B > 0$, there are both ionospheric and plasmaspheric contributions in the empirical data set. For derived hs and $IONf$, it is the same as the case when $B = 0$, i.e., they are reliable if there is enough data for fitting. However, unlike the case when $B = 0$, hu can be obtained from the model in this case. But, we should be cautious to the hu estimations. When the derived hu is far above the LEO satellite orbits, the estimation is questionable. According to [44], the altitude of saturated H^+ is slightly above the transition height, hu. In the other words, below hu, plasmasphere is still under developing. If hu is smaller than the maximum altitude in the data set, it means that there are saturated H^+ information in the empirical data. In this situation, we can get proper plasmaspheric information and hu from the data set. In STIP model, we simplify the plasmaspheric developing progress and use a constant to represent plasmaspheric contribution along the altitude, i.e., we assume that the plasmasphere is saturated since the lowest altitude in data set. Based on the comparison of fitting results using the STIP model and CPDH model, one can find the error introduced by this simplification of STIP model is minor. While, if hu is much higher than LEO height, 800 km, the plasmaspheric contribution among the empirical data is still under developing. Hence, the derived constant plasmaspheric contribution B only reflects the status of plasmasphere in the empirical data set. It cannot represent the final state of the plasmasphere due to the lack of information. Thus, the hu which depends on B is also not correct.

To sum up, if there is saturated plasmaspheric information in empirical data set, the error caused by the simplification of STIP model is small. While if there is no/lack of plasmaspheric information in data, no matter how sophisticated two-components model is used for fitting, we cannot get accurate plasmaspheric contribution. Since the empirical model reflects the characteristics of the data set. Thus, in the following climatological study, we will use STIP model to fit the upper-part of RO profiles.

4.5 Data set for climatological study

As well known, one key factor determining the ionosphere/plasmasphere is solar activity. Solar cycle, also named as magnetic activity cycle, is the nearly periodic 11-year change in the Sun's activity, including the variation of solar radiation levels and solar material ejections, and appearance, such

as the frequency and size of solar flares and so on. In order to check the characteristics of ionosphere/plasmasphere in solar minimum and maximum of solar cycle, the COSMIC/FORMOSAT-3 ROs data in 2007 and 2014 were gathered. 2007 is in solar minimum period in last cycle, Cycle 23, which lasted 11.6 years, beginning in May 1996 and ending in January 2008. The ROs were collected in 182 days, which are evenly distributed during the whole year. While 2014 is in solar maximum of current cycle, Cycle 24, which started in January, 2008. The ROs from the whole year 2014 were gathered for the present study.

The individual electron density profile and shape function were retrieved using SM with IGS GIMs, which was described in chapter 2, from each RO measurement. There are $3.5 \cdot 10^5$ retrievals in 2007 and $3.2 \cdot 10^5$ ones in 2014. Then STIP model, which was introduced and validated in previous sections, is used to fit the upper part of the retrieved profiles. The cutting range pair $\{h_{tc}, h_{bc}\}$ is a bit different in these two years. It is set to {50, 75} km in 2007 and to {50, 100} km in 2014. These settings agree with the physical phenomenon that larger h_{bc} is needed to avoid influence of greater F2 peak. The electronic density in F2 peak in solar maximum is generally larger than in solar minimum, also the peak in maximum is higher.

As we mentioned in the last section, hu cannot be derived from each profile with a good fitting result, although $IONf$ and hs can be obtained from each one. hu is only available when $B > 0$. Furthermore, the estimated hu, which is much greater than LEO height, is not reliable.

Year	Number($\times 10^5$)		
	good fits	$B > 0$	$B > 0, hu < 1200$
2007	2.12	2.05	2.04
2014	2.44	2.00	1.95

Table 4.1: Numbers of the fitting with different criteria

Table 4.1 shows the numbers of fitting results in the two years analyzed. Here, the data set consists in all the fits satisfying the criteria (a) – (c) in section 4.3.1. For the study of hu, we will need to separate it with different conditions. We define a subset of cases denoted $B = 0$, which includes those cases where the transition region between ionosphere and plasmasphere is much higher than LEO height, thus there is only ionospheric portion at the altitude of LEO height and below. 3.3% of good fits in 2007 are with $B = 0$, while the percentage is 18.0% in 2014. In this case, we cannot compare the hu in solar maximum and minimum directly, since we do not have the estimated values. However, we see that there are higher portions

of ROs whose transition heights are much greater than LEO satellite orbits in solar maximum than in minimum. This result agrees with the physical phenomenon that the ionosphere is more active in solar maximum, thus, there are more ROs with higher transition region.

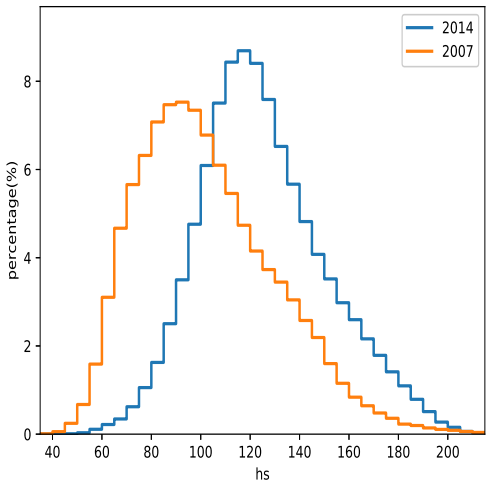

Figure 4.10: Histogram of hs. Orange line – 2007 and blue line – 2014.

Figure 4.10 shows the histogram of scale height for good fits in 2007 and 2014 respectively. The orange line represents the results in 2007 and the blue one is corresponding to 2014. The scale height hs in 2014, which is centralized around 120 km, is greater than the one in 2007, that most of the results are located around 90 km. Scale height hs is an index showing the O^+ decaying speed. From the comparison between these two years, we can find that O^+ decreases relatively slower along the altitude in solar maximum than in solar minimum.

After excluding the subset of data $B = 0$, there are similar numbers of data set in 2007 and 2014. Figure 4.11 are the histograms of hu, based on the ones with hu estimations among all the good fits, in 2007 and 2014. It shows a general picture of the hu distribution. Here, we can have a direct comparison of hu. The hu in 2007 is more centralized, and with a peak around 600 km, while the peak of hu distribution in 2014 is about 100 km greater than the one in 2007. Besides, the distribution is more spread, and there are more ROs with big value of hu. The 95% percentile value of hu in 2007 is 829 km, while it is 1108 km in 2014.

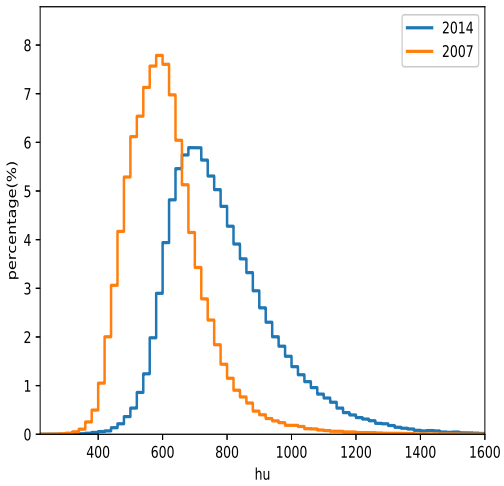

Figure 4.11: Histogram of *hu*. Orange line – 2007 and blue line – 2014.

4.6 The characteristics of the transition height *hu* and scale height *hs*

In this part of the thesis, we will have a more detailed study of *hu*, *hs* and the relationship between these two quantities. The study is based on the data in 2007 and 2014, which are described in last section. The whole year is equally divided into four seasons: March Equinox (ME) – the period around 20th, March; June Solstic (JS) – around 21st, June; September Equinox (SE) – around 22nd, September; and December Solstic (DS) – around 21st, December.

4.6.1 General picture of *hu* in solar minimum

hu in Equinoxes

Figure 4.12 is a group of plots showing the *hu* distribution in equinoxes, 2007. Figure 4.12a and 4.12c show the *hu* map along the LT (x-axis) and magnetic dip (y-axis). The colour represents mean *hu* in pixel, 1 h LT bin and 10^o dip bin. These two plots are quite similar and symmetric along the magnetic dip. Hence, we focus on the North, and divide it into several regions: near magnetic equator – $[0^o, 30^o]$, mid-dip – $[30^o, 70^o]$ and magnetic polar region – $[70^o, 90^o]$. The corresponding quantitative diurnal variations of *hu* in specific dip bins are shown in Figure 4.12b and 4.12d.

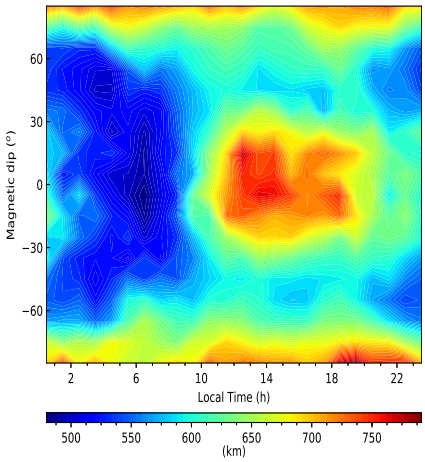

(a) March Equinox (ME)

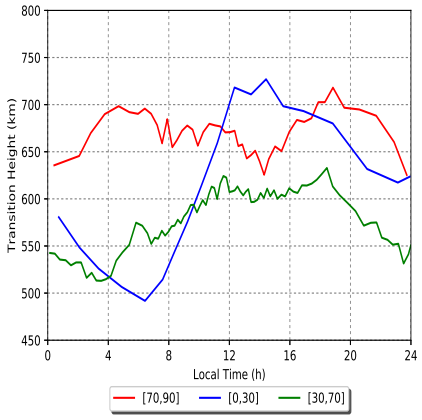

(b) North, ME

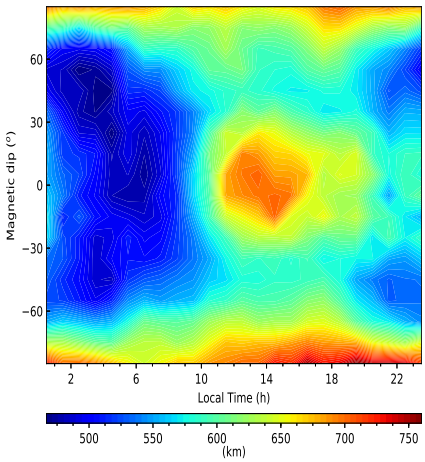

(c) September Equinox (SE)

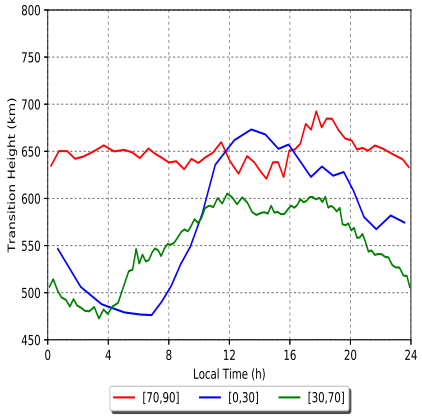

(d) North, SE

Figure 4.12: *hu* distribution in equinoxes, 2007. The plots in left are the *hu* distribution along the LT (x-axis), and magnetic dip (y-axis). The colour represents mean *hu* in pixel. The plots in right are the diurnal variation of *hu* in different dip ranges in North. Red line – polar region; green line – middle magnetic dip region; and blue line – magnetic equator.

There are clear diurnal variations of *hu* in the middle-dip and near equator regions. The transition height is characterised by a rapid collapse following the sunset, which is associated with the contraction of the plasma due to the rapidly decreasing plasma temperatures at this time. And there is an increase in *hu* at sunrise correspondingly [45]. While the *hu* values in the region close to magnetic pole stay at high level during the whole day, around or above 650 km, this is mainly due to the weak plasmasphere in this region.

Around magnetic equator, the diurnal difference of *hu* is the greatest, more than 200 km. The lowest *hu* in magnetic equator appears around 7 h, and the one in mid-dip region happens earlier, around 4 h, both are at similar levels. Since then, the *hu* increases. The increasing slope in magnetic equator is much steeper than the one in mid-dip region. And the peak values are much greater, it is above 650 km near equator and about 600 km in mid-dip region. The peak value in equator happens around noon, in LT [12 h, 16 h], meanwhile, there is some slight shrink in *hu* in polar region. After sunset, there is clear decreasing of *hu* in different regions, mainly due to the contraction of ionosphere caused by the drop of the plasma temperature. However, by comparing *hu* values at the same LT in different dip regions, one can find the one in mid-latitude is smallest during most periods of the whole day.

[34] presented incoherent scatter radar measurements of the ionosphere over Arecibo Observatory, with the dip 46.7^o, in recent extreme solar minimum of 2007-2009. It addressed that the unusually low electron densities and cold temperatures result in an extraordinarily contracted ionosphere and thermosphere. Thus, the *hu* during that period is found at extraordinary low altitudes. In October, 2009, it showed the transition altitude varies from about 450 km at night to about 800 – 820 km during the day. This result has a great agreement with our model derived *hu* in SE, 2007, the similar solar activity period, shown in Figure 4.12c.

hu in Solstices

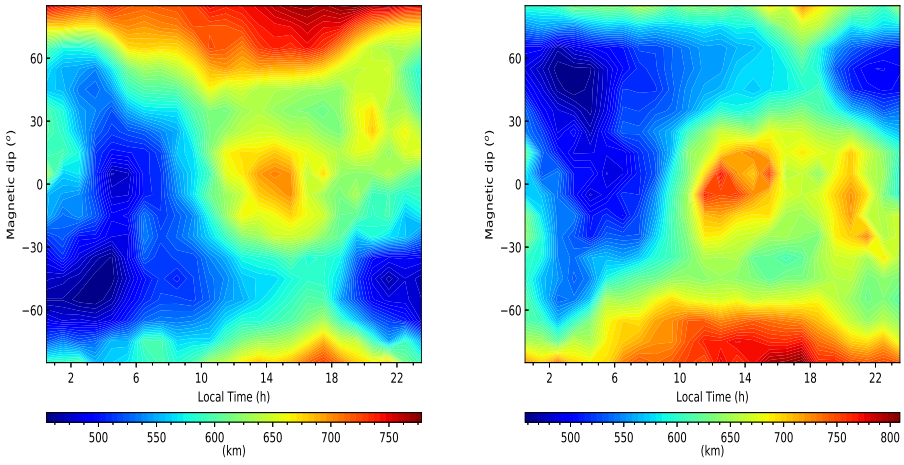

(a) June Solstic (JS) (b) December Solstic (DS)

Figure 4.13: *hu* distribution along the LT (x-axis), and magnetic dip (y-axis) in solstices, 2007. The colour represents mean *hu* in pixel.

Figure 4.13 is a group of plots showing the *hu* in solstices, 2007. Similar as Figure 4.12a and 4.12c, Figure 4.13a and 4.13b are *hu* distribution in JS and DS respectively. From these two plots, one can find the significant asymmetry in two hemispheres caused by local summer/winter difference. In general, *hu* is higher in local summer than in local winter. And the difference mainly occur in mid-dip and magnetic polar regions. Similar plots could be found in [52] Fig 4, which is based on the ROs in 2008, when has the similar solar activity like in 2007. But there are some differences between the [52] and this work.

- Inversion methodology. In [52], the classic Abel inversion was used to derived electron density profiles, which results in large errors close to equator. While, SM is used in this study. According to the discussion in chapter 3, we could find the result derived from SM is more reliable than classic Abel inversion near equator.

- Fitting model for topside ionosphere/bottomside plasmasphere. In [52], one-component model was applied to fit the topside ionosphere, i.e., only the O^+ density is modelled. In the region of geomagnetic latitude outside the range of $\pm 60^o$, there is lack of reliable fitting results in [52]. However, we use two-component models, STIP model, to get *hu*, and plenty reliable fitting results in high-dip region are obtained for the climatological study.

Besides the above two points, the y-axis in Figure 4.13 is the magnetic dip, while it is geomagnetic latitude in [52]. These two quantities are a bit different. Despite all these differences, the range for *hu* in those two works is the same, from around 450 km to 850 km. Besides, the patterns of *hu* distribution are also consistent.

Figure 4.14 shows the seasonal difference of *hu* in a more quantitative way. The ROs in both hemispheres are chosen, solid lines represent the South, and dash lines are the values in North. Red lines represent the *hu* in local summer, while the blue ones are the *hu* in local winter.

Figure 4.14a is the *hu* diurnal variation for the ROs within dip range [$\pm 30^o$, $\pm 70^o$]. The *hu* in both local summer and winter both show clear diurnal variations. The general value of *hu* in local summer is about 100 km larger than the one in local winter. The lowest values of *hu* in local summer appear 1 h earlier than in local winter, around 3 h. Besides, there is no hemispheric difference, i.e., *hu* in the same season, local summer or winter, in North and South are the same. However, for the *hu* in local winter, we can find that it stays at low altitude during the day, and it reaches maximum at 18 h. After that, there is a dramatic decrease till midnight.

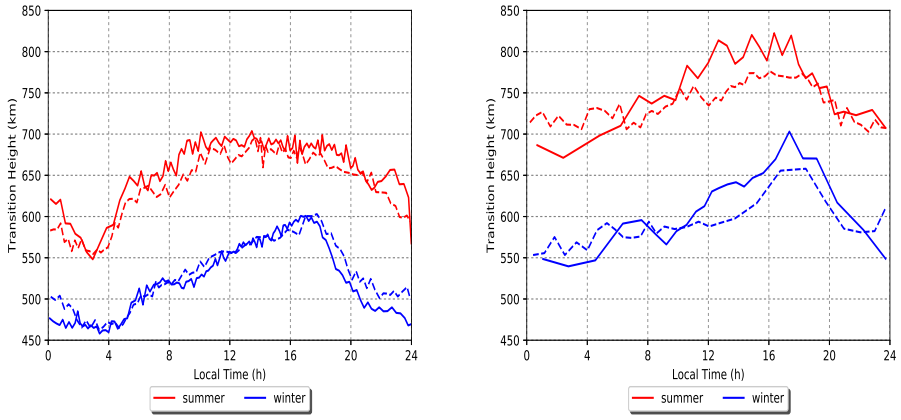

(a) In dip range [$\pm 30^o$, $\pm 70^o$] (b) In dip range [$\pm 70^o$, $\pm 90^o$]

Figure 4.14: The diurnal variation of *hu* in local winter/summer. Red lines represent local summer, blue lines are the local winter; and the solid lines represent the *hu* in South, while the dash lines are the ones in North.

Figure 4.14b corresponds to the value in magnetic polar region, above $\pm 70^o$. Similar features could be found in polar regions, but with greater *hu* in high-dip region. Both in local winter and summer, there is about 100 km difference in *hu* between the values in mid-dip and magnetic polar regions.

Furthermore, in Figure 4.13b, near magnetic equator, there is some large *hu* appearing after sunset, from LT 19 h to 22 h. This may relate with the Equatorial Spread *F* (ESF) / plasma bubble irregularities. ESF refers to the electron density irregularities in equatorial ionosphere during post-dusk which is mainly produced by ionospheric interchange instabilities. First signatures of these irregularities was shown as the spread of range and frequency in *F* region of ionosphere [35]. In [41], three varieties of irregularities, bottom-type, bottomside, and topside spread *F* were studied in details using the JULIA (Jicamarca Unattended Long-term Investigations of the Ionosphere and Atmosphere) system. Bottom-type events occurs in relatively weak and narrow scattering layers (less than about 50 km thick) in the lower F region. Topside plumes, perhaps the most impressive one, are well developed vertically, which could reach topside ionospheric heights. During moderate or high solar flux condition, it could reach over 1000 km. Furthermore, topside plume are believed to be a manifestation of the so-called plasma bubbles commonly observed by satellites and airglow measurements[46]. Bottomside spread F events correspond to broad (about 50 – 100 km wide), more structured, and stronger scattering layers around and below the F region peak.

[37] showed that the height of the post-sunset F layer is the most important parameter controlling the generation of ESF. This height is determined largely by the equatorial vertical plasma drift velocity, which is driven by the zonal electric field. The equatorial zonal electric field affects the growth rate of the Rayleigh-Taylor instability through the gravitational and electrodynamic drift terms and by controlling the electron density gradient in the bottomside of the F layer after dusk. Here, we use two parameters to indicate the height of F layer: $hmF2$ – the height of the F2 layer peak and scale height hs – reflects the decaying speed of the ionosphere, the larger hs, the slower decay.

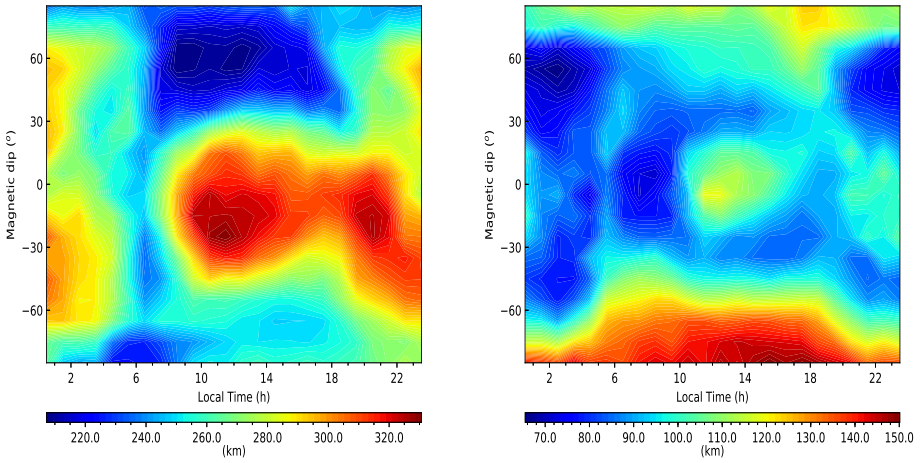

(a) $hmF2$ (b) hs

Figure 4.15: Two parameters $hmF2$ and hs, which represent the F layer height, during DS of 2007.

Figure 4.15a and 4.15b are the distribution of $hmF2$ and hs in DS, 2007, respectively. They are based on the same data set for Figure 4.13b. During the post-dusk, from LT 19 h to 22 h, near magnetic equator, we could find the higher $F2$ layer peak, $hmF2$ with relatively large scale height, hs. Hence, during this period, near magnetic equator, the height of the F layer is quite large, which suggests the existence of ESF.

4.6.2 General picture of hu in solar maximum

Through the plots above, we can conclude that there are diurnal, magnetic latitudinal and seasonal effects on hu in solar minimum. In this section, the characteristics of hu in solar maximum will be studied based on same separations, and the yearly effects on hu will be checked by comparing the results in these two years.

Lack of derived *hu* near magnetic equator

Unlike in solar minimum that there is *hu* value in each pixel, 1 h LT and 10^o magnetic dip bin, in different seasons, there are many pixels lack of *hu* values in 2014, mainly occurring from noon till night, in magnetic equator region. Hence the general picture of *hu*, like Figure 4.12a could not be obtained in almost all periods of the year in 2014, except JS.

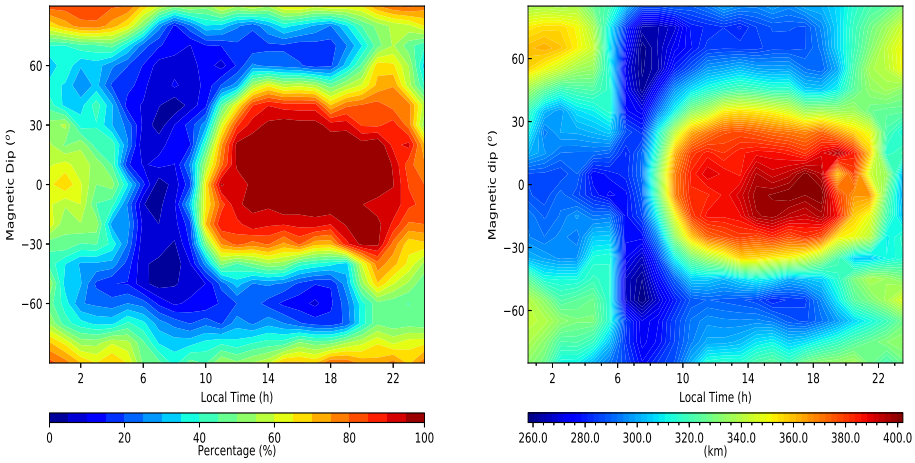

(a) invalid points ratio (b) $hmF2$ distribution

Figure 4.16: The invalid points ratio and $hmF2$ distribution in ME, 2014.

In order to check the cause of sparsity of *hu*, and density distribution of the derived *hu*, the invalid points ratio in each pixel are obtained and shown in Figure 4.16a as an example. The invalid points are the ROs which could be retrieved, but the *hu* value could not be obtained by fitting RO profiles with STIP model. And the invalid points ratio is the ratio between invalid points and number of RO profiles. Figure 4.16a is based on the data in ME, 2014. From this plot, we could find that there is a large patch close to equator – dip within $\pm 30^o$, from noon till midnight, with 100% invalid points ratio, i.e., there is no derived *hu* value in this area. Figure 4.16b is the distribution of $hmF2$, the F2 layer peak altitude, based on the same data set. Comparing these two plots, one could find that they have similar pattern, i.e., the invalid points ratio is highly related to the $hmF2$ value. The ratio becomes greater as the $hmF2$ increasing. When the $hmF2$ is greater, it means that the ionosphere is more active, and could extend to higher altitude. While the RO data only contains the topside ionospheric information up to LEO height, it may not contain the plasmaspheric information till that altitude when the ionosphere is active. Hence, the *hu* could not be derived from RO profiles. In this way, high invalid points ratio could link to the higher transition height. Return to this example, Figure 4.16a, in equator area from

noon till midnight, the invalid point ratio is above 90%, we could conclude higher transition height in this area comparing to the surrounding area, even without derived *hu* values. This also agrees with the features shown in Figure 4.12a, based on the data in ME, 2007.

hu in local winter/summer

Different from the magnetic equator region, there are plenty *hu* values in mid-dip and polar region in 2014. Figure 4.17 are *hu* diurnal variations in local summer/winter in both hemispheres, 2014. The left one is the diurnal variation of *hu* in mid-dip region, dip within [$\pm 30^o$, $\pm 70^o$], and the right one is magnetic polar region, above $\pm 70^o$. The red lines represent the *hu* in local summer, and blue lines correspond to local winter. The solid lines are the South, while the dash lines are North.

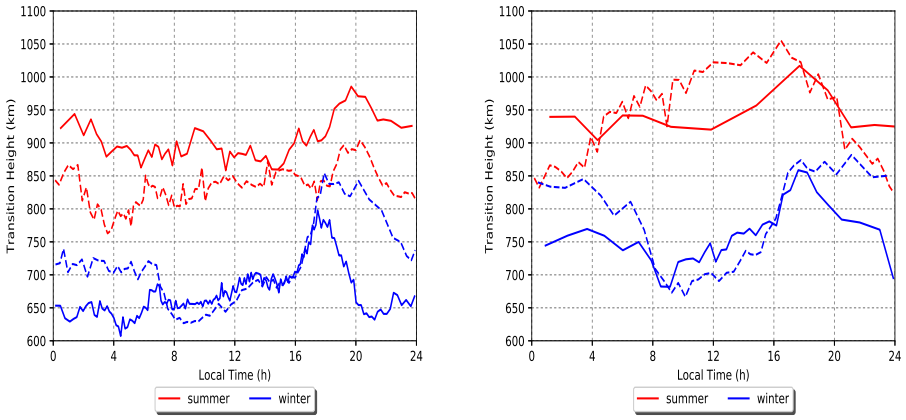

(a) In dip range [$\pm 30^o$, $\pm 70^o$] (b) In dip range [$\pm 70^o$, $\pm 90^o$]

Figure 4.17: *hu* diurnal variations in local winter/summer, 2014. Red lines – local summer, blue lines – local winter; and the solid lines – South, the dash lines – North.

In solar maximum, the mean values of *hu* vary from 600 km to 1100 km in mid-dip and magnetic polar region, much higher than the range in solar minimum. The same as in solar minimum, the *hu* values in local summer, red lines, are generally higher than the ones in local winter, blue lines. However, there are many different features comparing to the ones in 2007.

In both Figure 4.17a and 4.17b, there is no evident climbing stage after sunrise for *hu* like in 2007 for both local summer and winter. On the contrast, it happens in the afternoon. As a result, the peak value of *hu* mainly occur

after sunset in both summer/winter. In mid-dip region, it still happens around 18 h in local winter, the same hour as in solar minimum. While in local summer, it occurs around 20 h. And in polar region, it appears about 18 h in both summer and winter.

The hu during the day, from 8 to 14 h, stays at low level for both winter/-summer in solar maximum. Especially, in the local winter, the blue lines, there is a valley during that period in both plots, i.e., the daytime hu is smaller than at night. A similar phenomenon was found in [52].

In mid-dip region, the solid blue line, local winter in South, has a clear second collapse during the 3 – 4 h, while the first one happens after 18 h. [45] pointed out that it is related with the midnight abatement/reversal of the neutral air wind over low to mid latitudes which is associated with the midnight temperature maximum. When the wind begins to abate or reverse, the height of the F region is lowered, the recombination rate increases, and the O^+ density decreases.

There is obvious hemispheric difference in 2014. While, the diurnal variation of hu in both hemispheres during the same season are overlapped in 2007. In North, shown as the dash lines, there are some epochs of the day, the hu in winter and summer are at the same level. In mid-dip region, around 18 h, the blue and red lines are at the same level, around 850 km.

4.6.3 Linear regression between hu and hs

As shown in [44], transition height and scale height are highly correlated, with a correlation coefficient exceeding 0.8 at mid-latitudes. In STIP model, hu and hs are linked. In fact, hu is derived from hs with some factor, $ln(A/B)$. But this factor, $ln(A/B)$, could vary with the RO. Hence, we will check if the factor is similar for all or some group of ROs selected by some conditions, for instance, magnetic dip, LT, season and period of solar cycle.

Figure 4.18 is one example showing the relationship between hu and hs. Blue dots are the individual hu/hs ratio, gathered from magnetic dip range [50^o, 60^o] in North, during daytime within LT range [10 h, 16 h] in JS, 2014. Red line is the linear regression based on all the individual ratio, with a correlation coefficient $r = 0.75$. And the green line is the best fit of the linear relationship between hu and hs which starts from origin. Comparing these two linear regression, the green one worsens the fit a bit, but it only needs one quantity, the hu/hs ratio – Rt, to model the relationship between hu and hs.

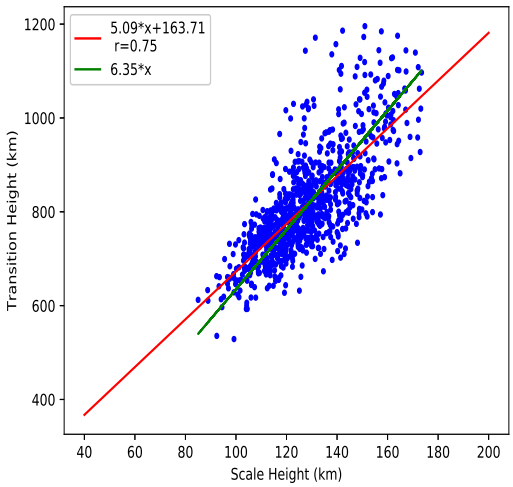

Figure 4.18: hu vs hs.
Blue dots: individual profiles; red line: linear regression $y = ax + b$ with two variables a and b; green line: linear regression which starts from origin.

The general features about the transition height, hu, in solar minimum and maximum were studied in the last two sections. In this section, we will focus on the relationship between transition height, hu, and scale height, hs. As it is shown in section 4.6.3, the relationship between these two parameters could be modelled by a linear regression starting from origin, with high correlation coefficient. Here, we will use the ratio $Rt = hu/hs$ to represent the relationship between hu and hs.

Figure 4.19 is a set of plots showing the hu, hs and Rt variation along the magnetic dip in different seasons of 2007. The top panel is the variation of hu, the middle panel is the one for hs, and the bottom one represent the Rt variation. The plots on the left column are based on the data during night-time, LT within [20 h, 2 h], and the right column shows the parameters during day-time, LT in [10 h, 16 h]. The different colour of lines means the data set collected in different periods of year: the red line is the data in ME, blue one is DS, green one is SE and cyan one is JS.

Figure 4.19a and 4.19c show the hu variation along magnetic dip, which is the mean hu of each 150 continuous values. There is a valley within [$\pm 30^o$, $\pm 60^o$] in all the cases during both night and day, although the location varies in different seasons. The greatest hu appears close to magnetic poles. The difference of hu values caused by the magnetic dip is sometimes bigger than the daily difference. For example, for the red line corresponding to

the data in JS, the difference between maximum, around North pole, and minimum, within $[-60^o, -40^o]$, is almost 350 km. Since it is the combination of seasonal and magnetic latitudinal effects. While comparing the hu during night-time and day-time at the same magnetic dip region, the difference is within 100 km. Figure 4.19c and 4.19d are the corresponding hs. Generally, hs has the similar variation shape along the magnetic dip as hu. It varies within range [70 km, 150 km], while hu varies from 450 km to 800 km.

Figure 4.19e and 4.19f are the variations of Rt. The Rt is obtained by linear regression which starts from origin based on the data with 10^o dip bin. The variations of Rt are constrained to the range [5, 8] for both night and day. The shape of the Rt variation is opposite to the one of hu or hs. There are greater values of Rt in the mid-dip and near magnetic equator regions, while the smallest values occur at magnetic poles.

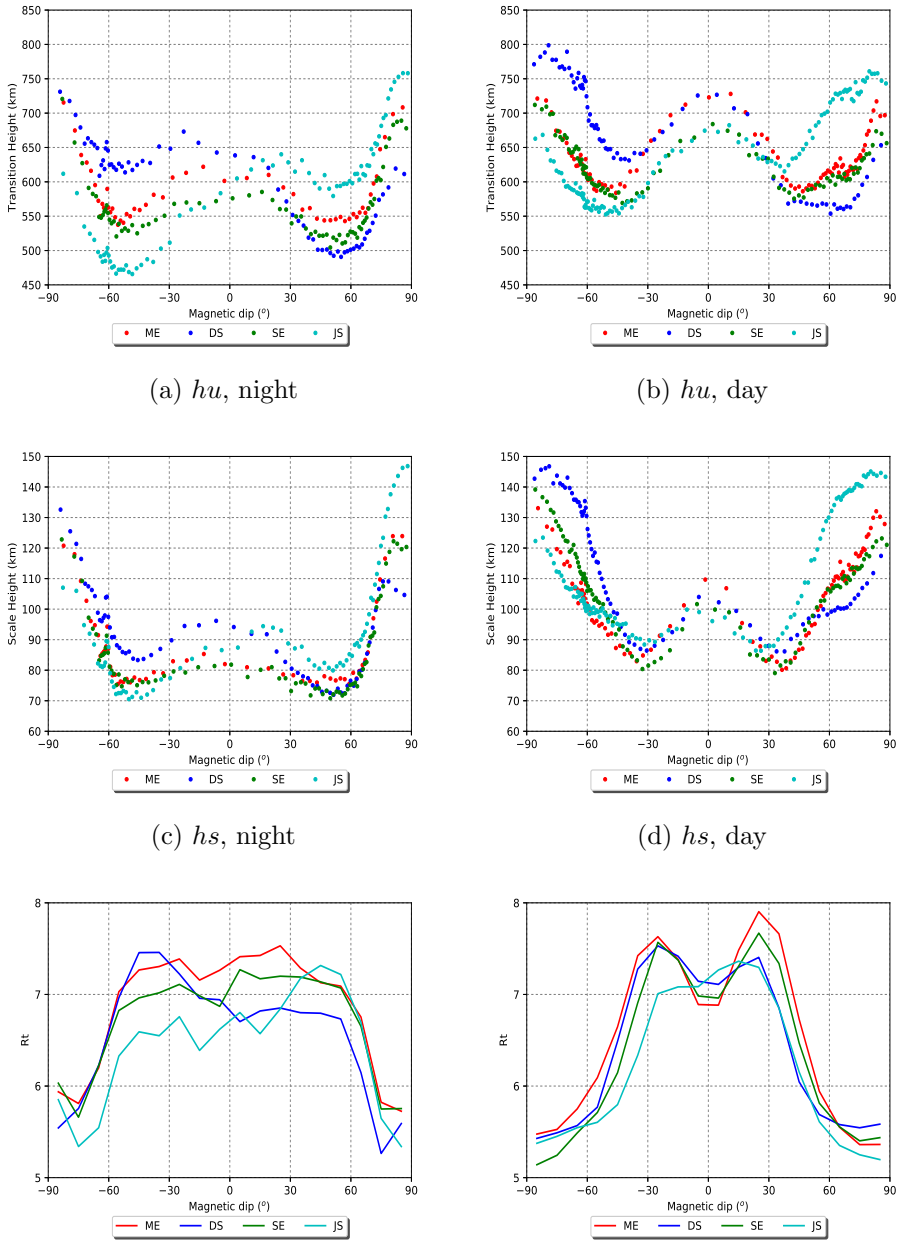

(a) *hu*, night

(b) *hu*, day

(c) *hs*, night

(d) *hs*, day

(e) *Rt*, night

(f) *Rt*, day

Figure 4.19: Variation of *hu* – top, *hs* – middle and *Rt* – bottom along magnetic dip in different seasons, 2007. The night epoch is the LT within [20 h, 2 h], and the day epoch with LT in [10 h, 16 h]. The red dot/line correspond to the data in ME, blue one is DS, green one is SE and cyan one is JS

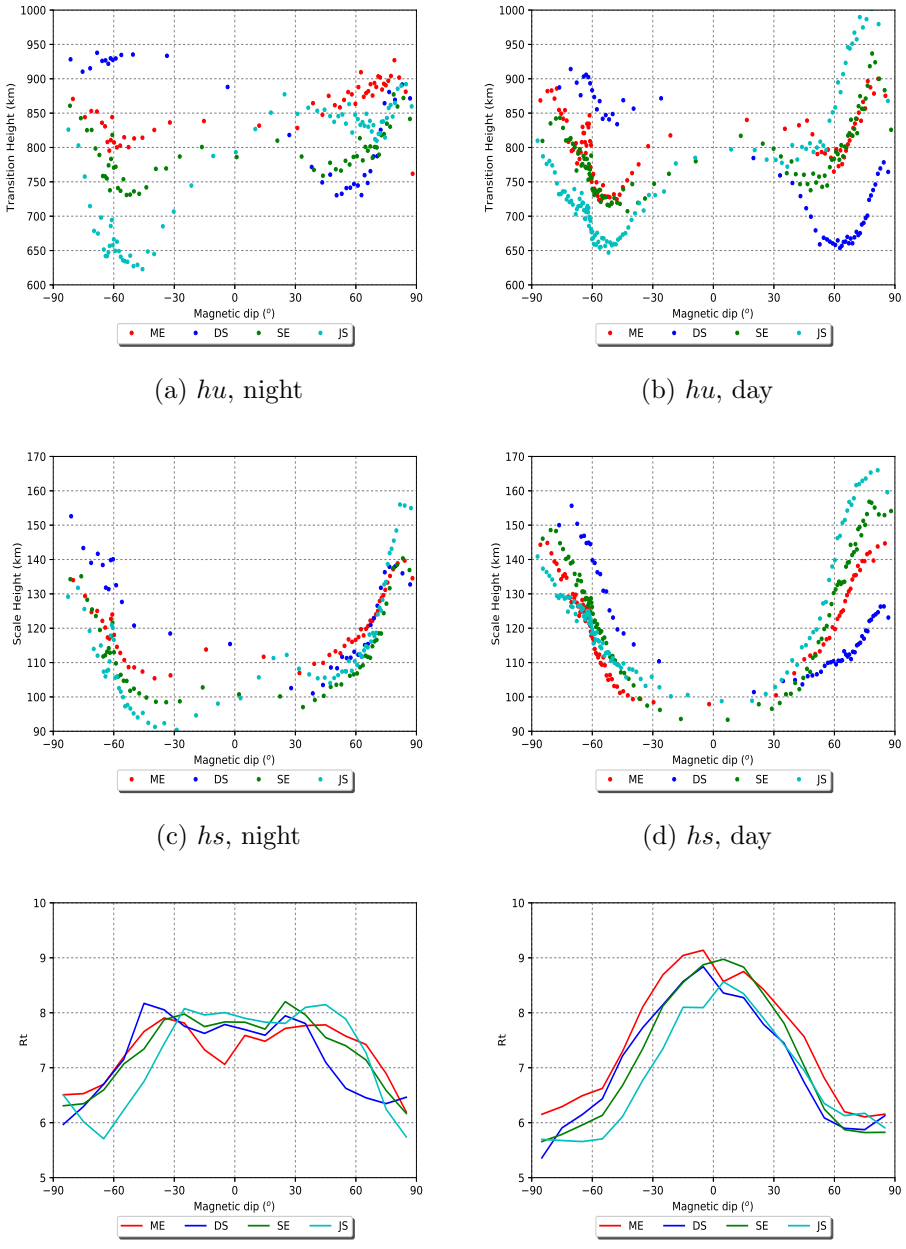

(a) *hu*, night

(b) *hu*, day

(c) *hs*, night

(d) *hs*, day

(e) *Rt*, night

(f) *Rt*, day

Figure 4.20: Variation of *hu*, *hs*, and *Rt* along magnetic dip in different seasons, 2014, similar as Figure 4.19.

Figure 4.20 are the similar group of plots as figure 4.19, but for 2014. For the right column, the variation of three quantities during the day in 2014 is presented. I must be pointed out that, not like in 2007, there is a lack

of hu values near equator during the day in all the seasons in 2014, as it is addressed in previous section. Hence, the lines between -30^o and 30^o cannot show so much details about hu in this region. It is same applied to hs and Rt, since they are based on the same data set. Hence, we will focus on the features in mid-dip region and magnetic poles, i.e., magnetic dip above $\pm 30^o$, from these plots.

Different from the solar minimum, there is obvious hemispheric difference in solar maximum for hu and hs. During the night-time, the seasonal difference is more significant in South hemisphere. The difference in hu between local summer and winter in South could reach about 350 km, around -50^o. While the difference in North is only about 150 km, less than half of the difference observed in the South. However, during the day, the situation is just the opposite, the seasonal difference in North is larger.

The Rt in 2014 also varies in the same range, [5, 8], except the ones during the day within dip range $[-30^o, 30^o]$, which is not reliable due to the lack of data. Hence, we could find Rt is more stable than the other two parameters. It is more easy and reasonable for modelling.

4.7 Conclusion

In this chapter, the two-components models, STIP model and CPDH model, both considering the ionospheric and plasmaspheric portions, are introduced to fit the topside ionosphere. The ionospheric scale height hs, the parameter reflecting the ionosphere decaying speed along the altitude, and transition height hu, the separation between ionosphere and plasmasphere, could be derived by fitting the topside part of RO profiles with both models.

Based on the sample data in November and December, 2008, the fitting results of the two-component models are validated in different ways. The CDF of global relative error dr of fitting results with respect to RO profiles shows that the two-component models have good fitting performance, around 95% fits with $dr < 0.1$. The model parameters, hu and hs, derived from these two models, have similar distributions, i.e., the assumption of constant plasmaspheric contribution in topside ionosphere is reasonable. Furthermore, the model derived hu has a good match with the direct measurements from CINDI in the range of altitudes that we have analysed.

The conditions of applying the STIP model are also discussed. For the empirical models, there is the constraint brought by the data set. i.e., these models show the picture of topside ionosphere till some limited altitude, which is determined by the LEO height. This constraint applies to the

STIP model, since it is a kind of empirical model based on the data. However, it differs from one-component model, only considering the ionospheric contribution in topside profiles. The STIP model could reflect the two contributions in topside-ionosphere region. Besides, for the case of more active ionosphere, i.e., there is no plasmaspheric contribution in data, it is simplified as one-component model, but with the indication of the active ionosphere. The derived hs are reasonable if there are enough data for fitting. Considering the height of LEO orbits, around 850 km, it is easy to meet this condition. But for transition height, the condition is a bit more restrictive. Since it requires reasonable estimation of both ionospheric and plasmaspheric contributions. Hence, if the derived hu is far above the LEO height, the values are questionable.

The statistical and climatological study of transition height hu is carried out based on the RO measurements in 2007 and 2014, solar minimum and maximum respectively, along with other two related parameters hs and Rt. The transition height shows the clear diurnal, seasonal, solar cycle dependences. Besides, we could find the link between transition height and equatorial plasma bubbles, i.e., equatorial plasma bubbles may cause higher transition height. On the other hand, we find that hu and hs are highly correlated. The parameter Rt, hu/hs ratio, could be used to represent and model that relationship. Different from hu and hs, Rt is more stable under different situations. Hence, it is a parameter more suitable for modelling.

Chapter 5

Study of Ionospheric and Plasmaspheric contributions to GPS TEC in Different Periods of Solar Cycle

5.1 Introduction

Thanks to dual-frequencies signals transmitted by GPS satellites, the TEC along the propagation path between the satellites and receivers can be estimated from the distinctive frequency-dependent delays caused by upper ionized part of atmosphere. Since the orbit of GPS satellites is near 20,200 km, equal to 4.2 L, while the transition height usually occurs between 500 to 2000 km, the radio signal transverses through plasmasphere and ionosphere, with a large range of altitudes in the plasmasphere. Thus, the TEC obtained from ground-based GPS receivers includes both the ionospheric and plasmaspheric electron contents. Several studies have pointed out the plasmasphere contributes significantly to TEC, night-time plasmaspheric electron content could reach 60% of the TEC at low latitude [61], [74]. Hence, we cannot simply ignore plamaspheric contributions in GPS TEC.

Since 1960s, the plasmaspheric electron content distribution were mainly computed using the physical models, such as field line inner-hemispheric plasma (FLIP) model [69], or deduced from observations in limited geographic locations, such as the whistler wave data [55], [64], ionosonde's measurements [54]. The physical models usually require a lot of computational effort. Besides, most of them are very sensitive to the values of parameters [71]. While the empirical models are constrained to some specific geographic locations. Hence, based on these methodologies, it is very difficult to get a global picture of plasmasphere. However, according to the

orbit height of GPS, 4.2 L, and the outer boundary of the plasmasphere, from 4.5 to 8 L, we can get almost all the plasmaspheric electron content from GPS TEC. And thanks to the global coverage over the Earth of GPS network of ground receivers, it brings us a way to carry out the climatological analysis of ionosphere and plasmasphere globally by extracting these two contributions from GPS TEC.

[74], [9] used the JASON-1 zenithal observations to estimate the plasmaspheric electron content directly. JASON-1 is the LEO satellite equipped with dual-frequencies GPS receiver, orbiting at 1335 km. In this approach, the region from GPS satellite to JASON-1 is treated as pure plasmasphere by fixing the transition height at the LEO orbit, independent from the real situation of the boundary between these two layers. However, as we have seen in the previous chapter, the transition height varies in a large range of several hundreds of kilometres, sometimes being above JASON-1 orbit, since the plasmasphere and ionosphere are quite dynamic.

Using the quantity $IONf$, the ionospheric fractional contribution to TEC, described in the previous chapter, we could separate the ionospheric and plasmaspheric contribution from GPS TEC, without fixing the transition height. $IONf$ is an unit-less quantity, which can be computed using Equation 4.5. Once $IONf$ is calculated, with known TEC at a particular location and time, for instance, IGS GIMs, the ionospheric/plasmaspheric electron contents can be obtained directly.

In this chapter, the same data set as in previous chapter for the climatological study of transition height hu and scale height hs are used. Based on the very good fits in the two years, 2007 and 2014, the $IONf$, along with other related parameters, such as Ionospheric and Plasmaspheric electron contents, EC_{ion} and EC_{pl}, are studied. Besides, in order to check the ionospheric anomalies, the quantity $NmF2$ is also studied along with $IONf$.

5.2 Ionospheric Contribution to GPS TEC – $IONf$

5.2.1 Diurnal Variation

In this subsection, the diurnal variation of $IONf$ will be studied. Initially, the ROs are selected around magnetic equator, within magnetic dip range in $[-20^o, 20^o]$, to minimize the seasonal influence. There are 1.66×10^4 ROs in this region in 2007 and 1.44×10^4 ones in 2014.

Figure 5.1 shows the average $IONf$ variation along the LT. The red line represents 2014, while the blue one is 2007. The $IONf$ follows a similar

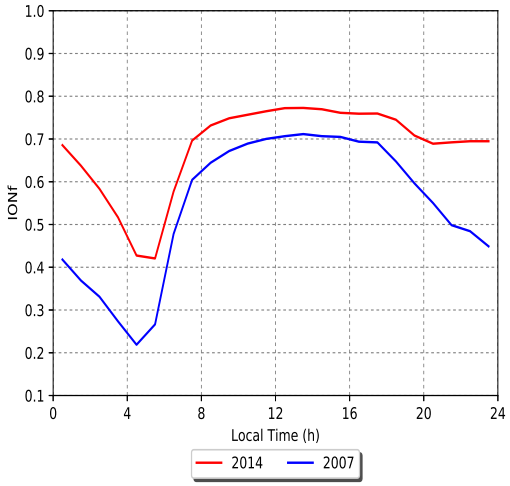

Figure 5.1: The local time variation of $IONf$ for ROs near magnetic equator. Red line – 2014, blue line – 2007.

trend in different periods of solar cycle. In both cases, the $IONf$ hits its bottom value around 5 h, when it is just before sunrise in equator. After that, it increases rapidly till it reaches its highest value around noon, i.e., it is the period when the $F2$ layer is developing. Then it keeps more or less the same level around 18 h, i.e., during this period, the $F2$ layer stays at some equilibrium state. The diurnal difference of $IONf$ is around 0.4 in 2014, and about 0.5 in 2007. When it is sunset, the $IONf$ drops. However, there are also some differences between solar minimum and maximum. $IONf$ in 2014 is larger than the one in 2007, i.e., the ionospheric contribution of TEC in solar maximum is greater than the one in solar minimum. The difference of $IONf$ in these two years is less than 0.1 during the day, while it reaches 0.3 at midnight. Moreover, one can find the different features between these two years during the period after 16 h till midnight. The $IONf$ drops rapidly in 2007, while it keeps in a high level till midnight in 2014.

As we can see in the previous figure, $IONf$ varies along LT. Here, we group the ROs into four different epochs of the day:

- Day-time. ROs are selected within LT [10, 18] h.
- Night-time, LT before 4 h or after 22 h.
- Sunrise period, LT in [4, 10] h.
- Sunset period, LT in [18, 22] h.

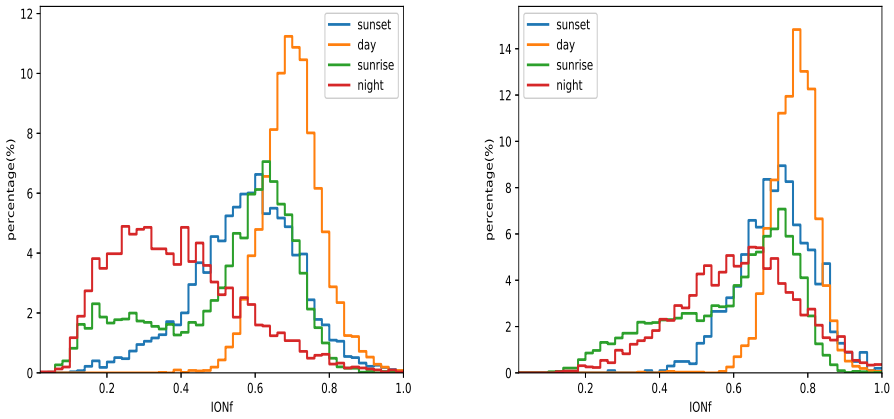

(a) 2007 (b) 2014

Figure 5.2: Histograms of $IONf$ for ROs near magnetic equator. The ROs are divided into four groups according to LT: day-time – orange line; night-time – red line; sunrise – green line and sunset – blue line.

Figures 5.2a and 5.2b are the histograms of $IONf$ distribution for the ROs near equator in different epochs of the day. The left plot is for ROs in 2007, and the right is 2014. The orange line represents the day-time ROs, the red line corresponds to the night-time ones, and the blue one is the sunset period, while the green one is the sunrise epoch. By comparing these two plots, one can find that $IONf$ in solar maximum is generally greater than in minimum.

The $IONf$ of the day-time ROs in these two years has the similar distribution, which is a close-to-Gaussian distribution. Thus, we can use the mean value μ and standard deviation σ to characterize the distribution of $IONf$ during day time. There are 6264 day-time ROs in 2007, with $\mu = 0.70$ and $\sigma = 0.08$, while 3156 ones in 2014, with $\mu = 0.76$ and $\sigma = 0.06$.

Comparing with other period, the $IONf$ distribution of night ROs in these two year shows most significant difference, i.e., the difference of $IONf$ distribution between these two years is mainly caused by the night-time ROs. $IONf$ in 2007 is clearly smaller than the one in 2014 at night. In 2007, the histograms of night-time ROs and the one during sunset shows the distinctive difference. While, in 2014, the night-time distribution can be treated as the continuation of the sunset process. In other words, in solar minimum, there is enough time for the recombination process to reach its end. Furthermore, we can find that the $IONf$ distributions show more variation during the periods of sunrise and night than in the other two

periods analyzed.

5.2.2 Ionospheric Anomalies

The classic Chapman ionization theory is a simple mathematical model for the formation of ionized layers. In theory, Ne in the ionosphere should behave in a way that is controlled by the solar zenith angle. For instance, Ne should be greater in summer than in equinox, and smallest in winter. However, many previous studies revealed there are discrepancies between the observations and predicted values. Historically, when the behaviours of the $F2$ layer were significantly deviated from predicted values based on the theory, they were called the ionospheric anomalies. In this work, different ionospheric anomalies/irregularities will be studied in the following two subsections.

The winter anomaly is one of the well-known anomalies in the $F2$ layer. It has been known since the beginning of regular ionospheric observation. It is mainly present in North at mid-latitude. It is defined as the higher total $F2$ ionization in the winter hemisphere than in the summer one. In [68], it reported that the winter maximum prevails over much of North at solar maximum, and appears to be due to an increase in the O/N^2 ratio caused by convection of the O from the summer to winter hemisphere. The winter anomaly falls off in amplitude and area with decreasing solar activity as would be expected to happen with decreasing energy input and consequent reduction in the convection activation mechanism.

Semi-annual anomaly, which produces larger $foF2$ / $NmF2$ for equinoxes than for solstices, is another well-known phenomenon in ionosphere. [76] proposed that the the semi-annual variation of $NmF2$ is linked to the upper atmosphere temperature and [68] suggested that semi-annual anomaly is related with geomagnetic and auroral activity.

The seasonal sunrise anomaly is shown as the ionospheric critical frequency $foF2$ increases faster in winter than in summer. According to the relationship between $NmF2$ and $foF2$, which was described in chapters 2 and 3 in detail, the same feature will occur for $NmF2$. In [65], it was suggested that this anomaly is related with the neutral composition changes.

In contrast to the winter anomaly, annual anomaly, also named as non-seasonal anomaly, affects the world as a whole. It is the phenomenon that the $NmF2$ in December is on average greater than the one in June in the whole world, both during sunlight and at night time periods. The early studies of annual anomaly, [75], [76], have pointed out that the non-seasonal

variation is unexpectedly large and, in particular at noon, is generally the most important component in low and equatorial latitudes and/or when solar activity is low. Its importance, however, decreases with increasing solar activity. Its amplitude has a latitudinal peak at about 15^o – 20^o geomagnetic latitude.

Besides the above anomalies related with seasons, there are several ionospheric irregularities which are observed in specific regions of the globe.

- Equatorial Ionization Anomaly (EIA), is characterized by a depression in ionization densities (or trough) at the magnetic equator and two crests on either side of the equator at about 18^o magnetic dips. It is a daytime phenomenon. [66] talked about the height structure of EIA, which extends throughout the F-region starting from 200 km with a strong altitude dependency. The depth of EIA is defined as the ratio of electron density at the crest over the one at the trough. This depth is maximum at the height around $F2$ layer peak, $hmF2$, and it decreases as the altitude goes farther from $hmF2$, both downwardly and upwardly. While the locus of EIA is moving equatorwardly as the altitude increases.

- Weddell Sea Anomaly (WSA) is a summer ionospheric anomaly, where electron densities have been observed to maximize around the Weddell Sea region (roughly 60^o magnetic dip) during the night, rather than during the day as would be expected due to diurnal photoionization [57].

- South Atlantic Magnetic Anomaly (SAMA), is a region spanning the south Atlantic and South America where the Earth's magnetic field is at its weakest. [53] addressed that SAMA plays an important role in contributing the longitudinal variations of the geomagnetic field intensity and declination angle. Enhanced ionospheric conductivity over the SAMA region could result from precipitation of energetic particles from the inner radiation belt on a spatial scale that may extend several degrees in longitude and latitude around the central region of the anomaly. [70] pointed out the occurrence of plasma density irregularities responsible for scintillations is most likely when the integrated E-region Pedersen conductivity is changing most rapidly. Hence, it is highly linked to the longitudinal occurrence patterns of equatorial scintillations and range-type spread F.

- The mid-latitude trough is a region of ionization depleted sector in F-region ionosphere. The most accepted view for the nature of the mid-latitude trough, also known as main trough, is that the electron

densities represent the ionization level to which the entire night ionosphere would fall in the absence of the external ionization sources [67]. Thus, $IONf$ is a suitable quantity to check that trough. [67], [73] expressed the mid-latitude trough is a result of the stagnation of ionospheric plasma, trapped at the dip around 60^o.

5.2.3 Seasonal, Semi-annual and Annual Variations / Hemispheric Difference

In this section we will focus on the study of the annual, semi-annual and seasonal variations of ionosphere using the results from ROs. At the same time, the hemispheric difference observed during those anomalies will also be checked. The whole year is divided into four periodsas in previous chapter, namely: March Equinox (ME), June Solstic (JS), September Equinox (SE), and December Solstic (DS).

Ionosphere in local winter/summer in both hemispheres

To study the ionosphere in local winter/summer, the ROs in mid-latitudes, within the magnetic dip ranges $[20^o, 70^o]$ and $[-70^o, -20^o]$, in two periods, JS and DS, are chosen.

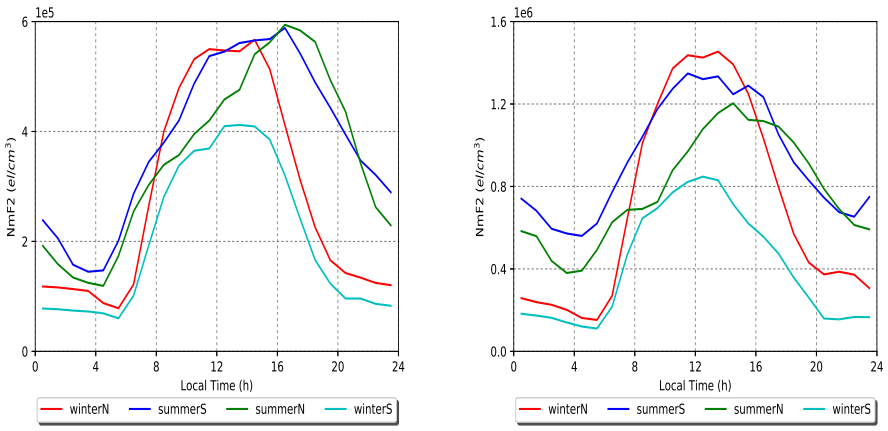

(a) 2007 (b) 2014

Figure 5.3: Diurnal variation of $NmF2$ during local winter/summer in both hemispheres. Red line – local winter in North; blue line – local summer in South; green line – local summer in North and cyan line – local winter in South.

Figure 5.3 shows the diurnal variation of the $NmF2$ in local summer/winter in both hemispheres for solar minimum, left plot, and solar maximum,

right one. We can find the following features from Figure 5.3.

- In study of the winter/summer ionosphere, one of the most popular phenomenon is the winter anomaly. As shown in Figure 5.3, during both solar minimum and maximum, around noon between [8, 16] h, the $NmF2$ in local winter in North, red line, is clearly greater than in local summer in South, blue one.
- The seasonal sunrise anomaly in Figure 5.3, the winter ones, red and cyan lines, are much steeper than the summer ones, blue and green lines, during the sunrise sector.
- The hemispheric difference is much greater in local winter than in local summer. The $NmF2$ diurnal variations in local summer, in both South and North, blue and green lines respectively, are quite similar in the shape and scale. While in local winter, the diurnal variation in North is more significant than the one in South. During the night, $NmF2$ is at the same level in both hemispheres, but since sunrise period, the one in North, red line, increases much faster than the one in South, cyan one. In Figure 5.3b, during local winter, the $NmF2$ in North is almost twice as the one in South during the noon.
- By checking the $NmF2$ at the same period during the year in different solar periods, we can find the difference between solar minimum and maximum is enormous. The $NmF2$ is about twice or more in 2014 than in 2007 at the same season.
- Comparing the left and right panels, we could find the winter maximum in North is more significant in both amplitude and duration in solar maximum than in solar minimum, i.e., the difference between red and blue lines are larger in right plot. It also agrees with the result in [62].

Based on the same data sets, the seasonal effects on ionospheric contribution to TEC, $IONf$, is studied. Figure 5.4 are the similar plots like figure 5.3, but for $IONf$. From these two plots, one can also find the systematic diurnal variation in $IONf$ like the one shown in $NmF2$. The minimum value of $IONf$ during the day moves with the local time of sunrise. The minimum happens at the same time during the same season in both hemispheres. The time of sunrise in local winter is later than in local summer, the minimum value of $IONf$ shows the great agreement in all the cases. In general, ionosphere contributes more to the TEC in summer than winter due to the more photoionization brought by the longer solar hours. The peak value of $IONf$, occurs around noon in all the cases. Besides, $IONf$ in solar maximum is greater than the one in solar minimum thanks to the higher solar activity.

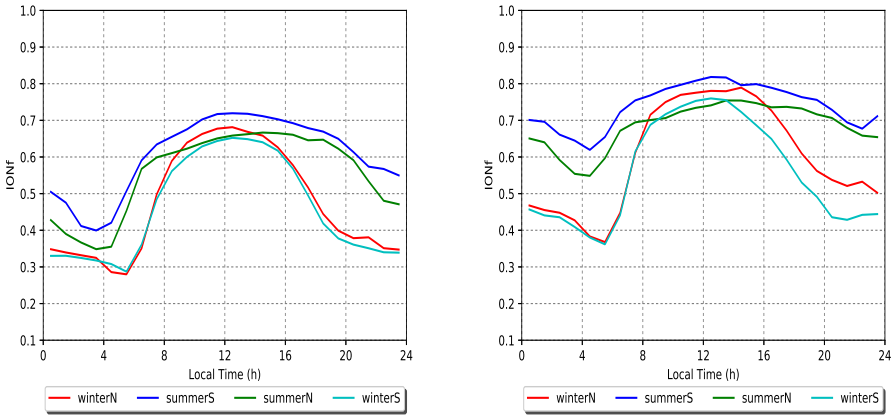

(a) 2007 (b) 2014

Figure 5.4: Diurnal variation of $IONf$ during local winter/summer. Red line – local winter in North; blue line – local summer in South; green line – local summer in North and cyan line – local winter in South.

From $IONf$, one can still find the winter and seasonal sunrise anomalies. During the noon in North, there is a reduction of ionospheric contribution to TEC in summer, and enhancement of $IONf$ in winter comparing to the same period in South, which results in the $IONf$ of local winter in North, red line, is bigger than the one of local summer in South, blue line, during both solar minimum and maximum. Besides, the $IONf$ in winter increases faster than the one in summer during the sunrise, which is more significant in the right plot, solar maximum.

However, different from the feature shown in $NmF2$, the peak values of $IONf$ are quite similar in local winter and summer in both hemispheres, i.e., there is no significant seasonal difference in peak value of $IONf$ as shown in $NmF2$. Moreover, the hemispheric difference is also not so evident for $IONf$ at the same season. For instance, in 2014, there is huge difference in $NmF2$ around noon in North and South, while for $IONf$, the values in both hemispheres are quite similar. These points are advantages to differentiate the plamaspheric TEC from the ionospheric one. $IONf$ is more suitable to model thanks to the fewer dependency factors.

Finally, by checking the quantity of $IONf$, one could find the $IONf$ at night in 2007 is generally smaller than 0.5, i.e., plasmaspheric contribution weights more than ionospheric one.

Ionospheric maps in Equinoxes and Solstices

Figure 5.5 is a group of plots showing the $NmF2$ distribution in the whole world in different periods of the year, 2007, DS (top), JS (middle) and ME (bottom) for two epochs of the day: day-time (left column) defined as LT in [10, 18] h, and night-time (right column), LT in [20, 4] h. Figure 5.6 is similar to 5.5, but based on the ROs in 2014. Mean value of $NmF2$ is calculated in a longitude bin of 10^o, and a latitude bin of 5^o, and represented by the colour. The contour lines represent the magnetic dip.

[62] used the IGS GIMs to analyse the ionosphere in 1999 – 2009, and it concluded the semi-annual anomaly is globally recorded at noon, especially at mid and low geomagnetic latitudes, and its amplitude has a close relationship with the solar activity. This is in agreement with the results shown in Figure 5.5a and 5.6a. $NmF2$ in equinox, bottom rows, is generally greater than the ones in solstices, middle and top rows and during high solar activity the difference is larger, since he maximum $NmF2$ in 2014 is 2.58×10^6 el/cm^3, twice the value in 2007. Besides, at night during solar maximum, Figure 5.6b, the semi-annual anomaly is also recorded near magnetic equator.

The top panels of Figures 5.5 and 5.6 are based on the ROs in DS, when is the local summer time for South. Around the Weddell Sea region, we could find there is obvious enhancement of the $NmF2$ value during the night comparing to the daytime map, both in solar minimum and maximum, i.e., Weddell Sea Anomaly (WSA).

Besides, from the plots in solstices, the top and middle panels of Figures 5.5 and 5.6, the plots obtained from ROs in DS and JS, respectively, one can find the hemispheric difference caused by local summer/winter is more obvious during the night. Moreover, by comparing the $NmF2$ maps in solar minimum and maximum, during same season and diurnal period, the most remarkable difference between these two years is the scale, $NmF2$ in 2014 is much larger than the one in 2007.

Based on the same data set for $NmF2$, the $IONf$ distribution of ROs is also checked. Figures 5.7 and 5.8 are the $IONf$ maps similar to the corresponding $NmF2$ maps in Figures 5.5 and 5.6, respectively. $IONf$ maps show different features from the $NmF2$, since the former is a ratio representing the ionospheric contribution to TEC. By checking the maximum value (see colorbar scale) in the different plots, one could find that the difference of maximum value of $IONf$ in different periods of the day, of the year, and of the solar cycles is within 10%, while $NmF2$ could vary in a big range as was showed in the previous plots.

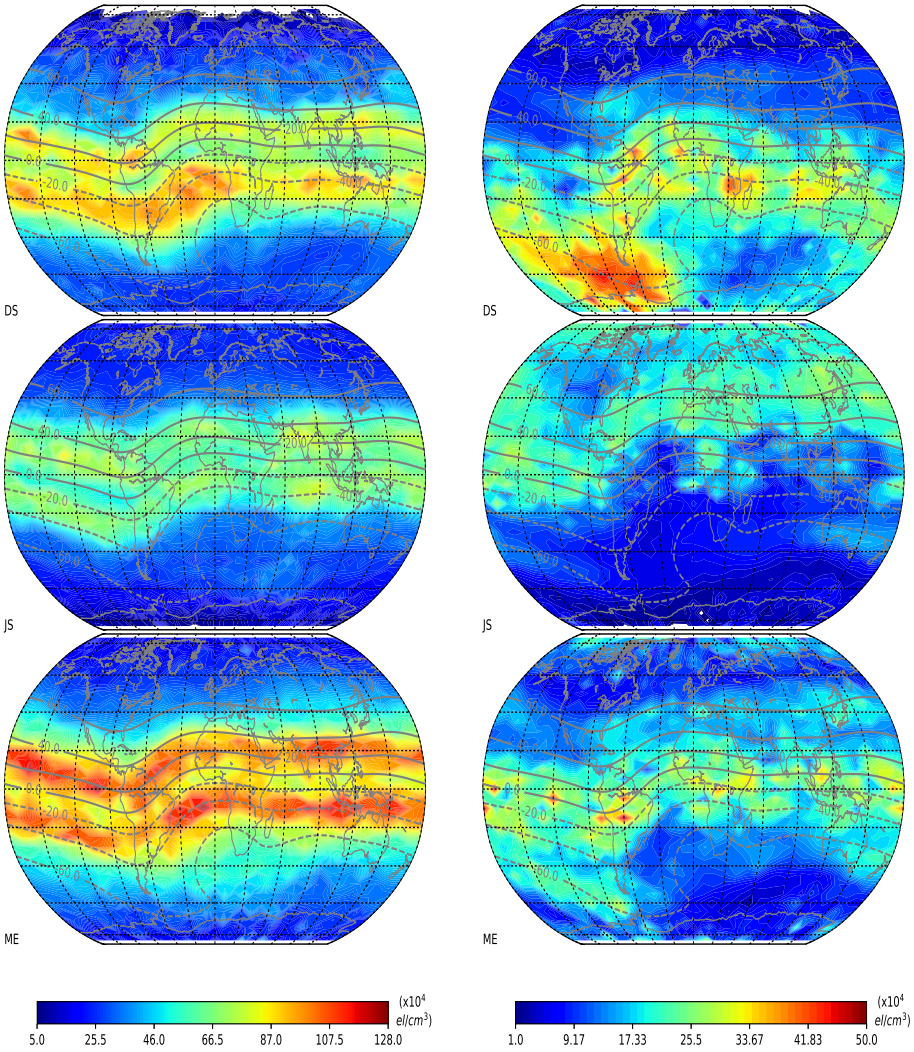

(a) day, LT in [10, 18] h (b) night, LT in [20, 4] h

Figure 5.5: $NmF2$ map in 2007. The left plots corresponds to day-time ROs, the right ones represent night time. Top – DS, middle – JS and bottom – ME.

Semi-annual anomaly could still be found in $IONf$. The $IONf$ in ME is obviously larger than in JS for both day and night and solar minimum and maximum. In other words, the ionospheric contribution to the TEC is higher in equinoxes than during solstices. $IONf$ irregularity in WSA region is also found both in solar minimum and maximum. While EIA could not be found through $IONf$. From the day-time plots, Figure 5.5a and 5.6a,

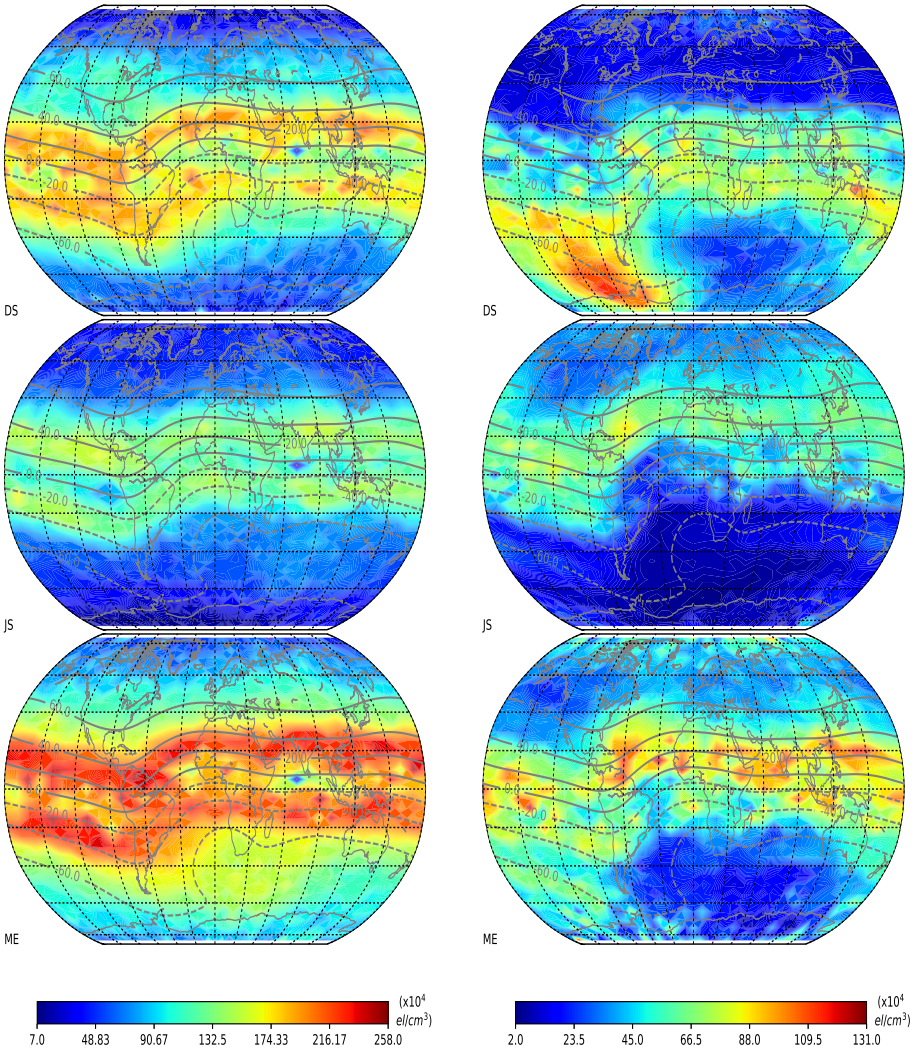

(a) day (b) night

Figure 5.6: $NmF2$ map in 2014, similar as Figure 5.5.

we can find EIA from $NmF2$ map in both equinox and solstice. However, according to the height structure of the EIA and the computation of $IONf$, which is an vertical integration of shape function $F(h)$ along the altitude, we could find that $IONf$ is not suitable in detecting the EIA.

From the above $IONf$ maps during the night-epoch, Figure 5.7b and 5.8b, a clear longitude dependence is shown besides the hemispheric difference. Agreed with the occurrence time of spread F, which is a post-sunset and

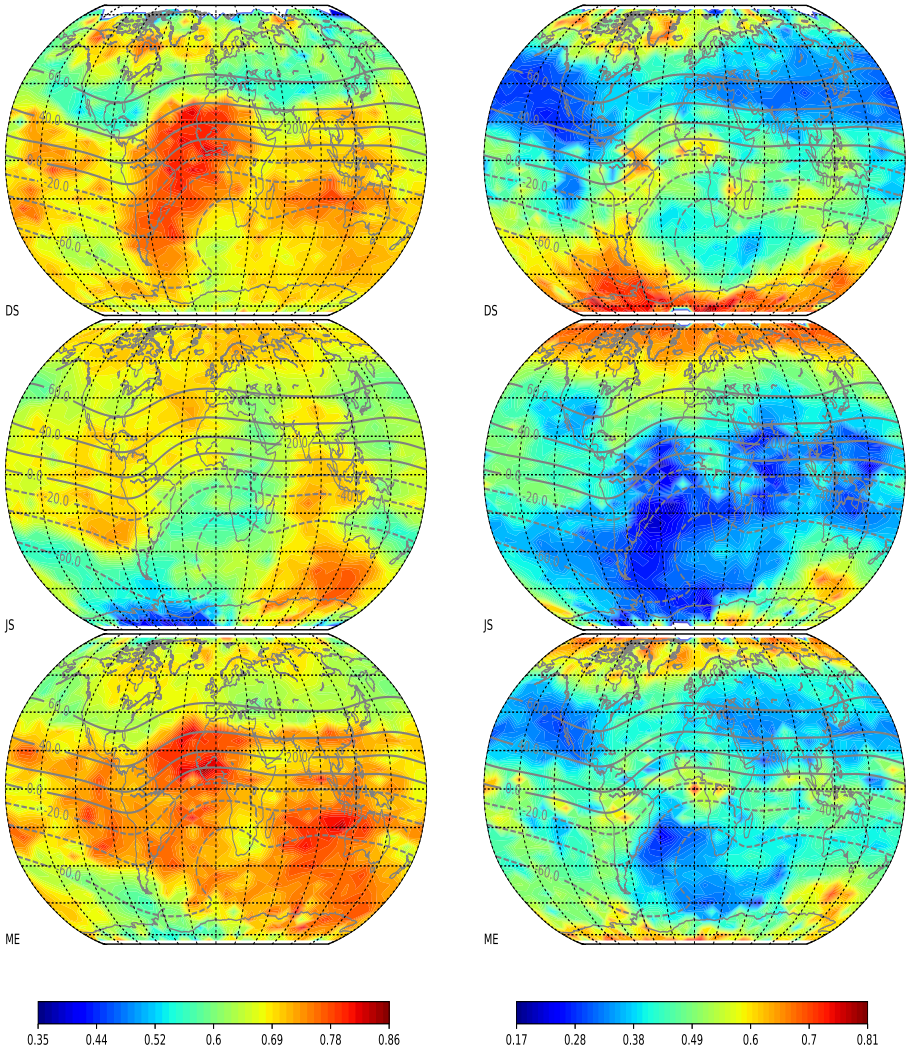

(a) day (b) night

Figure 5.7: $IONf$ map in 2007

night phenomenon, as we mentioned in previous chapter. The irregularity of $IONf$ could be found in the South Atlantic ocean, where $IONf$ is smaller than the ones in surrounding areas. In other word, the enhanced ionospheric conductivity causes the reduction of ionospheric contribution to the TEC.

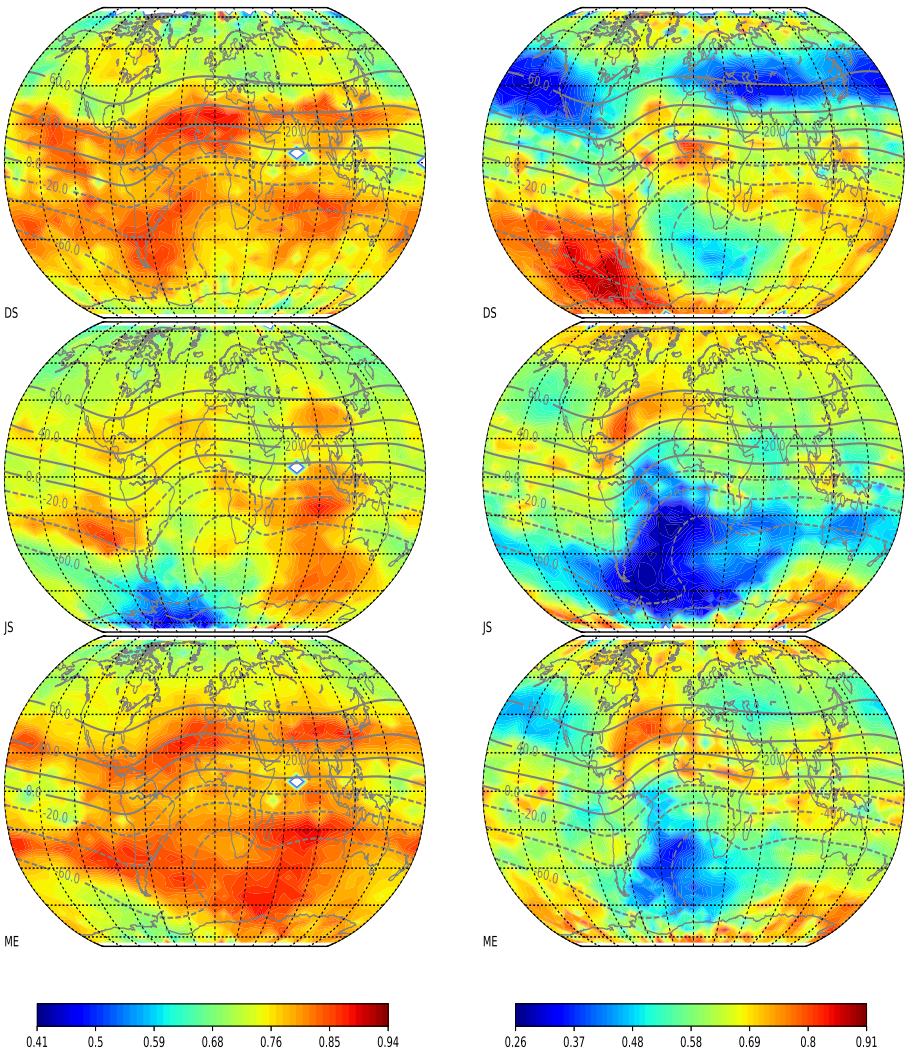

(a) day (b) night

Figure 5.8: $IONf$ map in 2014

Annual anomaly

In order to check the annual anomaly, the ROs in December and June are selected in 2007 and 2014.

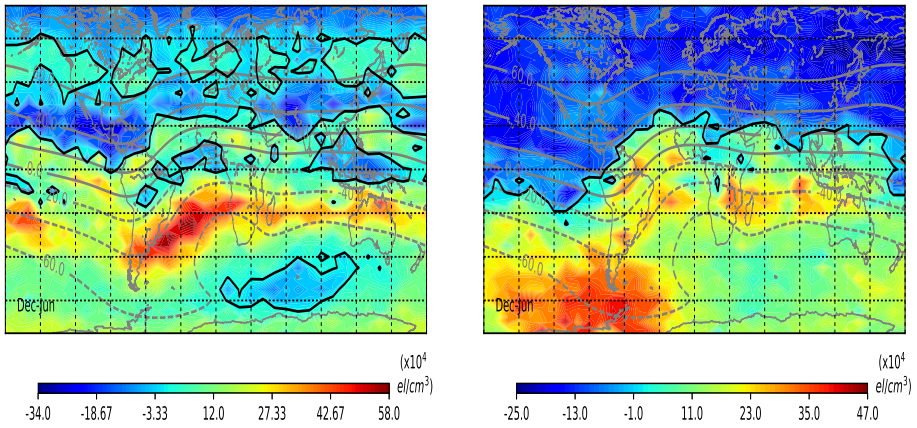

(a) day (b) night

Figure 5.9: $\Delta NmF2$ map ($NmF2_{Dec} - NmF2_{Jun}$), in 2007. The black contour line represents zero value.

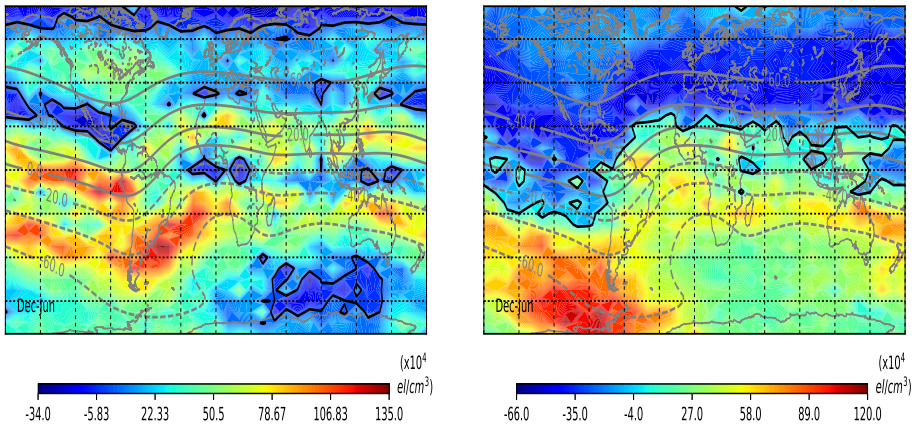

(a) day (b) night

Figure 5.10: $\Delta NmF2$ map in 2014.

Figure 5.9 shows the difference between the mean $NmF2$ in December and June, 2007, i.e., $NmF2_{Dec} - NmF2_{Jun}$. The black contour line represents

zero value, i.e., $NmF2_{Dec} = NmF2_{Jun}$. The positive value means that the $NmF2$ in December is larger than the one in June. These results are similar to those in Fig.6 in [59].

Figure 5.9a is based on the ROs during the day, within LT [10, 18] h. The majority of the whole world has the positive value, and the maximum positive value is 5.8×10^5 el/cm^3, which is larger, in absolute value, than the minimum negative value, -3.4×10^5 el/cm^3. Hence, we can derive that during the day, the $NmF2$ in December is larger than the one in June on average.

In [59], it was reported that the annual anomaly exhibits strong enhancements over southern EIA crest latitudes during day time and around WSA region during night time. Moreover, one can find the annual anomaly is more significant around EIA crest, especially in SAMA region. Figure 5.9b corresponds to the night-time period, LT after 20 h, and before 4 h. Due to the winter/summer effects, the $\Delta NmF2$ in North is negative, while it is positive in South, i.e., the seasonal dependency is stronger at night. However, in low magnetic dip and near magnetic equator, there is still the annual anomaly. And the value distribution is not symmetrical, i.e., the maximum positive difference, 4.7×10^5 el/cm^3, is almost twice as the minimum value of the difference, -2.5×10^5 el/cm^3. Furthermore, large $\Delta NmF2$ appears around WSA region due to greater electron density in this region at night in the local summer, December. In one word, the annual anomaly also exists during the night.

The same methodology is applied to the quantity $IONf$, Figure 5.11 and 5.12 are obtained, which are the $\Delta IONf$ maps. The annual anomaly is also found in $IONf$, i.e., the ionospheric contribution to the TEC is higher in December than in June. However, different from $NmF2$, the dependency of solar activity is not so evident for $\Delta IONf$. In other words, the $IONf$ is more stable. And the greatest values appear in SAMA and WSA regions, both during the day and night.

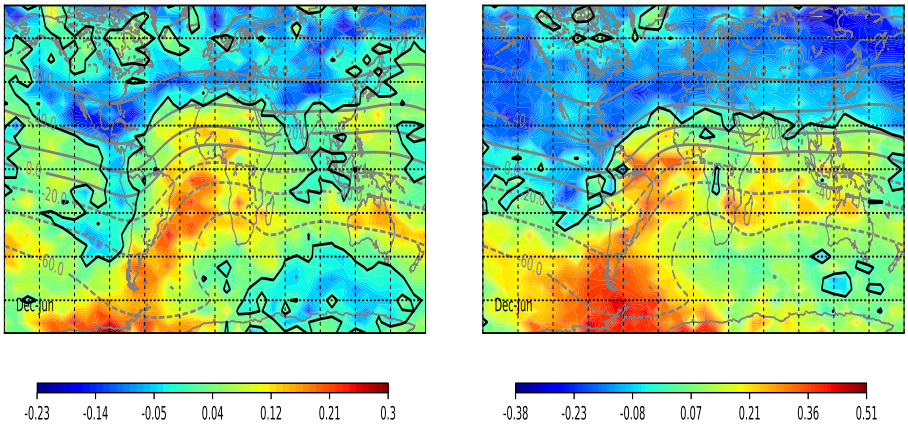

(a) day (b) night

Figure 5.11: $\Delta IONf$ map ($IONf_{Dec} - IONf_{Jun}$), in 2007. The black contour line represents zero value.

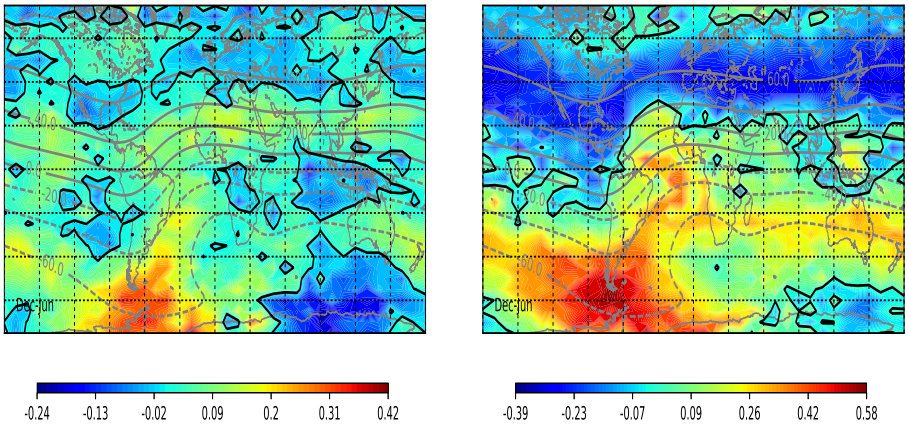

(a) day (b) night

Figure 5.12: $\Delta IONf$ map in 2014

5.2.4 Magnetic dip Variation

In this section, we will check the $IONf$ distribution in different magnetic dip. Based on the previous study, we know that there is significant difference of $IONf$ caused by seasons. Thus, the whole data set will be separated by periods like in the previous section. And the whole world is divided into different regions by magnetic dip, which are calculated by using International Geomagnetic Reference Field (IGRF) model, 12th generation [42].

Figure 5.13 are a group of plots showing the diurnal variation of $IONf$ in different dip bins, seasons, solar cycles. The North/South is divided into three regions: 1) the low dip region, i.e., near magnetic equator, the dip within [0^o, $\pm 30^o$], represented by the green lines in the plots. 2) the middle dip region, within [$\pm 30^o$, $\pm 70^o$], blue lines. 3) the high dip region, i.e., magnetic polar region, [$\pm 70^o$, $\pm 90^o$], red lines. The dash lines in each plots represent South, while the solid lines correspond to North. The plots in the left – (a), (c) and (e), are based on the ROs in 2007, and the right – (b), (d), (f), correspond to 2014. And the ROs are selected by the seasons: the top shows $IONf$ derived from ROs in local summer, i.e., the ROs in North during JS and in South during the DS; the middle represents local winter, the ROs in South during JS and in North during the DS; and the bottom ones are based on ROs in SE.

Figure 5.13a is the diurnal variation of $IONf$ in local summer, in 2007. In general, the higher latitude, the flatter diurnal variations, which is linked to more photoionization caused by longer sunlight period. Since in local summer, the higher latitude, the longer day-time. The difference of $IONf$ value in different dip bins are constrained to post-midnight and morning periods mostly, while the peak values of $IONf$ are more or less in the same level in different magnetic dip, around 0.7 with the fluctuation within 10%. However, the minimum value of $IONf$ changes dramatically in different dip. Near magnetic equator, there is more time for the recombination process. Hence, $IONf$ could reach lower value. The location of minimum value of $IONf$ follows the sunrise time in different dip.

Figure 5.13b is also the diurnal variation in local summer, but for 2014. By comparing to the ones in solar minimum, Figure 5.13a, one could find that the day-time $IONf$ in these two years have the same shape, staying at a constant level during the day. The peak values of $IONf$ in solar maximum, around 0.75, are slightly higher than the ones in solar minimum, around 0.7. While from post-sunset till sunrise, the variations of $IONf$ show more difference between these two year. In solar minimum, the $IONf$ decreases gradually just after sunset, while there is a delay in solar maximum, i.e. $IONf$ still stays at high level after sunset, and it drop quickly at midnight, and hits its bottom in a short time. However, the minimum $IONf$ appears at the same LT for the same dip range in different solar cycle, but with the different levels in these two years. The bottom value of $IONf$ is much greater in solar maximum than in solar minimum. For instance, near magnetic equator, the minimum $IONf$ is around 0.2 in 2007, while it is around 0.5 in 2014. finally, we should point out that all the difference mainly happens in middle dip and near magnetic equator regions. Actually, the $IONf$ in polar region in these two years are quite similar.

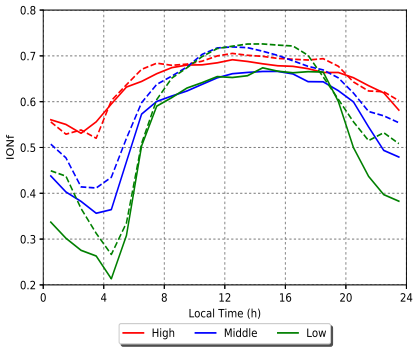

(a) Summer, 2007

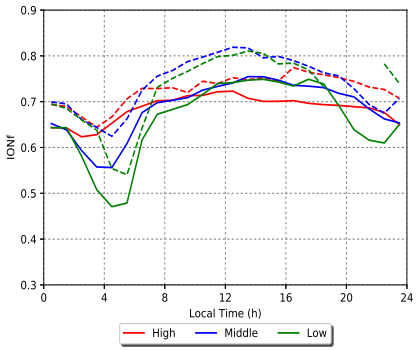

(b) Summer, 2014

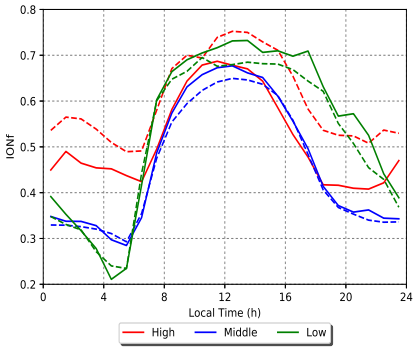

(c) Winter, 2007

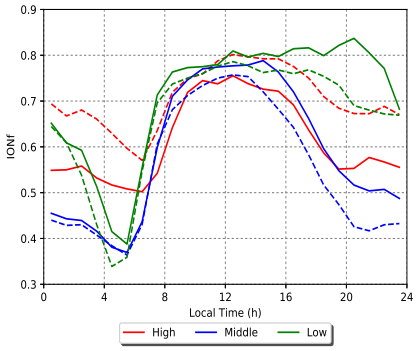

(d) Winter, 2014

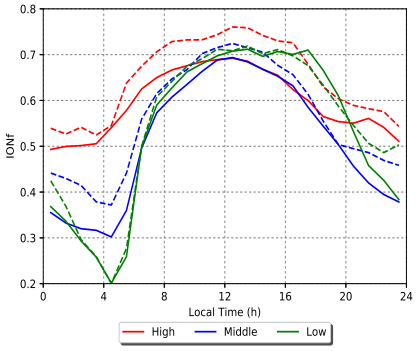

(e) Equinox, 2007

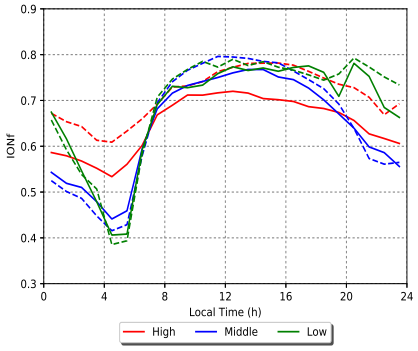

(f) Equinox, 2014

Figure 5.13: Diurnal variations of $IONf$ in different dip bins. The left – (a), (c) and (e), are based on the ROs in 2007, and the right – (b), (d), (f), correspond to 2014. The dash lines in each plots represent South, while the solid lines correspond to North.

The middle plots, Figure 5.13c and 5.13d, are the diurnal variation of $IONf$ in local winter in 2007 and 2014 respectively. And the bottom panel is the one corresponding to the equinox. The same dip dependency occurs in all these plots, i.e., the diurnal variation becomes more significant equatorwardly. The difference caused by solar cycle mainly appears near magnetic equator region. In this region, during post-sunset period, there is an enhancement of $IONf$ in solar maximum in both local winter and equinox, which may link to the stronger equatorial spread F in solar maximum. Since in [56] used the equatorial stations to show the increment of spread F with increasing solar activity. Due to this enhancement, in 2014, the lowest values of $IONf$ near magnetic equator, which just occurs before sunrise, become greater and are around 0.4, similar to the corresponding value in middle dip region. While in 2007, the the minimum near magnetic equator is more than 0.1 smaller than the minimum in middle dip region.

Furthermore, by checking the $IONf$ variation in the same dip region in the same season and year, but in different hemispheres, i.e., comparing the solid and dash lines in the plots, one can find that with respect to other factors, diurnal, latitudinal, seasonal, yearly dependency, the hemispheric difference is quite small. The $IONf$ variation in different hemispheres are quite similar.

Mid-latitude trough

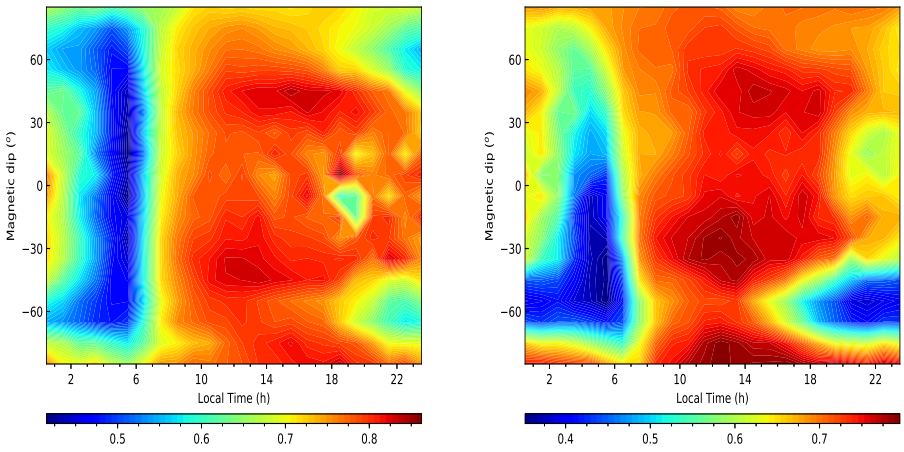

(a) ME, 2014 (b) JS, 2014

Figure 5.14: $IONf$ in 2014. The x-axis – LT, y-axis – magnetic dip, and the colour represents the mean value of $IONf$ in pixel.

Figure 5.14a shows the $IONf$ distribution along the LT, x-axis, and magnetic dip, y-axis, for ROs in ME, 2014. The mean value of $IONf$ is calculated within $1h$ LT and 10^o magnetic dip bin, and represented in colours. After 18 h, there is a clear reduction of $IONf$ around $\pm 60^o$ comparing to the surrounding areas. And this phenomenon lasts till almost 4 h, the sunrise period. It agrees with the fact that the mid-latitude trough is primarily a night-time phenomenon. And $IONf$ is a quantity that could be used to check this feature. Figure 5.14b is the similar plot for ROs in JS, 2014. The $IONf$ distribution is not symmetrical along the magnetic dip due to the winter/summer seasonal affects. In the local winter hemisphere, South in JS, mid-latitude trough around -60^o could be found earlier during the day, around 14 h. And it is more clear than the one in equinox. While in local summer, there is a trough appearing around 60^o at mid-night, LT after 22 h till 2 h. However, comparing to the one in South, it is much less evident.

Due to the fact that the mid-latitude trough is a night-time phenomenon, and it is more evident in equinox and local winter, we will check the night-time $IONf$ maps.

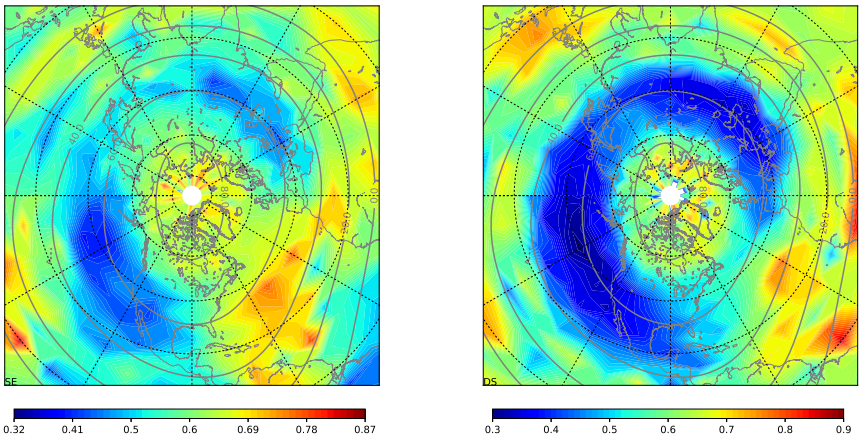

(a) SE, 2014 (b) DS, 2014

Figure 5.15: Mid-latitude trough in North, 2014

Figure 5.15a and 5.15b shows the night-time $IONf$ maps in North in SE and DS, 2014, which are local autumn and winter respectively. The map is in Polar Stereographic Projection. The night-time epoch is defined as LT from 20 h till 4 h, i.e., the ROs within this time range are chosen for these plots. From these two plots, one can find that the trough takes the form of a band a few degrees wide in latitude of the auroral oval during the winter and equinoctial months. As shown in Figure 5.14, the trough in local winter

is more significant than in equinox, but it has the similar distributions along the world during the Two periods of time.

Furthermore, Figure 5.14 shows the trough in South, while Figure 5.15 shows the through in North. Hence, we can conclude that the mid-latitude trough can be observed in both South and North.

Besides, by checking the same plots in 2007, we could find the similar features in solar minimum.

5.3 EC_{ion} and EC_{pl} variations

As commented previously, once we obtain $IONf$, with the known TEC, we can get EC_{ion} and EC_{pl} following the relationships: $EC_{ion} = IONf \cdot TEC$ and $EC_{pl} = (1 - IONf) \cdot TEC$. In this section, we will study the characteristics of ionospheric and plasmaspheric electron densities.

5.3.1 Diurnal variation

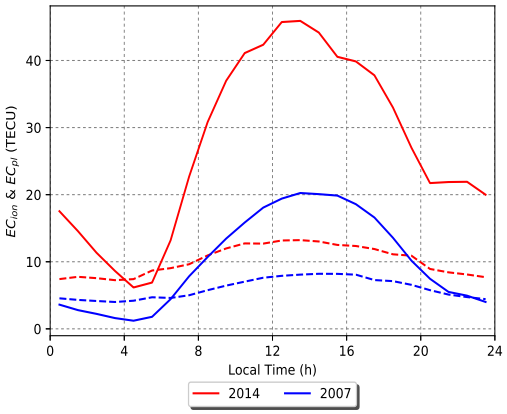

Figure 5.16: The local time variation of EC_{ion} and EC_{pl} for ROs closed to the magnetic equator. Red solid line – EC_{ion} in 2014; red dash line – EC_{pl} in 2007; blue solid line – EC_{ion} in 2007 and blue dash line – EC_{pl} in 2007.

Figure 5.16 shows the local time variation of EC_{ion}, the solid lines, and EC_{pl}, the dashed lines, in red for 2014 and in blue for 2007. The plot is based on the same data set as used in Figure 5.1, for the ROs close to magnetic equator, dip angle within the range $[-20^o, 20^o]$. Since it is in low dip region, we have used the ROs from the whole year, without any separation according

to the season. EC_{ion} shows the similar trends like $IONf$, The lowest values occur just before sunrise. However, EC_{ion} reaches its peak around noon, but afterwards there is no stable period and the value decreases. Especially in 2014, shortly after it reaches the top point, it begins to decrease. EC_{ion} in 2014 is much larger than in 2007. The maximum difference is around 25 $TECUs$, which happens at noon, while the minimum difference is about 5 $TECUs$, just before sunrise. Moreover, when we look at the diurnal variation of EC_{ion} in these two years, we can find that it has much steeper slope of variation in solar maximum than minimum. The diurnal difference could reach 40 $TECUs$ in 2014, while it is around 20 $TECUs$ in 2007. Compared to EC_{ion}, EC_{pl} seems more stable. The diurnal variation of EC_{pl} is less than 6 $TECUs$ in both years. It maintains more or less the same shape in the different periods of solar cycle, while EC_{pl} shifts several $TECUs$ above from solar minimum to maximum in general.

5.3.2 Seasonal variation

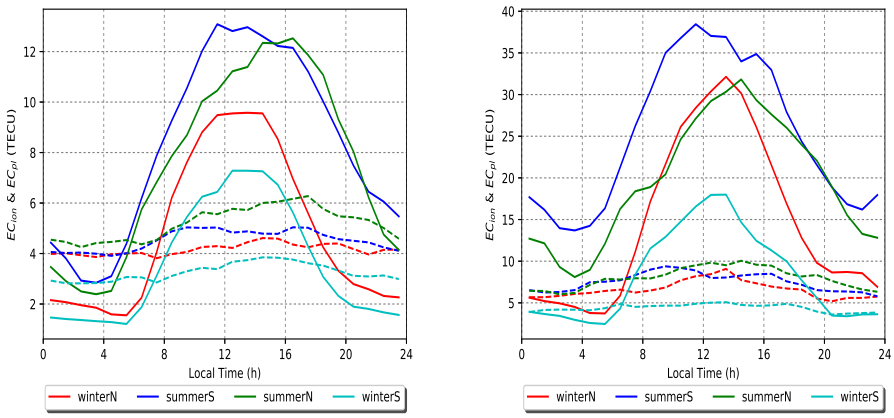

(a) 2007 (b) 2014

Figure 5.17: Diurnal variation of EC_{ion} and EC_{pl} during local winter/summer in North/South. The solid line represents the EC_{ion} and dash line for EC_{pl}. Red line – local winter in North, blue line – local summer in South, green line – local summer in North and cyan line – local winter in South.

Figure 5.17 show the diurnal variation of EC_{ion}, noted as solid lines, and EC_{pl}, shown with dash lines in local winter/summer in both hemispheres. The ROs within the dip range [$\pm 20^o$, $\pm 70^o$] are chosen. The red line represents the local winter in North, blue line is local summer in South, green

line is summer in North and the cyan line is winter in South.

Figure 5.17a is based on ROs in solar minimum. During solar minimum, in both hemispheres, there is clear separation in EC_{ion} between summer and winter, i.e., it is larger in summer than winter during the whole day, the difference could reach about 6 $TECUs$ around the noon, in South, while the maximum value of EC_{ion} is around 12 $TECUs$. Besides the seasonal variation, there is also significant diurnal variation of EC_{ion}. The diurnal variation is greater than the seasonal one, which the difference between the peak and bottom values could reach 10 $TECUs$. Similar to EC_{ion}, EC_{pl} also shows the seasonal and diurnal variation, but in much smaller scale, within 2 $TECUs$ variation with the peak value at 6 $TECUs$. Moreover, one can find that in 2007, EC_{ion} is larger than EC_{pl} during the day, however, it becomes smaller than EC_{pl} during the night.

Figure 5.17b corresponds to solar maximum. In solar maximum, there are similar features as in 2007, but in a larger scale. The diurnal difference of EC_{ion} could reach 25 $TECUs$ and seasonal difference could be around 20 $TECUs$. Besides, the difference caused by the solar cycle could be around 28 $TECUs$. However, the diurnal, seasonal, annual difference of the EC_{pl} are maintained within few $TECUs$. But there are different characteristics in solar maximum comparing to the solar minimum period. In North, during the noon around [9, 15] h, EC_{ion} in local winter is larger than in local summer during the day, which is not shown in Figure 5.17a. This coincides with the winter anomaly, which is seen mostly in the North hemisphere during solar maximum. However, we cannot find this feature in EC_{pl}. Furthermore, in local summer in both hemispheres, the EC_{ion} is always bigger than EC_{pl} during the whole day.

5.3.3 Magnetic dip dependencies

Figure 5.18 shows magnetic dip variations of EC_{ion} and EC_{pl} in different seasons for ROs in 2007. The whole year is divided into four seasons and represented by different colour lines in each plot: red line – ME, green line – SE, blue line – DS and cyan one – JS. Tow periods of the whole day are chosen, day-time – LT in [10, 16] h, and night-time – LT after 22 h and before 4 h. The top plots are the EC_{ion} during the day and night respectively. While the ones in bottom represent the EC_{pl}.

Figure 5.18a is the EC_{ion} during the day. EC_{ion} in ME, red line, is bigger than the one in solstices, cyan and blue lines, which matches the ionosphere semi-annual anomaly. There is no obvious winter/summer difference observed in daily EC_{ion}, except the ROs in DS, blue line, the value in South, in local summer, is slightly bigger than the one in North, in local winter.

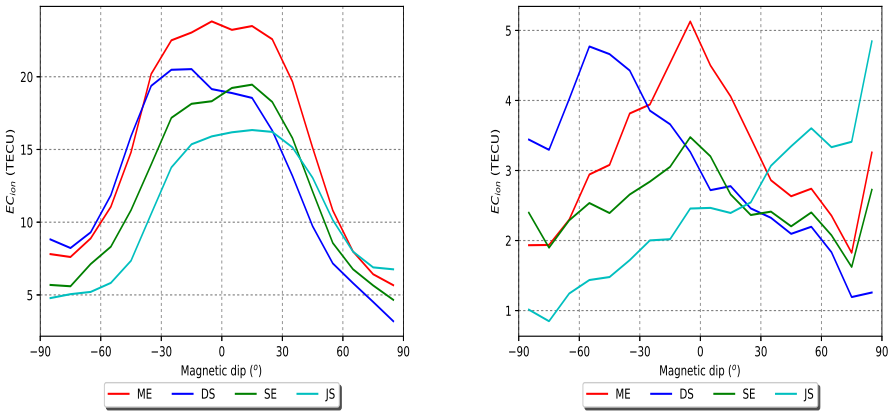

(a) EC_{ion}, day

(b) EC_{ion}, night

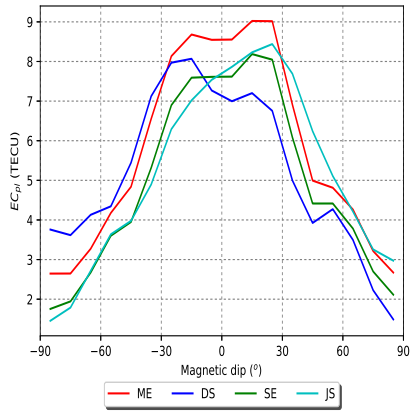

(c) EC_{pl}, day

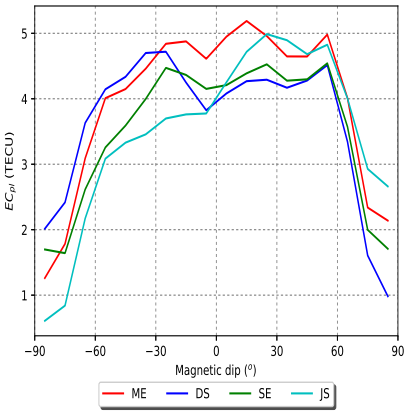

(d) EC_{pl}, night

Figure 5.18: Magnetic dip variation of EC_{pl} and EC_{ion} in different seasons, 2007. Red line – JS, green line – SE, blue line – DS and cyan one – ME.

The EC_{ion} in DS is generally higher than the one in JS, i.e., the ionospheric annual anomaly. Furthermore, the EC_{ion} in magnetic equator is maximized and decreases as the dip increases in the two hemispheres.

Figure 5.18b is the EC_{ion} during the night. There is a clear winter/-summer difference in EC_{ion} during the night. i.e., the seasonal variation in ionosphere is more obvious during the night than in the day. The day-time EC_{ion} is within the range from 3 $TECUs$ to 25 $TECUs$. In other words, the variation caused by magnetic dip and seasons could be around 20 $TECUs$ during the day. While the values of night-time EC_{ion} in 2007

are constrained to 5 $TECUs$. By comparing the day-time and night-time EC_{ion}, one could also find that the diurnal variation of EC_{ion} could also reach 20 $TECUs$ in 2007.

Figure 5.18c and 5.18d shows the EC_{pl} in both day and night respectively. EC_{pl} near magnetic equator is the greatest compared to the other dip regions and the values close to magnetic poles are the smallest in the different seasons, both during the day and night. Since the majority of a magnetic flux tube's volume is centred around the magnetic equator, where $Ne(H^+)$ varies slowly. From magnetic equator, the ion H^+ diffuses down the field line into the two hemispheres [71]. During the day, within $\pm 30^o$, the EC_{pl} stays at high scale, and it drops quickly polewardly. However, during the night, the EC_{pl} keeps more or less the same value within $\pm 60^o$. There is winter/summer difference shown in both plots, cyan and blue lines. EC_{pl} in local summer is higher than in local winter, with the peak values occurring at around 30^o. However, by comparing Figure 5.18d with 5.18b, EC_{pl} and EC_{ion} during the nights, one can find more significant seasonal variation in EC_{ion}, when these two values are at the same scale.

Figure 5.19 are similar plots like 5.18, but for ROs in 2014, solar maximum. In general, EC_{ion} and EC_{pl} show the consistent features appearing in 2007. However, there are also some relevant differences.

In general, the ionosphere in solar maximum is more active. The maximum value of EC_{ion} during the day reaches to 60 $TECUs$, shown in Figure 5.19a, almost triple as the day-time EC_{ion} in solar minimum, which is less than 25 $TECUs$, while EC_{ion} during the night at solar maximum, Figure 5.19b, is almost four times as the one in solar minimum. Thanks to higher level of EC_{ion} during solar maximum, the difference related to dip regions is also enhanced. For instance, the difference between magnetic equator, peak value, and magnetic polar, minimum value, is almost 40 $TECUs$ in ME. Besides, the annual anomaly is more obvious, blue line is above the cyan one. However, the winter/summer difference is still not clear in EC_{ion} during the day. Similar to EC_{ion}, EC_{pl} level is also enhanced in solar maximum. However, the increasing scale is much smaller than the EC_{ion}.

Finally, one could conclude that EC_{ion} is more sensitive to the environment compared to EC_{pl}. EC_{ion} varies diurnally, seasonally, latitudinal in a large scale. It also depends on the solar activity. Meanwhile, EC_{pl} also has its own variation according to the environment, which is different from the EC_{ion}, but it is relatively more stable.

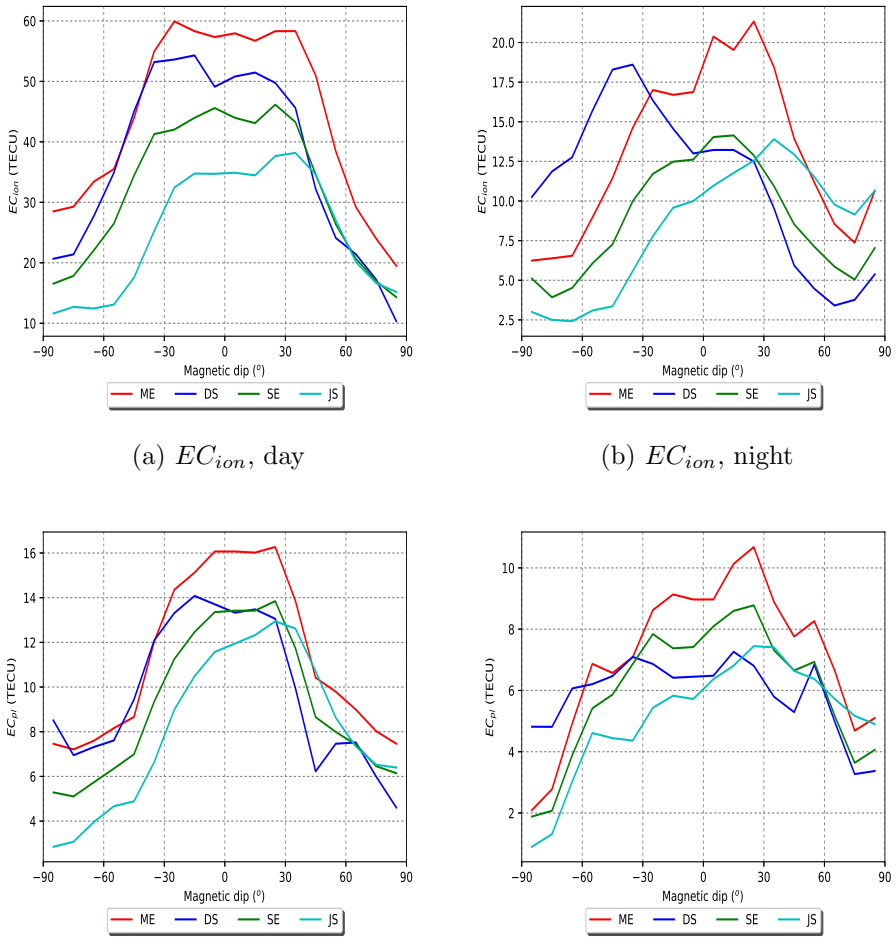

(a) EC_{ion}, day

(b) EC_{ion}, night

(c) EC_{pl}, day

(d) EC_{pl}, night

Figure 5.19: Magnetic dip variation of EC_{pl} and EC_{ion} in different seasons, 2014

5.4 Ionospheric Charging Process – Capacitor Model

5.4.1 Capacitor Model and fitting criteria

In the previous sections we have shown that $IONf$ is a quite stable parameter, much more than EC_{ion} or EC_{pl}. In this section, we want to evaluate if it is possible to build a simple model for predicting the evolution of this ratio along the local time.

We can find a consistent phenomenon from the $IONf$ diurnal variation. The $IONf$ hits its bottom values just before the sunrise, then it climbs to

its highest value and keeps at same level till sunset. Notice that for different epochs, the LTs of sunrise and sunset can be deruived easily form the local coordinates and the day of the year. So the only question to solve is a model for the transition of $IONf$ from sunrise to noon. The whole trend is similar to the charging process of a capacitor. Hence, in this section, we will study the charging process of ionosphere by capacitor model described by the following equation 5.1:

$$IONf_{capacitor} = v_0 + (v_{max} - v_0) \times (1 - e^{(\frac{-(t-t_0)}{\tau})}) \tag{5.1}$$

Here, v_{max} is the maximum $IONf_{capacitor}$ value reached during the day, v_0 is the initial value of $IONf_{capacitor}$ at the start time t_0, near sunrise. Finally, τ represents the response timescale of the whole charging process.

In order to achieve more realistic fitting result. There are several points that must be considered by the model:

- Based on the previous study, we find that there are obvious seasonal and magnetic latitudinal effects in diurnal variation. Thus, the whole data set are separated by four seasons: ME, JS, SE and DS. Then, the data set of each season is divided into subsets according to different ranges of dip angles.

- The set of ROs, which could reflect the ionospheric charging process, should be chosen at least covering the sunrise period. The time range of charging process is decided by tracking the mean $IONf$ trend along the LT of distinct data set. There are two different ways of calculating the mean $IONf$ along the time.

  1) Equal LT-bin. Since we want the mean $IONf$ along the time, we can simply set a fixed time bin to select the ROs which happens in this time range, and calculate the mean value.
  2) Equal number set. An equal number of ROs, collected in successive time order, is chosen to calculate the mean value.

  In this study, the method 2 is chosen, since the RO measurements are not evenly distributed in the whole day. In this way, each RO is valued equally, and it will detect the changes along the LT more sensitively rather than the method using a fixed time bin. An example of applying both methods is shown below.

- Set the reasonable ranges of the model parameters, t_0, v_0 and v_{max} for fitting. All the parameters in this model should have physical meaning, i.e., those three parameters are not fully free. Besides, the ionosphere varies greatly in different conditions. Hence, we can not

use the same ranges of t_0, v_0 and v_{max} for different data set. For instance, the starting time, t_0, could be around 3 h for ionosphere in high latitude during local Summer, but it may be delayed till 7 h in local Winter. In this study, all these ranges were decided by analysing the average trend of $IONf$. For example, the blue line in figure 5.20, the minimum $IONf$ and its corresponding time could be obtained, besides, the maximum $IONf$ can be found. By adding some fixed margin to these values, we can get the reasonable ranges for model parameters.

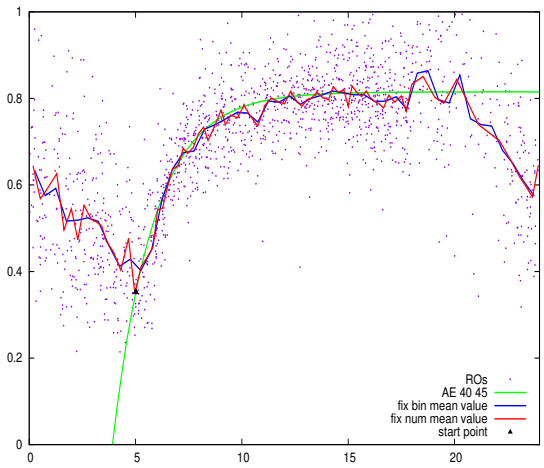

Figure 5.20: The fitting example based on the RO measurements within magnetic dip [40^o, 45^o], in SE, 2014. Purple dots are the individual $IONf$ value per RO. Green line is the Capacitor Model fitting result with starting hour shown as black filled triangle. Red line is the equal number average, 20 points. And blue line is equal bin average, 0.5h.

Figure 5.20 shows an example of Capacitor Model for ionospheric charging process. The ROs are selected within dip range [40^o, 45^o], in SE, 2014. $IONf$ of each RO is shown as the purple dots in the plot. The green line is the fitting result, with the black filled triangle representing the start point of the charging process. The blue line is the mean $IONf$ obtained in the fixed time bin, 0.5 h. While, the red line is the average trend obtained with equal number of values, 20 points. One can find that, the red line could catch more details of $IONf$ variation along the LT when the value is changing rapidly. In this example, the equal number average is better in finding the proper start point of "charging process".

5.4.2 Features of the Capacitor Model parameters

In this section, we will study the features of the model parameters, v_0, v_{max} and τ, which were obtained from best fits using the equation 5.1 based on RO sets in different seasons and magnetic dip. All dr between the fitting results and data set, defined as equation 4.11 in previous chapter, are smaller than 0.15.

Figure 5.21 shows the variation of capacitor parameters along the magnetic dip in different season in solar minimum. Figure 5.21a is the variation of v_0 and v_{max} along the dip.

The variation of v_{max}, represented as solid lines, is constraint within 0.2 around 0.7. It is quite stable in the low magnetic dips, within the dip range $[-30^o, 30^o]$, for different data sets. However, we can find some fluctuation in the region of middle magnetic dip. Outside this region, v_{max} climbs as the the dip increasing. However, shortly after it reaches the peak value in some magnetic dips, it drops quickly and hits the lowest value around 60^o. [72] addressed that the day-time F2 layer trough is present during winter conditions, under a large range of activities from disturbed to quiet. In theory, v_{max} represents the day-time ionospheric contribution to VTEC. We can find an obvious valley around dip 60^o in local winter, i.e., the blue line in $[-70^o, -40^o]$ and the cyan line in $[40^o, 70^o]$. From the study in previous section, we find the EC_{pl} is quite stable compared to EC_{ion}, in different periods of day and year. The variation of EC_{pl} is less than 10 $TECUs$ in 2007. Besides, v_{max} is around 0.7, i.e., there is more ionospheric contributions to TEC. Thus, the drop of $IONf$ can imply the obvious drop in EC_{ion}. Moreover, seasonal variation of v_{max} could be found by comparing the values at the same magnetic dip in different season. The difference could also reach 0.2 between local winter and summer in middle dip region.

While v_0, shown as dash lines, are more sensitive to magnetic dips compared with v_{max}, i.e., the variation could reach around 0.5. In low magnetic dip, the v_0 is at the bottom, and quite stable. v_0 increases polewardly. When the $IONf$ is around 0.5 or below that level, it means that EC_{ion} drops to the level of EC_{pl} or even smaller, a small change like several $TECUs$ will cause a big fluctuation in its value, since EC_{pl} is at the level of several $TECUs$. Basically, v_0 represents the lowest ionospheric contribution to TEC during the whole day. In solar minimum, v_0 is generally smaller than 0.5, i.e., plasmaspheric contribution is greater than ionospheric one before the sunrise.

Figures 5.21b show the variation of τ along the magnetic dip. τ is smaller around equator than in mid- and high- latitude. Combined with the fact that there is larger value of $(v_{max} - v_0)$ in the low magnetic dip region, one

can derive that the ionosphere climbs faster and varies more around equator during sunrise than in other regions.

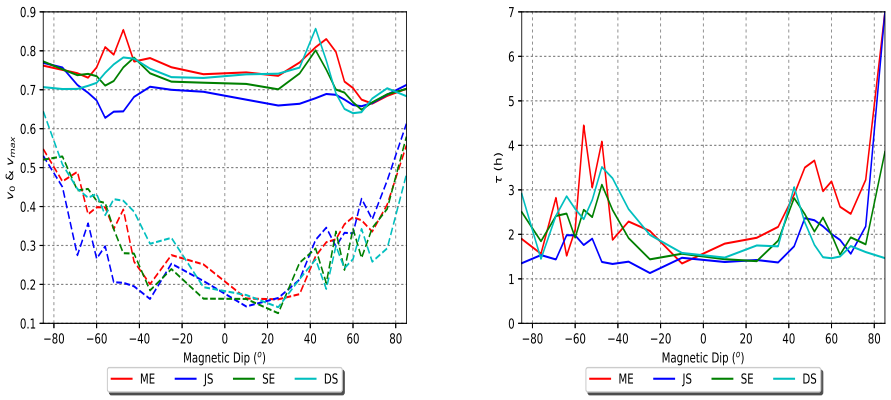

(a) v_0 (dash lines) and v_{max} (solid lines) (b) τ

Figure 5.21: The obtained parameters in capacitor model based on the ROs in 2007. ME – red lines, JS – blue ones, SE – green ones, DS – cyan ones.

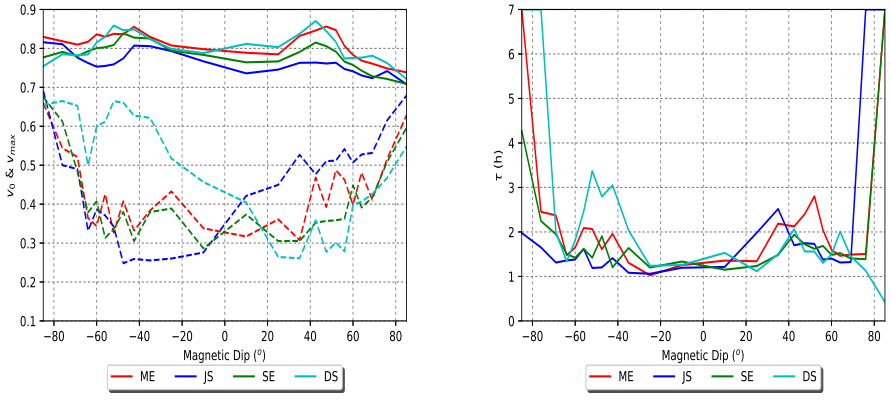

(a) v_0 (dash lines) and v_{max} (solid lines) (b) τ

Figure 5.22: The obtained parameters in capacitor model based on the ROs in 2014.

Figure 5.22 are the capacitor parameters for the ROs in solar maximum. They are consistent to the results in 2007. However, some differences can also be found.

- In solar maximum, v_{max} and v_0 are generally bigger than the ones in solar minimum. They shift 10% above generally.
- Seasonal effects on v_0 and τ are more obvious in 2014. The blue and cyan lines show a clear difference.
- In local summer, represented by the cyan line in South and green one in North, v_0 is bigger than 0.5, i.e., ionospheric contribution is always the dominant component to TEC during the whole day.

5.5 Conclusions

The TEC information obtained from the measurements of the ground-based GPS receivers, such as IGS GIMs, contains both ionospheric and plasmaspheric contributions, i.e., EC_{ion} and EC_{pl}. Based on the shape function retrieved from the RO measurements using SM aided by the TEC information, the ionospheric fractional contribution to TEC, $IONf$, can be derived. Since the TEC is used in retrivals, the shape functions represent the ratio between the Ne and the TEC at the different altitudes. Hence, by extracting the ionospheric contribution along the altitude from shape function, the $IONf$ has been obtained. Once it is computed, the ionospheric/plasmaspheric electron contents, EC_{ion} and EC_{pl}, has been computed directly using the known TEC.

The quantity $IONf$ shows the main features of the ionosphere. The diurnal, seasonal, yearly, latitudinal and longitudinal variations of ionosphere could be examined through $IONf$. It is also possible to detect and study the ionospheric anomalies by checking $IONf$, such as winter anomaly, annual anomaly, semi-annual anomaly, mid-latitude trough and others.

Furthermore, the characteristics of the ionosphere and plasmasphere in solar minimum and maximum have been checked based on EC_{ion} and EC_{pl} obtained through $IONf$. Similar as the ionosphere, there are also diurnal, seasonal, yearly difference in plasmasphere. The magnetic dip also plays an important role in the appearance of the plasmasphere. However, the plasmasphere has its own variation different from the ionosphere. Depending on the solar activity, the variation of EC_{ion} can be several tens of $TECUs$, and the variation of EC_{pl} is at the level of several $TECUs$. Hence, the plasmasphere is relatively more stable than the ionosphere.

Based on the present study, we can find that the $IONf$ is a more stable quantity than EC_{ion} and EC_{pl}, to represent the ionosphere. Since $IONf$ is a ratio, which is constrained within [0, 1], it shows relatively smaller variations, while the EC_{ion} and EC_{pl} can vary in a larger scale. Besides, the

diurnal variation of $ION f$ shows some consistent pattern for the ionosphere in different seasons, magnetic dip ranges and periods of solar cycle. The peak values during the noon in different cases are quite similar. The bottom values occur at pre-sunrise epoch. There is a "ionospheric charging process" during the sunrise-morning period. Hence, $ION f$ is a quantity more suitable for ionosphere modelling. In this study, the Capacitor Model is used to track the ionospheric charging process, with the relative difference between the fitting results and original data less than 0.15.

Chapter 6

Conclusion and Future Work

In this work, the GPS RO technique is applied to study the topside ionosphere. This thesis consists of two related parts. First part focuses on the methodology, the performance of the SM and the impact of the GIMs accuracy on RO retrievals are studied. Second part is the climatological study of the ionosphere and plasmasphere based on RO retrievals using SM.

6.1 Performance of Separability Method (SM) using more accurate GIMs

Classic Abel inversion is a methodology widely used in RO retrievals and the error introduced by the spherical symmetry assumption in classic Abel inversion is also well recognised. SM was introduced to overcome this error. The performance of SM comparing to the classic Abel inversion has been studies in previous studies which have suggested that the improvement of the SM, with regard to the classic approach, is small and/or essentially due to the LoC error. However, in this work, we find that the SM does have significant improvement in RO retrievals excluding the LoC error. The performance of the RO retrievals using SM depends on the accuracy of the GIMs used to aid the inversion, i.e., the more accurate GIMs are used, the better results can be obtained.

In the chapter 3 of this work, two kinds of tests were done to check the performance of SM, and, consequently, to validate the conclusions exposed in that chapter.

- The EC_{100} test, which is not affected by the LoC error. According to the 68% percentile of the error distributions, the results using SM aided by GAGE GIMs can improve by 31% world-wide and 45% over Europe the results obtained using the classic approach. The results also show 10% improvement using GAGE GIMs instead of IGS GIMs

in Europe, the well sounded area with high accuracy of the GAGE GIMs. Moreover, the SM substantially mitigates the artificial plasma caves produced by the large ionospheric gradients in the equatorial region when the classic approach is used.

- Comparison between ionosonde measurements and RO retrievals on $F2$ layer peak density. Similar improvements as those with the EC_{100} test are obtained in this test. Relative errors of RO derived results with respect to ionosonde measurements shown a 32% improvement world-wide and a 39% in Europe for SM aided with GAGE GIMs comparing to the results using the classic technique. With respect to the use of a IGS GIM, the results using SM supported by a GAGE GIM show more than 6% improvement in global comparisons, while it reaches around 11% in Europe.

The error introduced by the mis-modelling of using VTEC instead of EC_{LEO}, the electron content below LEO height, in SM the retrieval of RO profiles using SM, has been checked. Through the comparison between ionosonde measurements and RO retrievals using SM supported with VTEC and EC_{LEO} both derived from GAGE GIMs, one can find that the use of VTEC or EC_{LEO} only has minor impact on the results. This finding shows that the recent methods based on an iterative process, SM aided with $NmF2$ or VTEC maps, are equivalent to the SM using EC_{LEO}.

Finally, a quality criterion based on selecting the ROs yielding a value of β around unity was introduced. After applying this criterion, the results obtained by using SM aided with GAGE GIMs can achieve relative errors, at the 68% percentile, nearly 5% in $foF2$. This level of error is similar to the one obtained when comparing the results from two nearby ionosondes. This implies that using the SM with GAGE GIMs in well sounded areas, one can retrieve the peak electron density from ROs with an accuracy similar to that of ionosonde measurements, with errors smaller than 7% in nearly 80% of the cases in the European region during 2014.

6.2 Two-Components Model for Topside Ionosphere / Bottomside Plasmasphere

The empirical two-components models, STIP model and CPDH model, are introduced to fit the topside ionosphere/bottomside plasmasphere. Different from one-component model, which only considers the ionospheric contribution in topside profiles, the two-components model consists of ionospheric and plasmaspheric portions, i.e., it could separate these two parts from topside profile. In the case of more active ionosphere, i.e., there is

no plasmaspheric contribution in data, the topside ionosphere below LEO height is simplified as one-component model, but with the indication of active ionosphere.

The two-components models are checked and validated in different ways based on some sample data in 2008. First, the goodness of two-components models are checked through relative error dr of fitting results with respect to RO profiles. Among all the results there are around 90% fits with $dr < 0.1$ for STIP model and almost 95% for CPDH model with the same data set for fitting. Besides, the derived hu from two-components models are compared to the direct measurements from CINDI, showing good match between model derived hu and *in situ* measurements for altitudes below the LEO satellite orbits.

The comparison between the STIP model and CPDH model was carried out to check the impact of the assumption of constant plasmaspheric contribution in topside ionosphere used by STIP model. For the individual RO, if the plasmasphere is well developed at the upper limiting altitude of the data set used for fitting, these two models will obtain similar results. However, if the ionosphere is more active, i.e., the plasmasphere is still under developement below the LEO height, CPDH model will get more precise fitting. As a result, we will obtain different scale height hs and transition height hu. Based on the whole sample data set, in November and December, 2008, the histograms of derived hs and hu using these two models are obtained and checked. In solar minimum, there is no evident difference in using STIP model or CPDH model. For quantity $IONf$, there is also no evident difference between these two models. Since the dominant ion below LEO height is O^+, the profile of H^+ has less impact on computing $IONf$. It shows that the assumption of constant plasmaspheric contribution in topside ionosphere used by STIP model is reasonable.

The conditions of applying the STIP model are discussed. The same as all the other empirical models, it shows the picture of topside ionosphere till some limited altitude, which is decided by the LEO height. For derived scale height hs, the parameter reflecting the decaying speed of ionosphere density along the altitude, they are reasonable if there are enough data set for fitting. Considering the height of LEO orbits, around $850km$, it is easy to meet this condition. But for transition height hu, the separation between ionosphere and plasmasphere, the condition is a bit more strict. Since it requires reasonable estimation of both ionospheric and plasmaspheric contributions. Hence, if the derived hu is far above the LEO height, the values are questionable.

6.3 Transition Height and Scale Height in Solar Minimum and Maximum

In the second part of chapter 4, the statistical and climatological study of transition height hu has been carried out based on the RO measurements in 2007 and 2014, solar minimum and maximum respectively, along with other two related parameters: ionospheric scale height, hs, and hu/hs ratio, Rt. The STIP model has been used to fit the topside ionosphere and the model parameters were obtained from the best fitting. The transition height, hu, and scale height, hs, show clear diurnal, seasonal and solar cycle dependences. In general, the hu in summer is higher than the one in winter and it increases along with the solar activity. hu values in solar maximum are larger than the ones in solar minimum. Besides, this parameter also shows significant variations with the dip and longitude. Furthermore, we can observe the link between transition height and equatorial plasma bubbles, i.e., equatorial plasma bubbles cause higher transition height.

On the other hand, we find that hu and hs are highly correlated. The parameter Rt could be used to represent their relationship. Different from hu and hs, Rt is more stable under different situations. Hence, it is a parameter more suitable for modelling.

6.4 $IONf$ concept

Based on the shape function retrieved from the RO measurements using SM aided by the TEC GIMs, the ionospheric fractional contribution to TEC, $IONf$, could be derived. Since the TEC is used in retrievals, the shape functions represents the percentage of the Ne over the TEC at the specific altitude. Once $IONf$ is computed, the ionospheric/plasmaspheric electron contents, EC_{ion} and EC_{pl}, could be separated from the GPS TEC directly.

The features of the ionosphere can be checked through $IONf$, since it is a quantity representing the ionospheric contribution to TEC. Most of the ionosphere anomalies can also be detected using $IONf$, such as winter anomaly, semi-annual anomaly, annual anomaly, SAMA, WSA and mid-latitude trough. The diurnal, seasonal, yearly and latitudinal and longitudinal variations of $IONf$ are studied in chapter 5. Comparing to EC_{ion} and EC_{pl}, $IONf$ is a more stable quantity to represent the ionosphere. Since it is a ratio constrained within [0, 1], while the EC_{ion} and EC_{pl} could vary in a larger range.

Hence, $IONf$ is a quantity more suitable for ionosphere modelling. The diurnal variation of $IONf$ shows a consistent "ionospheric charging process"

during the period from sunrise to midday in all circumstances. In this study, the Capacitor Model is used to track the ionospheric charging process, with the relative difference between the fitting results and original data less than 0.15.

6.5 Some guidelines for Future work

From this work, there are some points that could be studied in future.

- In chapter 4, the CPDH model is introduced and validated with the sample data. This model introduces two extra parameters with respect to STIP model, hp, the scale height with an effective mass of 7 a.m.u, and hz, the height where the controlling factor of H^+ number density is switched from chemical equilibrium to diffusion equilibrium. We can perform a more detailed study of the ionosphere/plasmasphere system using this model and these parameters.

- In solar minimum, the STIP model works well in getting hu. While in solar maximum near magnetic equator, during the noon, there is lack of derived hu due to the active ionosphere. But it is different for scale height hs. In both years, we could get plenty hs, even when the ionosphere is active. Since, to derive reasonable hs, it only requires enough data for fitting. On the other hand, we find the Rt, hu/hs ratio, is a quantity more stable and more suitable for modelling. Hence, we could analyze the derivation of hu in general by modelling Rt.

- The modelling of $IONf$ can be used to derive a global map of ionosphere and plasmasphere. In this study, the "ionospheric charging process" was modelled using the Capacitor Model, showing a great agreement with the data. In future, we could derive a complete model to describe the ionosphere in different situations and then perform an extensive assessment of the model predictions.

Bibliography

[1] Basu S, Buchau J, Rich FJ and Weber EJ (1985) *Ionospheric radio wave propagation.* Handbook of Geophysics and the Space Environment, Fourth edition, Chapter 10, Section 10.1

[2] Benson RF (2010), *Four Decades of Space-Borne Radio Sounding.* Radio Science Bulletin, No 333

[3] Chapman JH and Warren ES (1968) *Topside sounding of the earth's ionosphere.* Space Science Reviews, 846-865.

[4] González-Casado G, Juan JM, Hernández-Pajares M, Sanz J (2013) *Two-component model of topside ionosphere electron density profiles retrieved from Global Navigation Satellite Systems radio occultations.* J Geophys Res Space Phys, 118:7348-7359. doi:10.1002/2013JA019099

[5] Gordon WE (1958) *Incoherent scattering of radio waves by free electrons with applications to space exploration by radar.* Proc. I.R.E., 46, 1824-1829.

[6] Hernández-Pajares M, Juan JM, Sanz J (2000) *Improving the Abel inversion by adding ground GPS data to LEO radio occultations in ionospheric sounding.* Geophys Res Lett 27:2473-2476. doi: 10.1029/2000GL000032

[7] Hernández-Pajares M, Juan JM, Sanz J, Orus R, Garcia-Rigo A, Feltens J, Komjathy A, Schaer SC, Krankowski A (2009) *The IGS VTEC maps: a reliable source of ionospheric information since 1998* J Geod, 83:263-275. doi: 10.1007/s00190-008-0266-1

[8] Hajj GA, Romans LJ (1998) *Ionospheric electron density profiles obtained with the Global Positioning System: Results from the GPS/MET experiment.* Radio Sci 3(1):175-190. doi:10.1029/97RS03183

[9] Lee HB, Jee G, Kim YH, Shim JS (2013) *Characteristics of global plasmaspheric TEC in comparison with the ionosphere simultaneously observed by Jason-1 satellite* Journal of Geophysical Research: Space Physics, Vol.118, 935-946

[10] Prolss, Gerad W (2004) *Physics of the Earth's Space Environment: An introduction.* Springer

[11] Schreiner WS, Sokolovskiy SV, Rocken C, Hunt DC (1999) *Analysis and validation of the GPS/MET radio occultation data in the ionosphere.* Radio Sci 34(4):949-966

[12] Anthes RA, Ector D, Hunt DC, Kuo YH, Rocken C, Schreiner WS, Sokolovskiy SV, Syndergaard S, Wee TK, Zeng Z, Bernhardt PA, Dymond KF, Chen Y, Liu H, Manning K, Randel WJ, Trenberth KE, Cucurull L, Healy SB, Ho SP, McCormick C, Meehan TK, Thompson DC and Yen NY (2008) *The COSMIC/FORMOSAT-3 Mission: Early Results.* Bulletin of the American Meteorological Society, Vol.89, 313-333

[13] Aragon-Angel A, Hernández-Pajares M, Juan JM, Sanz J (2010) *Improving the Abel transform inversion using bending angles.* GPS Solut 14(1):23-33. doi: 10.1007/s10291-009-0147-y

[14] Chou MY, Lin CCH, Tsai HF, Lin CY (2017) *Ionospheric electron density inversion for Global Navigation Satellite Systems radio occultation using aided Abel inversions.* J Geophys Res Space Phys 122:1386. doi:10.1002/2016JA023027

[15] García-Fernández M, Hernández-Pajares M, Juan JM, Sanz J (2003) *Improvement of ionospheric electron density estimation with GPSMET occultations using Abel inversion and VTEC information.* J Geophys Res 108(A9):1338

[16] García-Fernández M, Hernández-Pajares M, Juan JM, Sanz J (2005) *Performance of the improved Abel transform to estimate electron density profiles from GPS occultation data.* GPS Solut 9(2):105-110. doi: 10.1007/s10291-005-0139-5

[17] Hajj GA, Ibanez-Meier R, Kursinski ER, Romans LJ (1994) *Imaging the Ionosphere with the Global Positioning System.* Int J Imaging Technol 5:174-184

[18] Hernández-Pajares M, Juan JM, Sanz J (1998) *Global observation of the ionospheric electronic response to solar events using ground and LEO GPS data.* J. Geophys. Res., 103, 20,789 – 20,796

[19] Fjeldbo G, Kliore AJ and Eshleman VR (1970) *The neutral atmosphere of Venus as studied with the Mariner V Radio Occultation Experiments* The Astronomical Journal, Vol 76.

[20] Newman M, Schubert G, Kliore AJ, Patel IR (1984) *Zonal winds in the middle atmosphere of Venus from pioneer Venus Radio Occultation data* Journal of the atmospheric sciences, Vol.41.

[21] Pedatella NM, Yue X, Schreiner WS (2015) *An improved inversion for FORMOSAT-3/COSMIC ionosphere electron density profiles.* J Geophys Res Space Phys 120:8942–8953. doi:10.1002/2015JA021704

[22] Tulasi Ram S, Su SY, Tsai LC, Liu CH (2016) *A self-contained GIM-aided Abel retrieval method to improve GNSS-Radio occultation retrieved electron density profiles.* GPS Solut 20(4):825-836. doi:10.1007/s10291-015-0491-z

[23] Yue X, Schreiner WS, Kuo YH (2013) *Evaluating the effect of the global ionospheric map on aiding retrieval of the radio occultation electron density profiles.* GPS Solut 17(3):327-335. doi:10.1007/s10291-012-0281-9

[24] Aragon-Angel A, Liou YA, Lee CC, Reinisch BW, Hernández-Pajeres M, Juan JM, Sanz J (2011) *Improvement of retrieved FORMOSAT-3/COSMIC electron densities validated by ionospheric sounder measurements at Jicamarca.* Radio Science 46:RS5001

[25] González-Casado G, Juan JM, Sanz J, Rovira-García A, Aragón-Àngel A (2015) *Ionospheric and Plasmaspheric Electron Contents inferred from Radio Occultations and Global Ionospheric Maps.* J Geophys Res Space Phys, 120(7):5983-5997. doi:10.1002/2014JA020807

[26] Hernández-Pajares M, Juan JM, Sanz J, Colombo O (2002) *Improving the real-time ionospheric determination from GPS sites at Very Long Distances over the Equator.* J Geophys Res Space Phys, 107:1296-1305. doi: 10.1029/2001JA009203

[27] Jakowski N (2005) *Ionospheric GPS Radio Occultation measurements on board CHAMP.* GPS Solut, 9(2):88-95. doi: 10.1007/s10291-005-0137-7

[28] Lee IT, Liu JY, Lin CH, Oyama KI, Chen CY and Chen CH (2012) *Ionospheric plasma caves under the equatorial ionization anomaly* JOURNAL OF GEOPHYSICAL RESEARCH, VOL. 117, A11309, doi:10.1029/2012JA017868

[29] Liu JY, Lin CY, Lin CH, Tsai HF, Solomon SC, Sun YY, Lee IT, Schreiner WS, Kuo YH (2010) *Artificial plasma cave in the low-latitude ionosphere results from the radio occultation inversion of the FORMOSAT-3/COSMIC* Journal of Geophysical research, Vol.115, A07319, doi:10.1029/2009JA015079.

[30] Reinisch BW, Galkin IA (2011) *Global ionospheric radio observatory (GIRO).* Earth, Planets, and Space, 63:377-381. doi:10.5047/eps.2011.03.001

[31] Rovira-García A, Juan JM, Sanz J, González-Casado G (2015) *A World-Wide Ionospheric Model for Fast Precise Point Positioning.* IEEE Trans Geosci Remote Sens 53(8):4596-4604. doi:10.1109/TGRS.2015.2402598

[32] Rovira-García A, Juan JM, Sanz J, González-Casado G, Bertran E (2016) *Fast Precise Point Positioning: A System to Provide Corrections for Single and Multi-Frequency Navigation.* Navigation 63(3):231-247. doi:10.1002/navi.148

[33] Yue X, Schreiner WS, Lei L, Sokolovskiy SV, Rocken C, Hunt DC, Kuo YH *Error analysis of Abel retrieved electron density profiles from radio occultation measurements* Ann. Geophys., 28, 217–222, 2010

[34] Aponte, N., C. G. M. Brum, M. P. Sulzer, and S. A. Gonzalez (2013) *Measurements of the O+ to H+ transition height and ion temperatures in the lower topside ionosphere over Arecibo for equinox conditions during the 2008–2009 extreme solar minimum* JOURNAL OF GEOPHYSICAL RESEARCH: SPACE PHYSICS, VOL. 118, 4465–4470, doi:10.1002/jgra.50416.

[35] Booker HG, Wells HW (1938) *Scattering of radio waves by the F-region of the ionosphere* Terrestrial Magnetism and Atmospheric Electricity banner, 43.

[36] Banks PM, Schunk RW, Raitt WJ (1976) *The Topside Ionosphere: A Region of Dynamic Transition* Annual Review of Earth and Planetary Sciences, Vol. 4: 381-440.

[37] Fejer BG, Scherliess L, Paula ER (1999) *Effects of the vertical plasma drift velocity on the generation and evolution of equatorial spread F* JOURNAL OF GEOPHYSICAL RESEARCH, VOL. 104.

[38] González SA, Feier BG, Heelis RA, Hanson WB (1992). *Ion composition of the topside equatorial ionosphere during solar minimum* Journal of Geophysical Research: Space Physics Vol. 97

[39] Heelis RA, Coley WR, Burrell AG, Hairston MR, Earle GD, Perdue MD, Power RA, Harmon LL, Holt BJ, Lippincott CR (2009). *Behaviour of the O^+/H^+ transition height during the extreme solar minimum of 2008* Geophysical Research Letters, Vol.36.

[40] Hoffman JH (1967) *A mass spectrometric determination of the composition of the nighttime topside ionosphere* Journal of Geophysical Research, Vol. 72, Issue 7.

[41] Hysell DL (2000) *An overview and synthesis of plasma irregularities in equatorial spread F* Journal of Atmospheric and Solar-Terrestrial Physics, Vol. 62.

[42] Thébault E, et al. (2015) *International Geomagnetic Reference Field: the 12th generation.* Thébault et al. Earth, Planets and Space 67:79 DOI: 10.1186/s40623-015-0228-9

[43] Kotov DV, Truhlik V, Richards PG, Stankov S, Bogomaz OV, Chernogor LF, Domnin IF (2015) *Night-time light ion transition height behaviour over the Kharkiv ($50^oN, 36^oE$) IS radar during the equinoxes of 2006-2010* Journal of Atmospheric and Solar-Terrestrial Physics, 132, 2015

[44] kutiev I, Marinov P (2007) *Topside sounder model of scale height and the transition height characteristivs of the ionosphere.* Advances in Space Research 39

[45] MacPherson B, González SA, Bailey GJ, Moffett RJ, Sulzer MP (1998) *The effects of meridional neutral winds on the O^+ - H^+ transition altitude over Arecibo* Journal of Geophysical research, Vol.103, No.A12.

[46] McClure JP, Hanson WB, Hoffman JH (1977) *Plasma bubbles and irregularities in the equatorial ionosphere* Space Physics, Vol 82.

[47] Stankov SM, Jakowski N, Heise S, Muhtarov P, Kutiev I, Warnant R. *A new method for reconstruction of the vertical electron density distribution in the upper ionosphere and plasmasphere* J. Geophys. Res. 108 (A5), 1164, doi:10.1029/2002JA009570, 2003

[48] Torr MR, Torr DG, Richards PG, Yung SP (1990) *Mid- and low-latitude model of thermospheric emissions. I - O(+) (2P) 7320 A and N2 (2P) 3371 A* Journal of Geophysical Research (ISSN 0148-0227), vol. 95.

[49] Tulasi-Ram S, Liu CH, Su SY, Heelis RA (2010) *A comparison of ionospheric O^+/light-ion transition height derived from ion-composition measurements and the topside ion density profile over equatorial latitudes.* Geophysical research letter, Vol. 37.

[50] Webb PA, Essex EA (2001) *A dynamic diffusive equilibrium model of the ion densities along plasmaspheric magnetic flux tubes* Journal of Atmospheric and Solar-Terrestrial Physics 63.

[51] Webb PA, Benson RF, Grebowsky JM (2006) *Technique for determining midlatitude O^+/H^+ transition heights from topside ionosgrams* Radio Science, Vol.41.

[52] Yue X, Schreiner WS, Lei J, Rocken C, Kuo YH, Wan W (2010) *Climatology of ionospheric upper transition height derived from COSMIC satellites during the solar minimum of 2008* Journal of Atmospheric and Solar-Terrestrial Physics 72 1270–1274

[53] Abdu MA, Batista IS, Carrasco AJ, Brum CGM(2005) *South Atlantic magnetic anomaly ionization: A review and a new focus on electrodynamic effects in the equatorial ionosphere* Journal of Atmospheric and Solar-Terrestrial Physics 67, 1643–1657

[54] Belehaki A, Jakowski N and Reinisch BW (2004) *Plasmaspheric electron content derived from GPS TEC and digisonde ionograms.* Adv.Space Res., 33, 833-837

[55] Carpenter DL (1962) *Electron-Density variation in the magnetosphere decuced from Whistler data* Journal of Geophysical Research 67, 9.

[56] Chandra H, Rastogi RG (1970) *Solar cycle and seasonal variation of spread-F near the magnetic equator* Journal of Atmospheric and Terrestrial Physics, Vol. 32, Issue 3.

[57] Chang LC, Liu HX, Miyoshi Y, Chen CH, Chang FY, Lin CH, Liu JY, Sun YY (2015) *Structure and origins of the Weddell Sea Anomaly from tidaland planetary wave signatures in FORMOSAT-3/COSMICobservations and GAIA GCM simulations* J. Geophys.Res. Space Physics, 120, 1325–1340, doi:10.1002/2014JA020752

[58] Evans JV (1969) *Theory and Practice of Ionosphere Study by Thomson Scatter Radar.* Proc. IEEE, 57: 496.

[59] Gowtam VS, Tulasi Ram S (2017) *Ionospheric winter anomaly and annual anomaly observed from Formosat-3/COSMIC Radio Occultation observations during the ascending phase of solar cycle 24* Advances in Space Research 60.

[60] Krankowski A, Zakharenkova I, Krypiak-Gregorczyk A, Shagimuratov II, Wielgosz P (2011) *Ionospheric electron density observed by FORMOSAT-3/COSMIC over the European region and validated by ionosonde data.* Journal of Gnodesy 85(12): 949-964. doi: 10.1007/s00190-011-0481-z

[61] Lunt N, Kersley L, Bishop GJ, Mazzella Jr AJ and Bailey GJ (1999) *The protonospheric contribution to GPS total electron content: Two-station measurements* Radio Science, Vol. 34, No. 5, Pages 1281-1285.

[62] Meza A, Natali MP, Fernández LI (2012) *Analysis of the winter and semiannual ionospheric anomalies in 1999–2009 based on GPS global In-*

ternational GNSS Service maps JOURNAL OF GEOPHYSICAL RESEARCH, VOL. 117, A01319, doi:10.1029/2011JA016882.

[63] Moffett RJ and Quegan S (1983). *The mid-latitude trough in electron concentration of the ionospheric Flayer: a review of observations and modelling.* Journal of Atmospheric and Terrestrial Physics, 45, pp 315-343

[64] Park CG, Carpenter DL, Wiggin DB (1978) *Electron density in the plasmasphere: Whistler data on solar cycle, annual and diurnal variations* Journal of Geophysical Research 83, A7.

[65] Rishbeth H, Jenkins B, Moffett RJ (1995) *The F-layer at sunrise* Annales Geophysicae, Vol. 13, Issue 4.

[66] Sastri JH (1990) *Equatorial anomaly in F-region. A review.* Indian Journal of Radio and Space Physics

[67] Scali JL (1992) *The mid-latitude trough. A review.* Scientific Report No.2

[68] Torr MR, Torr DG (1973) *The seasonal behaviour of the F2-layer of the ionosphere* Journal of Atmospheric and Terrestrial Physics, Vol 34 Issue 12.

[69] Torr MR, Torr DG, Richards PG and Yung SP (1990) *Mid- and low-latitude model of thermospheric emissions 1* $O^+(2P)$ *7320 A and* $N2(2P)$ *3371 A.* Journal of Geophysical Research 95, 21, 147-21, 168

[70] Tsunoda RT (1985) *Control of the seasonal and longitudinal occurrence of equatorial scintillations by the longitudinal gradient in integrated E region Pedersen conductivity* Journal of Geophysical Research: Space Physics. Volume 90, Issue A1

[71] Webb PA, Essex EA (2001) *A dynamic diffusive equilibrium model of the ion densities along plasmaspheric magnetic flux tubes.* Journal of Atmospheric and Solar-Terrestrial Physics 63 1249-1260

[72] Whalen JA (1989) *The daytime F layer trough and its relation to ionospheric-magnetospheric convection* Journal of Geophysical Research 94, A12, 169-184.

[73] Yizengaw E, Wei H, Moldwin MB, Galvan D, Mandrake L, Mannucci A and Pi X (2005) *The correlation between mid-latitude trough and the plasmapause* GEOPHYSICAL RESEARCH LETTERS, VOL. 32, doi:10.1029/2005GL022954

[74] Yizengaw E, Moldwin MB, Galvan D, Iijima BA, Komjathy A, Mannucci AJ (2008). *Global plasmaspheric TEC and its relative contribution to GPS TEC.* Journal of Atmospheric and Solar Terrestrial Physics 70(2008) 1541-1548

[75] Yonezawa T, Arima Y (1959) *On the seasonal and non-seasonal annual variations and the semi-annual variation in the noon and midnight electron densities of the F2 layer in middle latitudes.* J. Radio Res. Labs. 6, 293–309.

[76] Yonezawa T (1971) *The solar-activity and latitudinal characteristics of the seasonal, non-seasonal and semi-annual variations in the peak electron densities of the F2-layer at noon and at midnight in middle and low latitudes* Journal of Atmospheric and Terrestrial Physics, Vol 33. Issue 6.